Computational Analysis of Clinical Brain Sub-cortical Structures

from Ultrahigh-Field MRI

by

Jinyoung Kim

Department of Electrical and Computer Engineering
Duke University

Date:_____

Approved:

_____
Guillermo Sapiro, Supervisor

_____
Allen W. Song

_____
Warren M. Grill

_____
Kristoffer Hauser

_____
Sina Farsiu

Dissertation submitted in partial fulfillment of the requirements for the degree of Doctor of Philosophy in the Department of Electrical and Computer Engineering in the Graduate School of Duke University

2015

ABSTRACT

Computational Analysis of Clinical Brain Sub-cortical Structures

from Ultrahigh-Field MRI

by

Jinyoung Kim

Department of Electrical and Computer Engineering
Duke University

Date:_____

Approved:

_____
Guillermo Sapiro, Supervisor

_____
Allen W. Song

_____
Warren M. Grill

_____
Kristoffer Hauser

_____
Sina Farsiu

An Abstract of a dissertation submitted in partial fulfillment of the requirements for the degree of Doctor of Philosophy in the Department of Electrical and Computer Engineering
in the Graduate School of Duke University

2015

Abstract

Volumetric segmentation of brain sub-cortical structures within the basal ganglia and thalamus from Magnetic Resonance Image (MRI) is necessary for non-invasive diagnosis and neurosurgery planning. This is a challenging problem due in part to limited boundary information between structures, similar intensity profiles across the different structures, and low contrast data. With recent advances in ultrahigh-field MR technology, direct identification and clear visualization of such brain sub-cortical structures are facilitated. This dissertation first presents a semi-automatic segmentation system exploiting the visual benefits of ultrahigh-field MRI. The proposed approach utilizes the complementary edge information in the multiple structural MRI modalities. It combines optimally selected two modalities from susceptibility-weighted, T_2-weighted, and diffusion MRI, and introduces a tailored new edge indicator function. In addition to this, prior shape and configuration knowledge of the sub-cortical structures are employed in order to guide the evolution of geometric active surfaces. Neighboring structures are segmented iteratively, constraining over-segmentation at their borders with a non-overlapping penalty. Experiments with data acquired on a 7 Tesla (T) MRI scanner demonstrate the feasibility and power of the approach for the segmentation of basal

ganglia components critical for neurosurgery applications such as Deep Brain Stimulation (DBS) surgery.

DBS surgery on brain sub-cortical regions within the Basal ganglia and thalamus is an effective treatment to alleviate symptoms of neuro-degenerative diseases. Particularly, the DBS of subthalamic nucleus (STN) has shown important clinical efficacy for Parkinson's disease (PD). While accurate localization of the STN and its substructures is critical for precise DBS electrode placement, direct visualization of the STN in current standard clinical MR imaging (e.g., 1.5-3T) is still elusive. Therefore, to locate the target, DBS surgeons today often rely on consensus coordinates, lengthy and risky micro-electrode recording (MER), and patient's behavioral feedback. Recently, ultrahigh-field MR imaging allows direct visualization of brain sub-cortical structures. However, such high fields are not clinically available in practice. This dissertation also introduces a non-invasive automatic localization method of the STN which is one of the critical targets for DBS surgery in a standard clinical scenario (1.5T MRI). The spatial dependency between the STN and potential predictor structures from 7T MR training data is first learned using the regression models in a bagging way. Then, given automatically detected such predictors on the clinical patient data, the complete region of the STN is predicted as a probability map using learned high quality information from 7T. Furthermore, a robust framework is proposed to properly weight different training subsets, estimating their influence in the prediction accuracy. The STN prediction on the clinical 1.5T MR datasets

from 15 PD patients is performed within the proposed approach. Experimental results demonstrate that the developed framework enables accurate prediction of the STN, closely matching the 7T ground truth.

To Heeju, Minjun, and all my family…

Contents

List of Tables

List of Figures

Acknowledgements

First, I would like to thank my Master's and Ph.D. advisor, Prof. Guillermo Sapiro. He has been always patient with me, while giving me the freedom to pursue my academic goals and invaluable advice to keep me on the right track. He is not simply a supervisor, but a truly great teacher and leader. He always treats students as whole individuals and guides in a way that prioritizes their development and overall well-being. It is my privilege to have him as a mentor in my academic and personal life.

I am deeply grateful to all members of my Ph.D. Committee - professors Allen Song, Warren Grill, Kris Hauser, and Sina Farsiu - who took patience to read my thesis and provided me with their constructive feedback.

I would also like to thank Prof. Noam Harel, a co-advisor from the Center for Magnetic Resonance Research (CMRR), University of Minnesota. He greatly advised me to maintain a balance between scientific and clinical perspectives, and provided large scale clinical datasets for this thesis. I am also thankful to Prof. Christophe Lenglet at the CMRR who provided me with very helpful guidance for the first part of my thesis.

As well, I thank my collaborators - Yuval Duchin, Ruby Shamir (Surgical Information Sciences, Inc), and Hyunsoo Kim (A Ph.D. student from Computer Science at Duke University) with whom I had great discussions during my thesis. Yuval pre-processed a large amount of datasets used in the second part of my thesis, and Ruby is making it possible to transfer our techniques in my thesis to clinical applications in

practice, with their extensive anatomical knowledge. Hyunsoo gave me a great help to implement and test various learning methods during his summer internship in our lab.

Furthermore, I would like to thank all my labmates - Mariano Tepper, Qiang Qiu, Mauricio Delbracio, Cecilia Aguerrebere, Jose Lezama, Jordan Hashemi, Chris Tralie, Anish Simhal, and Zhuoqing Chang. I am very proud that I am a member of this great and talented team. I hope that they achieve academic successes in their future.

Finally, on my personal note, I must thank my wife, Heeju and my son, Minjun for their patience and love. They always motivated me to pursue this long journey. I am also grateful to all my family members, especially my parents, brother, Jungwook, my wife's parents, and siblings for their endless supports and encouragement during my Ph.D. Without all their incredible helps, I would not have been able to complete my Ph.D.

The research projects during this thesis were partially supported by NIH, the Human Connectome Project, the W. M. Keck Foundation, ONR, NGA, ARO, NSF, and DoD.

1. Introduction

1.1 Problem statements

The differentiation and localization of brain structures is a crucial component for any neuroscience research or clinical applications. Volumetric segmentation is a pre-requisite for many neuroimaging studies such as voxel-based morphometry (VBM), statistical shape analysis, white matter fiber tractography from diffusion-weighted Magnetic Resonance Imaging (MRI), or seed-based analysis of resting-state functional MRI (fMRI). It is also critical for surgical interventions such as Deep Brain Stimulation (DBS) surgery or tumor resection. However, manual segmentation is prone to inherent confounds such as operator subjectivity and inter- or intra-observer variability of border definitions, which are all driven by the quality and richness of the input data. Most importantly, manual segmentation of fine brain structures is a tedious, time consuming and significantly limiting factor for any clinical or translational workflow that requires anatomical definition. The problem is further aggravated when multiple modalities are available, each modality providing enhanced information for the segmentation of specific structures, forcing the user to discover that and to constantly switch between them. These challenges will become more and more relevant with the proliferation and advances of high-field MR machines that provide higher-resolutions images with superior contrast that allows the delineations of smaller structures with greater shape complexity. This dissertation first addresses the research question: **How to utilize the visual benefits of**

ultrahigh-field multi-modal (contrasts) MRI to accurately and automatically segment adjacent brain sub-cortical structures?

DBS surgery is a popular surgical intervention for symptom's alleviation of patients with neurological disorders. Recently, DBS procedures for essential tremor, Parkinson's disease (PD), and dystonia were approved by Food and Drug Administration (FDA), and the demands are expected to further increase. Accurate placement of the electrodes into target structures is a crucial procedure for successful DBS, since slight misplacement onto adjacent structures or even within target region may result in severe side effects. To verify the location of the electrodes, current practices utilize intra-operative electro-physiological methods that include lengthy burdensome steps and might be associated with procedural hemorrhage. Direct visualization and localization of target structures on the individual patient's MRI is required for safe and efficient DBS targeting, reducing the need of the electrophysiological procedures (Dormont et al., 2010; Xiao et al., 2014b). While recent ultrahigh-field MR imaging techniques directly visualize targeting structures with the superior contrast and high resolution (Abosch et al., 2010; Cho et al., 2010; Kerl et al., 2012), and most recent studies have proven their clinical feasibility, addressing a wide range of artifacts (Duchin et al., 2012; Zitella et al., 2015), such high-field MR machines are limited for clinical availability due to significantly increased costs. Therefore, MRI-guided DBS planning still needs to be performed in a standard clinical scenario (e.g., 1.5 or 3T), where high quality information is not available.

With these practical challenges, this dissertation also addresses the research question: **How to learn high quality information from ultrahigh-field MRI and utilize it for guidance of DBS targeting on standard clinical data?**

The preceding questions motivate the research objective of this dissertation: ***To provide automatic tools for segmentation from ultrahigh-field MRI and its application to DBS targeting in standard clinical scenarios.*** The main contributions for the objective are provided in each chapter of this dissertation.

1.2 Thesis outline

Chapter 2 presents the article "Semi-automatic segmentation of brain sub-cortical structures from high-field MRI" (Kim et al., 2014) published in IEEE Journal of Biomedical and Health Informatics, addressing the first research question. The goal of this work is to provide an automatic framework for delineation of adjacent brain sub-cortical structures with global shape constraints, optimally combining visual properties from two single modality 7T MRIs.

Chapter 3 introduces an ultrahigh-field MR atlases based automatic localization method of DBS targeting structures in a standard clinical scenario, addressing the second research question. A part of the chapter, titled "Direct patient-specific deep brain stimulation is here: Automatic localization of surgical target structures via robust shape relationship learning from ultrahigh-field MRI" will be submitted to NeuroImage for publication (Kim et al., 2015d). The key contribution of this work is to transfer learned

high quality shape information from 7T onto a patient-specific 1.5T MRI for automatic localization of DBS targeting structures. The initial articles also have been published in the conferences ISBI (International Symposium on Biomedical Imaging) held in New York, NY in April 2015, ICIP (International Conference on Image Processing) held in Quebec city, Canada in September 2015, and MICCAI (Medical Image Computing and Computer Assisted Interventions) held in Munich, Germany in October 2015 (Kim et al., 2015a, 2015b, and 2015c).

Finally, Chapter 4 provides concluding remarks.

2. Semi-automatic segmentation of brain sub-cortical structures from multi-contrast ultrahigh-field MRI

2.1 Introduction

Various segmentation frameworks have been reported to automate the manual segmentation during the last two decades. However, most segmentation methods still require user intervention, and some artifacts such as over-segmentation around boundaries of neighboring objects are unavoidable. In particular, when an image has low-contrast or objects to be segmented are occluded, segmentation techniques have shown limited performance (Fang and Chan, 2007; Madden, 2007). Therefore, segmentation of complex and adjacent objects such as sub-cortical structures in brain MR images still remains a challenging task. In general, segmentation approaches are based on local edge information (edge based) or the intensity of a given image (region based). Accuracy of edge detection and the image quality such as its Contrast-to-Noise Ratio (CNR) and Signal-to-Noise Ratio (SNR) are critical factors in the segmentation performance. On the other hand, region based approaches utilize the distribution of intensities over the entire region of interest, and they are more robust to noise or missing information than edge based approaches (Chan and Vese, 2001). However, neighboring regions can have similar intensity distributions that often overlap.

Recently, it has been reported that Susceptibility Weighted Image (SWI) at higher magnetic fields provides superior image contrast, thereby allowing improved delineation of sub-cortical structures (Abosch et al., 2010). Moreover, detailed anatomical information

obtained by combining SWI with T_2-weighted (T_2W) or Fractional Anisotropy (FA) images enables localization and visualization of sub-cortical structures (Lenglet et al., 2012).

In this work, we focus on the segmentation of sub-cortical structures such as the basal ganglia and thalamus from MRI data obtained at high magnetic field (7T), critical for any neurosurgery planning and particularly for DBS procedures (Dormont et al., 2010). We start with an edge based segmentation approach to exploit sufficient edge information on the MRI (with high CNR and SNR), embedded in an active contour/surface model (Terzopoulos et al., 1988). The geodesic active contour/surface (GAC/GAS) model (Caselles et al., 1997) originally translated the energy based active contours' minimization problem into a geometric curve evolution approach computing a geodesic curve in a Riemannian space via the level-sets method (Osher and Sethian, 1988), thereby handling topological changes of evolving curves as well as increasing attraction of the active contour toward the boundary, even with high variation of gradient values. Its 3D extension led to the geodesic active surface (GAS) model (Caselles et al., 1997), which is the basis of our proposed framework. However, this approach fails to achieve accurate segmentation results for occluded objects or regions with weak or missing boundaries that commonly exist in MRI data.

Several approaches have been proposed in order to address this problem by incorporating shape prior information (Fang and Chan, 2007; Leventon et al., 2000; Madden, 2007; Uzunbas et al., 2000). In Leventon et al. (2000), in particular, training

shapes are represented by the level-set method as a Gaussian distribution in the subspace obtained by Principle Component Analysis (PCA), and level-set curves evolve toward a best-fit shape estimated using maximum a posteriori (MAP) within the GAC framework. More recently, Uzunbas et al. (2010) jointly incorporates shapes of multi-objects and their relative pose relationships into a region based approach for the segmentation of multiple structures. Our proposed method considers the volumetric shape model incorporated into the GAS framework (Leventon et al., 2000).

Additionally, we extract the edge information integrating edge maps generated from multi-modal MR images (referring to different image contrasts in this context) such as SWI, T_2W image, and FA image, using a new edge indicator function. Boundary information from the shape prior, initially located on a region overlapping with an object after registration onto the data to be segmented, is applied as a weighting factor for the edge maps of the multi-modal images. Several segmentation approaches using multi-modal MR data have been introduced and applied for localization of deep brain structures or prostate cancer (Kacem et al., 2010; Artan et al., 2010). These works present segmentations improved by combining additional information from the diffusion data (e.g., FA or Apparent Diffusion Coefficient (ADC) image). However, we fully exploit superior contrast and SNR properties of SWI, T_2W image and FA image at the high-field, providing a new edgemap. Moreover, we exploit the optimal combination of multi-modal data, where each brain sub-cortical region is fairly visible.

Over-segmentation around boundaries between neighboring structures is inevitable during the semi-automatic segmentation process. Overlapping regions are often found also on manual segmentations because of inaccurate definition of the boundary information. However, accurate delineation of adjacent structures, such as the basal ganglia and thalamic structures in the brain, provides crucial information in neuro-surgical procedures such as DBS surgery (Abosch et al., 2010). Some approaches have been proposed in the literature in order to overcome such overlapping problem (Lucas et al., 2012; Paragios and Deriche, 2000a; Zimmer and Olivo-Marin, 2005). A multi-stage level set segmentation within the geodesic active region framework (Paragios and Deriche, 2000a), and coupled parametric active contours (Zimmer and Olivo-Marin, 2005), respectively, employing an additional force to constrain the overlapping during the propagation of multiple regions are introduced. More recently, an efficient multi-object level set method using the projection method within the GAC framework was proposed in (Lucas et al., 2012).

However, simultaneous segmentation of adjacent structures might lead to inaccurate delineation (i.e., dividing line) even though it disjoints those structures in an efficient way, in practical cases (e.g., SN and STN) where there exist unclear boundaries (i.e., similar intensity profiles within adjacent structures) between those regions or the initialization is not favorable, especially, in Zimmer and Olivo-Marin (2005).

In this work, we have added a penalty term into our framework, considering adjacency between basal ganglia and thalamic structures, thereby incorporating another layer of prior structural information. The segmentation process for each structure follows the subject-specific manual analysis pipeline presented in Lenglet et al. (2012). Structures are initially segmented with two different contrast MR images (simultaneous combination of additional contrasts doesn't necessarily improves the results since the regions are not all visible in all contrasts), as well as prior knowledge about those regions and represented by the level-set method. Then, each pre-defined level-set surface is utilized as a non-overlapping constraint, limiting the possible deformation of the other evolving surface toward its adjacent structures within our framework. Moreover, a set of segmented adjacent structures can be further refined in order to produce more accurate delineation during the iterative process.

Section 2.2 describes each extension within the GAS framework in detail. The schematic overview for the segmentation of basal ganglia and thalamic structures is presented in Section 2.3. We then provide experimental results on real 3D 7T MRI in Section 2.4. Finally, we discuss potential research directions in Section 2.5 and conclude the work in Chapter 4. This work was published in Kim et al. (2014).

2.2 Methods

We extend the geodesic/geometric active surface (GAS) model (or minimal surfaces) by incorporating additional global information, including shape priors and non-

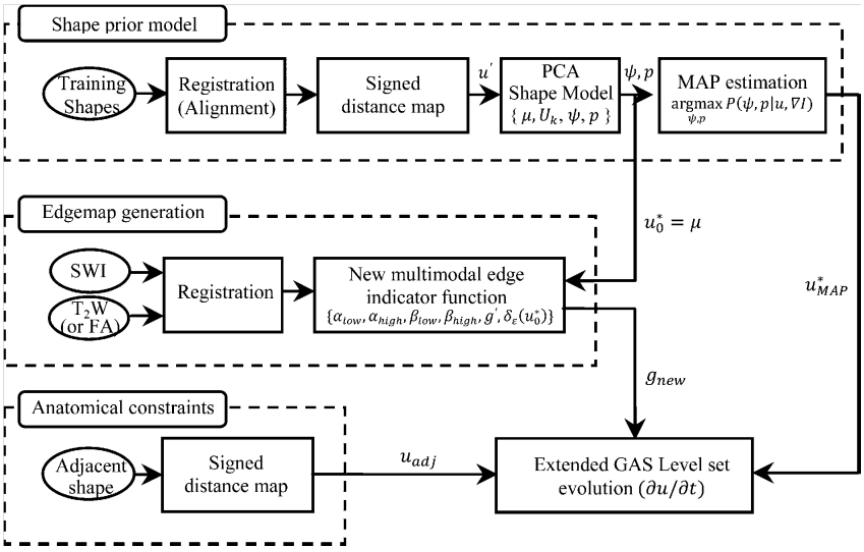

Figure 1: Schematic overview of the proposed segmentation.

overlapping constraints. The target application in this work is the segmentation of sub-cortical structures, as a key ingredient in DBS protocols, and additional known non-overlapping constraints are exploited, in the form of negative distance forces between the corresponding evolving surfaces. This encodes the basic anatomical relationships between the different components in these regions. The per-structure shape prior model is built via a probabilistic approach and incorporated into the GAS model by estimating its best-fit shape and pose while guiding the evolving surfaces toward it. A newly introduced edge indicator function is obtained by integrating edge maps generated from the Laplacian of the smoothed multi-modal datasets (SWI, T_2W, and FA image from DWI), together with boundary information about the given shape prior (initially, it is registered onto the region maximally matching with the structure to be segmented). Overview of the proposed

segmentation framework is presented in Figure 1. The next sections describe these contributions in detail.

2.2.1 Geodesic active surface model

Given a 3D image $I: \mathbb{R}^3 \to \mathbb{R}^+$ (this will later be extended to multi-modal data, meaning vectorial 4D images) and an evolving 2D surface $S: \mathbb{R}^+ \times [0,1]^2 \to \mathbb{R}^3$ in parametric form, $S(t,r,v) = \{x(t,r,v), y(t,r,v), z(t,r,v)\}$, $(t,r,v) \in \mathbb{R}^+ \times [0,1]^2$, the goal of active surfaces is to propagate this 2D surface in the 3D image space such that it evolves toward the region of interest and stops at its boundary. For this purpose, a deformable surface model was proposed by Terzopoulos et al. (1988). The GAS model was developed to extend this classical model (Caselles et al., 1997), and is based on solving the functional

$$E_{GAS}(S) = \iint_{A(S)} g(I(S))da, \tag{2.1}$$

where da is the Euclidean element of area, and the Euclidean area of the surface S is given by $A(S) \coloneqq \iint da$. Also, g is a decreasing function such that $g(\chi) \to 0$ as $\chi \to \infty$ (to be more precise, as the gradient magnitude of the variable goes to zero). This edge indicator function should attract the surface towards the objects of interest, and in Caselles et al. (1997a, 1997b) it was selected as (considering it is now defined in the whole image space and not just on the evolving surface)

$$g(I) = 1/(1 + |\nabla \hat{I}|^{\gamma}), \tag{2.2}$$

where $\hat{I}$ is a smoothed version obtained by regularizing I using anisotropic diffusion, and γ is 1 or 2. For the simplification, we write g(I) instead of g(I(S)).

The following surface evolution (Euler-Lagrange) equation, minimizing E_{GAS}, is obtained by calculus of variations:

$$\frac{\partial S}{\partial t} = \left(g(I)H - \nabla g(I)\cdot\vec{\mathcal{N}}\right)\vec{\mathcal{N}}, \tag{2.3}$$

where H is the mean curvature and $\vec{\mathcal{N}}$ is the inner unit normal to the evolving surface S. The steepest descent flow described above is implemented using the level-sets method (Osher and Sethian, 1998) via an embedding function given by the signed distance map, $u: \mathbb{R}^+ \times \mathbb{R}^3 \to \mathbb{R}$, whose zero level-set function is the surface S (i.e., u(t, S) = 0):

$$\frac{\partial u}{\partial t} = |\nabla u|\operatorname{div}\left(g(I)\frac{\nabla u}{|\nabla u|}\right) = g(I)|\nabla u|\operatorname{div}\left(\frac{\nabla u}{|\nabla u|}\right) + \nabla g(I)\cdot\nabla u. \tag{2.4}$$

As it is standard practice, the following minimal surfaces model is obtained by adding a constant motion force c, weighted by g(I), in order to increase the speed of convergence (Caselles et al., 1997b),

$$\frac{\partial u}{\partial t} = \left(\operatorname{div}\left(g(I)\frac{\nabla u}{|\nabla u|}\right) + cg(I)\right)|\nabla u| = g(I)(c + H)|\nabla u| + \nabla g(I)\cdot\nabla u. \tag{2.5}$$

In this level-set representation, the surface u evolves at all points normal to the level-set as a function of the image gradient and the surface curvature at that point. The term $\nabla g(I) \cdot \nabla u$ provides stable detection of boundaries even if variations in their gradient are large, and makes the model more robust to parameters choice (Caselles et al., 1997b).

In this work, the segmentation of sub-cortical structures from MRI data is performed within this GAS framework, with extension to be presented in the next three sections.

2.2.2 Guidance from statistical shape models

The GAS model utilizes edge information to detect objects as discussed in the previous section. This approach has shown reliable and fast in many applications (Fang and Chan, 2007; Leventon et al., 2000; Lorigo et al., 2000; Paragios and Deriche, 2000b). However, low contrast or occlusion around objects' boundaries might lead to inaccurate segmentations. In this case, guiding the surface evolution via shape (and pose) prior information can considerably improve the quality of the segmentation. In Leventon et al. (2000), the shape model is built based on a probabilistic approach and is then incorporated into the GAS framework. The modeling of the shape prior and the estimation of the shape and pose parameters is briefly summarized below.

2.2.2.1 Shape representation

Each surface in the provided training dataset $\mathcal{T} = \{S_1, \dots, S_l \dots, S_n\}$, represented as a binary segmentation, is embedded as the zero level-set of a higher dimensional surface

$S_l \in \mathbb{R}^3 \rightarrow \mathbb{R}$, using the signed distance map, where each point (N^3 points if it is assumed that a 3D shape template is cropped into a size N in each dimension) encodes the distance to the nearest points on the surface. A mean surface (shape) μ is obtained as the arithmetic mean of the training shape $\mathcal{T}$. The variance of the shape is computed using Principal Component Analysis (PCA). A matrix $M \in \mathbb{R}^{N^3 \times n}$ is constructed consisting of column vectors $\hat{S}_l$, obtained from subtracting the mean μ from S_l. Then the covariance matrix $\frac{1}{n-1}MM^\intercal$ is decomposed using Singular Value Decomposition (SVD),

$$U\Sigma U^\intercal = \frac{1}{n-1}MM^\intercal. \tag{2.6}$$

Here, $U \in \mathbb{R}^{N^3 \times n}$ is a unitary matrix whose columns represent n orthogonal modes of shape variation, and $\Sigma \in \mathbb{R}^{n \times n}$ is a diagonal matrix of the corresponding eigenvalues as scaling factors along these variations. An estimate of a new shape u′ is represented by combining the first k principle components, and is given by the coefficients $\psi \in \mathbb{R}^k$. The dimension of the training set is therefore reduced to k by projecting $u' - \mu$ onto the k principle components,

$$\psi = U_k^\intercal(u' - \mu), \tag{2.7}$$

where U_k is a matrix with the first (largest corresponding eigenvalues) k columns of U.

Given ψ, the estimate $\tilde{u}$ of u' is reconstructed as

$$\tilde{u} = U_k \psi + \mu. \tag{2.8}$$

2.2.2.2 Prior shape and pose estimation

The probability of a particular surface is computed by assuming, following the PCA model, a Gaussian distribution in the reduced shape subspace,

$$P(\psi) = \frac{1}{\sqrt{(2\pi^k |\Sigma_k|)}} \exp\left(-\frac{1}{2}\psi^T \Sigma_k^{-1} \psi\right), \tag{2.9}$$

where Σ_k is a matrix with the first (largest eigenvalues) k rows and columns of Σ.

Note that the shape model cannot guide the surface evolution without its global pose information, as the structures must be registered for the shape information to be relevant. Let the shape surface, u^*, be determined from the shape parameter ψ and the pose p. The surface u evolves toward the target shape by estimating u^* using the maximum a posteriori (MAP) at a given discrete time t following

$$u(t+1) = u(t) + \lambda_1\left(u^*_{MAP}(t) - u(t)\right), \tag{2.10}$$

where $\lambda_1 \in [0,1]$ is a coefficient that controls the effect of the estimated surface model.

More specifically, u^* is estimated using MAP at each update of the surface evolution,

$$u^*_{MAP} = \underset{u^*}{\operatorname{argmax}}\ P(u^* \mid u, \nabla I). \tag{2.11}$$

Accordingly, parameters ψ and p are also estimated (2.12), and u^*_{MAP} is then computed using Bayes Theorem (Leventon et al., 2000).

$$< \psi_{MAP}, p_{MAP} >= \underset{\psi,p}{\operatorname{argmax}}\ P(\psi, p \mid u, \nabla I) \tag{2.12}$$

2.2.2.3 Level set evolution with shape information

The evolution equation of the surface in (2.10) is incorporated into the (discrete time) level-set equation (2.5):

$$u(t+1) = u(t) + \lambda_1\left(u^*_{MAP}(t) - u(t)\right) + \lambda_2\left(g(I)(c+H)|\nabla u(t)| + \nabla g(I)\cdot\nabla u(t)\right), \tag{2.13}$$

where λ_2 controls the tradeoff between the shape prior and the image forces. In this framework, the surface evolves globally, towards the MAP estimate of a given shape model (prior), and locally based on image gradient and surface curvature.

2.2.3 A new multi-modal edge indicator function

The inverse function g(I) of image gradient in (2.2), commonly selected as an edge indicator in active surface models, often fails to generate clear edge information when the objects to be segmented have low contrast boundaries. In this section, a new edge indicator function is introduced by combining edge maps generated from the Laplacian of multi-modal images (i.e., multiple modalities all derived from MRI), together with boundary information from the shape prior presented in the previous section.

Recently, it has been shown that SWI at higher magnetic fields shows superior contrast, especially within the basal ganglia and thalamus structures, by comparison with T_1W and T_2W images (Abosch et al., 2010; Cho et al., 2010). To take advantage of this, the edge information of the SWI is integrated with that of T_2W images, and with FA images obtained from diffusion MRI, defining a new edge indicator function. This automates the procedure typically followed by experts performing the manual segmentation and switching between various modalities to exploit information from multiple contrasts (Lenglet et al., 2012). The main steps to compute this new edge indicator function with fusion of multi-modal images are described next.

2.2.3.1 Edge maps from two modality MR images

The stopping function g in (2.2) is substituted by g′ using a sigmoid function, whose center and width are controlled by the user (Madden, 2007). Additionally, the zero-crossing of the Laplacian image, instead of the image gradient, is applied in order to detect

more detailed boundaries,

$$g'(I) = 1/(1 + e^{-\left(\frac{\Delta\hat{I}-\beta}{\alpha}\right)}), \tag{2.14}$$

where β is the center of the intensity range, and α is in inverse proportion to the slope of the function at β (i.e., the slope is $1/4\alpha$). Also, $\Delta\hat{I}$ is the Laplacian of a regularized image. Note that regularization such as anisotropic diffusion before the Laplacian operation is important for the noisy SWI.

Two edge map terms, g'_{High} and g'_{Low}, are computed with β_{High} and β_{Low}, and a fixed value of α, tuned by the user with respect to each modality image, such as the T_2W (or FA) and SWI images, using (2.14). These edge map terms have comparable values (0 or 1) within regions with strong boundaries or homogeneous intensities, but have different values in intermediate regions (see Figure 2). More specifically, a positive (or negative) α is selected to transform higher intensity values of the Laplacian magnitude into homogeneous regions (or boundaries) by the sigmoid function. As in Figure 2(a), if $\alpha > 0$, β_{High} is manually chosen to be the value of the Laplacian magnitude of the smoothed SWI to produce g'_{High}, where regions with intensity values over β_{High} are considered as strongly homogeneous, thereby capturing more edge information on the SWI.

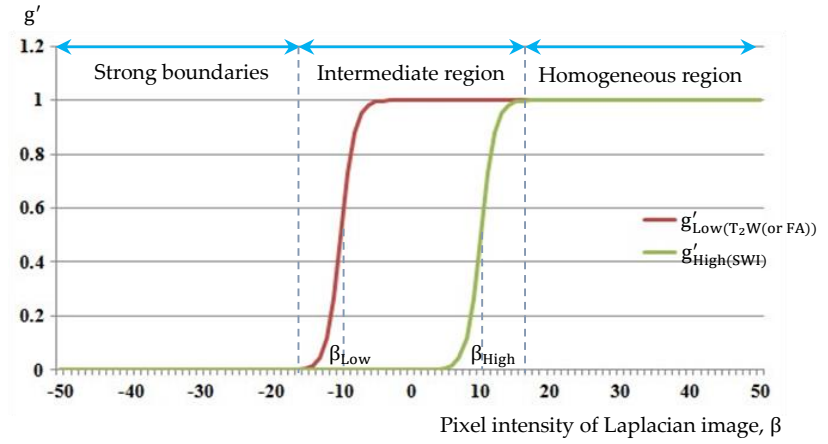

(a)

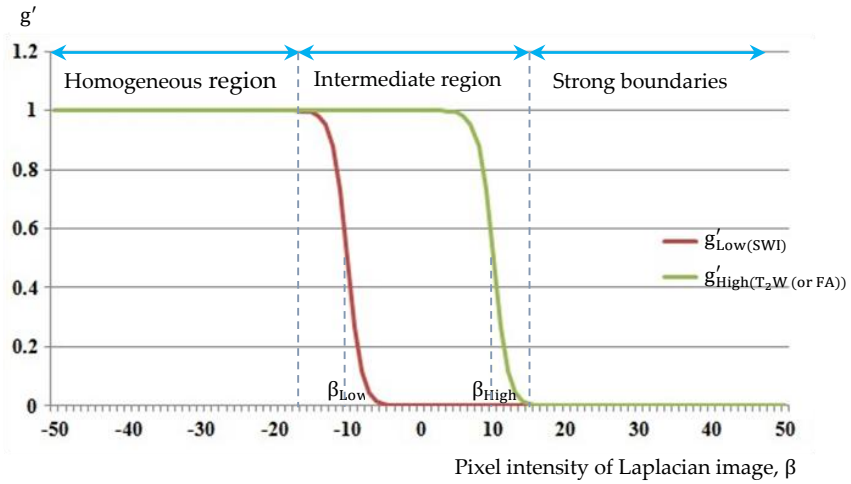

(b)

Figure 2: Sigmoid function with β_{Low}=-10, β_{High}=10, and (a) α=1, (b) α=-1

Also, β_{Low} is manually chosen to be the value of the Laplacian magnitude of the smoothed T_2W (or FA) image to produce g'_{Low}, where regions with intensity values under β_{Low} are considered as strong boundaries, thereby capturing wider homogeneous regions on the T_2W (or FA) image. On the other hand, as in Figure 2(b), if $\alpha < 0$, β_{High} is manually chosen

to be the value of the Laplacian magnitude of the smoothed T_2W (or FA) image to produce g'_{High}, where regions with intensities over β_{High} are considered as strong boundaries, thereby capturing wider homogeneous region on the T_2W (or FA) image. Additionally, β_{Low} is manually chosen to be the value of the Laplacian magnitude of the SWI to produce g'_{Low}, where regions with intensities under β_{Low} are considered as homogeneous regions, thereby capturing more edge information on the SWI.

2.2.3.2 Generation of a new edge map g_{new}

A new edge map g_{new}, is obtained from g'_{Low} and g'_{High}. Let $g'_{Low\ (T_2W\ (or\ FA))}$ or $g'_{High\ (T_2W\ (or\ FA))}$ be the edge map terms computed using (2.14) with β_{Low} and a fixed positive α, or β_{High} and a fixed negative α, on the T_2W (or FA) image; and let $g'_{Low\ (SWI)}$ or $g'_{high\ (SWI)}$ be the edge map terms computed with β_{Low} and a fixed negative α, or β_{High} and a fixed positive α, on the SWI. An edge map g_{new} is computed by weighted averaging of g'_{High} and g'_{Low} with the (smoothed) Dirac measure δ_ε of u_0^*, the level-set of a given shape prior on the initial position (registered onto the test data), to weight the values of $g'_{low\ (T_2W\ (or\ FA))}$ on the homogeneous region and $g'_{High\ (SWI)}$ on the boundary surface (zero level-set) within the shape prior if $\alpha > 0$, or values of $g'_{High\ (T_2W\ (or\ FA))}$ on the homogeneous region and $g'_{Low\ (SWI)}$ on the boundary surface within the shape prior if $\alpha < 0$:

$$g_{new} = \begin{cases} (1 - \delta_\varepsilon(u_0^*))g'_{\text{Low } (T_2W \text{ (or FA)})} + \delta_\varepsilon(u_0^*)g'_{\text{High (SWI)}} & ; \alpha > 0 \\ (1 - \delta_\varepsilon(u_0^*))g'_{\text{High } (T_2W \text{ (or FA)})} + \delta_\varepsilon(u_0^*)g'_{\text{Low (SWI)}} & ; \alpha < 0 \end{cases} \quad (2.15)$$

where the Dirac measure δ_ε is defined as the regularized version of the derivative $\delta_0(z)$ of the Heaviside function H(z) (Madden, 2007; Chan and Vese, 2001):

$$\delta_\varepsilon(z) = \frac{\varepsilon}{\varepsilon^2 + z^2}, \quad \delta_0(z) = \frac{d}{dz}H(z), \text{ where } H(z) = \begin{cases} 1 & ; z \geq 0 \\ 0 & ; z < 0 \end{cases} \quad (2.16)$$

Here ε is the width of the function. Specifically, $\delta_\varepsilon(u_0^*)$ with ε =1 is 1 on the boundary of a given shape prior on the initial position. In this case, g_{new} captures sufficient boundary information on the SWI if it is assumed that the shape prior on the initial position optimally matches the object to be segmented (g_{new} is fixed during the shape/surface evolution for stability). In particular, the initial shape surface u_0^* is obtained by averaging shape priors registered onto the object to be segmented (or the boundaries of the regions on the edge map ($g'_{\text{High (SWI)}}$ if $\alpha > 0, g'_{\text{Low (SWI)}}$ if $\alpha < 0$) generated from the SWI), using FSL FLIRT (FMRIB's Linear Image Registration Tool) (Jekinson et al., 2002) or the Euler transformation in 3D provided by the user (i.e., $u_0^* = \mu$). Proper initial placement of a given shape model contributes not only to accurately integrate boundary information of the initial shape surface into the new edge map, but also reduces the MAP

estimation time of the shape prior step. Note that corresponding training shapes registered initially onto the test data are overlapped with structures to be segmented since training shapes are manually segmented versions from other datasets on the same ROI as the test dataset.

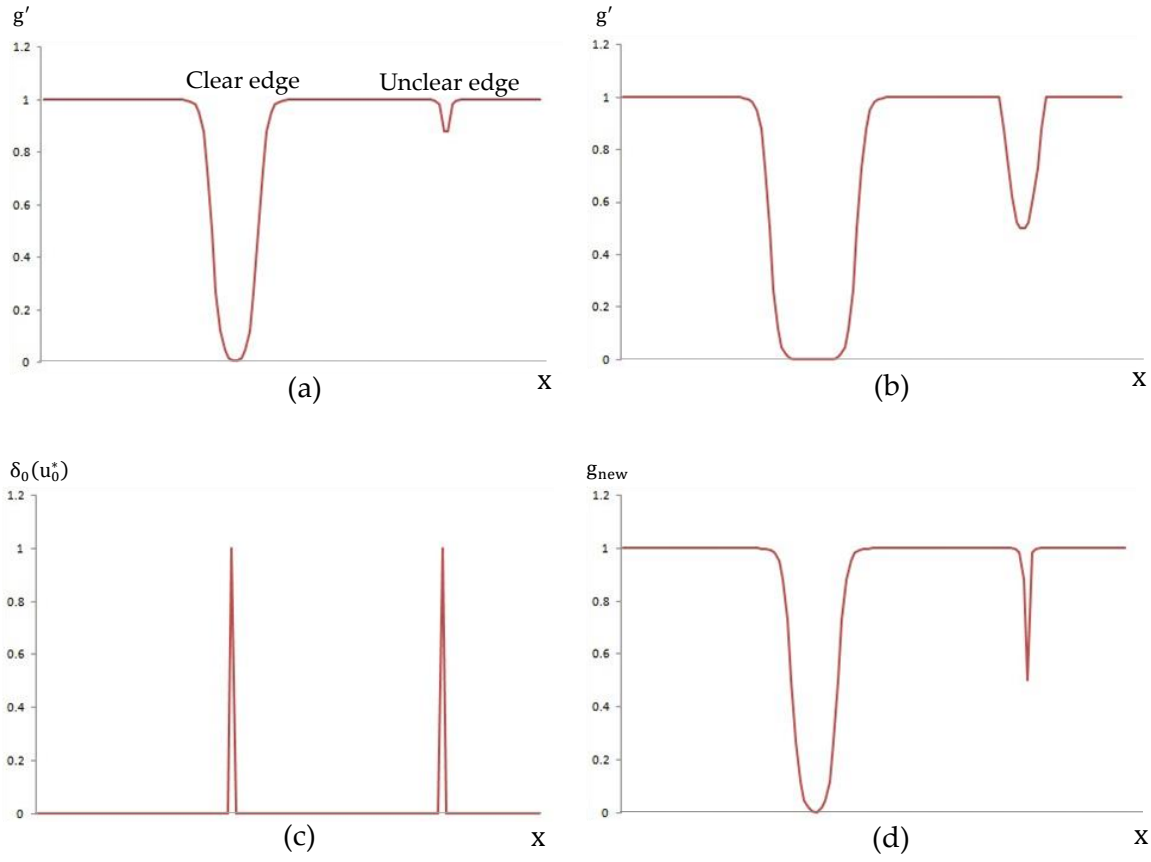

Figure 3: Interpretation of g_{new} on the clear edge and unclear edge in a 1D (in case of α<0). (a) g' with β_{High} on T_2W in (2.14), $g'_{High\ (T_2W)}$. (b) g' with β_{Low} on SWI in (2.14), $g'_{Low\ (SWI)}$. (c) Dirac measure for the level set representation of a mean shape, $\delta_0(u_0^*)$. (d) A new edge map, g_{new}.

Figure 3 shows a simple interpretation of $g'_{\text{High }(T_2W)}$, $g'_{\text{Low (SWI)}}$, $\delta_0(u_0^*)$, and g_{new} for a clear and an unclear edge in case of $\alpha < 0$ in 1D. $g'_{\text{Low (SWI)}}$ has wider boundary regions due to small β_{Low} and superior contrast on the SWI, compared with $g'_{\text{High }(T_2W)}$. Also, $\delta_0(u_0^*)$ is 1 on the boundary of the initial shape prior. g_{new} is computed as the weighted average of $g'_{\text{Low (SWI)}}$ and $g'_{\text{High }(T_2W)}$ with $\delta_0(u_0^*)$, capturing $g'_{\text{Low (SWI)}}$ on the boundary and $g'_{\text{High }(T_2W)}$ on the homogeneous region within the initial shape prior. Therefore, g_{new} has more detailed boundary information, when compared with $g'_{\text{Low (SWI)}}$ or $g'_{\text{High }(T_2W)}$.

Figure 4 shows the SWI and T_2W images in three orthogonal directions, corresponding to the Laplacian outputs, $g'_{\text{Low }(T_2W)}$ with $\alpha = 0.5$ and $\beta_{\text{Low}} = 8$, $g'_{\text{High (SWI)}}$ with $\alpha = 0.5$ and $\beta_{\text{High}} = 13$, δ_ε of a shape prior for the left external Globus Pallidus (GPe), and g_{new} on the ROI of the 2D axial slice. $g'_{\text{Low }(T_2W)}$ contains wider homogeneous regions, while $g'_{\text{High (SWI)}}$ has more detailed edge information. In particular, $g'_{\text{High (SWI)}}$ provides clearer separation of the left GPe and internal Globus Pallidus (GPi) (see red circle in Figure 4(h)). This is attributed to the superior contrast of the SWI, enabling the identification of thin boundaries (lamina pallid medialis) separating GPe and GPi (Abosch et al., 2010). Stronger boundaries are exhibited by the intensity transformation using g' with β_{High}. Finally, we observed that g_{new} (Figure 4(j)) shows clearer boundaries by weighted averaging of $g'_{\text{Low }(T_2W)}$ and $g'_{\text{High (SWI)}}$ with $\delta_\varepsilon(u_0^*)$ of ε=1. More specifically, edge information around the left GPe in g_{new} comes from boundaries

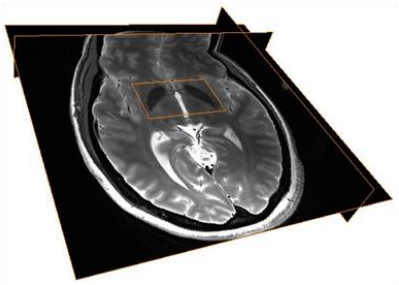

(a)

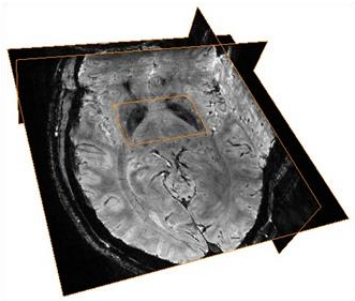

(b)

(c)

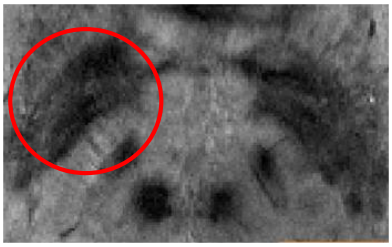

(d)

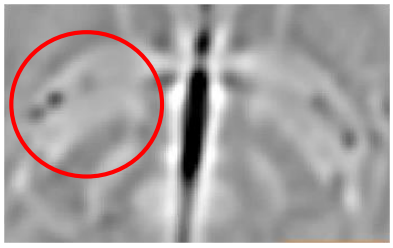

(e)

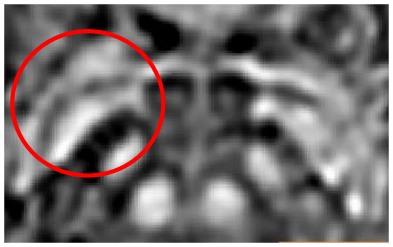

(f)

(g)

(h)

(i)

(j)

Figure 4: A new edge map generated by combining axial T_2W image with SWI. (a) Axial T_2W image. (b) Axial SWI. (c) ROI of T_2W image. (d) ROI of SWI. (e) Laplacian of smoothed T_2W image. (f) Laplacian of smoothed SWI. (g) $g'_{Low\ (T_2W)}$ with α=0.5, β_{Low}=8. (h) $g'_{High\ (SWI)}$ with α=0.5, β_{High}=13. (i) $\delta_\varepsilon(u_0^*)$ with ε=1. (j) g_{new}. Note that regions around left GPe and GPi (the red circle) in (j) are improved.

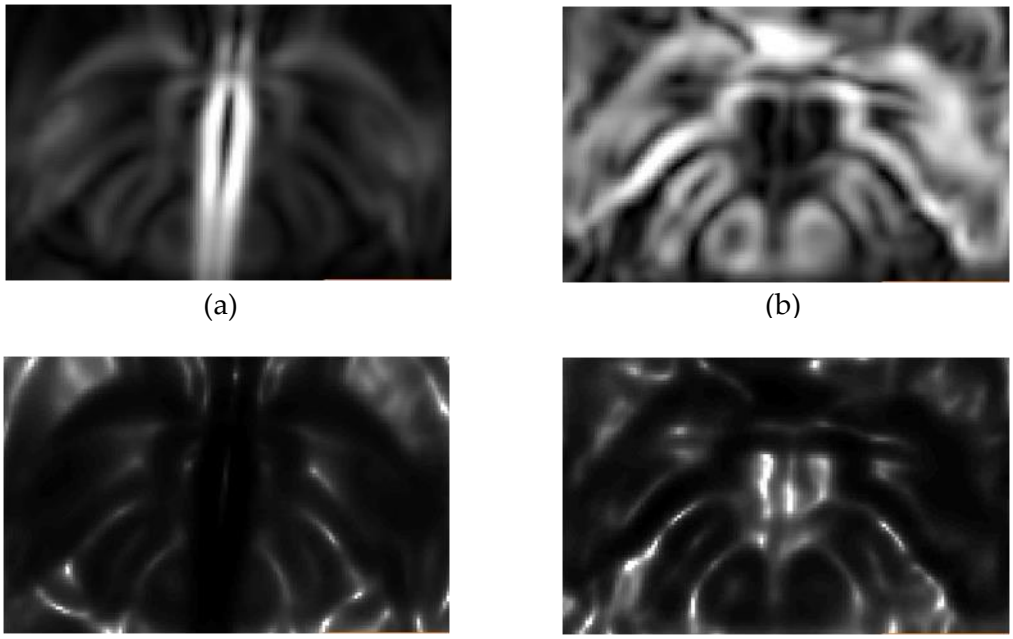

(a) (b)

(c) (d)

Figure 5: Image gradient magnitude of the SWI and T_2W images and their corresponding g in (2.2). (a) Gradient magnitude of smoothed T_2W. (b) Gradient magnitude of smoothed SWI. (c) g_{T_2W} (inverse of (a)). (d) g_{SWI} (inverse of (b)).

of $g'_{High\ (SWI),}$ and homogeneous region within the left GPe comes from $g'_{Low\ (T_2W)}$ if it is assumed that the intensity of $g'_{High\ (SWI)}$ on boundaries and $g'_{Low\ (T_2W)}$ on an homogeneous region within a given shape prior for left GPe on the initial position is ideally 0 and 1, respectively. On the other hand, $g'_{High\ (SWI)}$ and $g'_{Low\ (T_2W)}$ are averaged

with the weighting value $\delta_\varepsilon(u_0^*)$ on the region where $g'_{\text{High (SWI)}}$ is not 0 on the boundary or $g'_{\text{Low (T}_2\text{W)}}$ is smaller than 1 on the homogeneous region within a given shape prior for GPe (see gray scale region in Figure 4(j)). For comparison, the image gradient of each single modality image, SWI or T_2W image, and the corresponding g in (2.3) is presented Figure 5. The edge map produced by g does not have sufficient information, by comparison with the edge map generated by g_{new}. In particular, boundaries between the left GPe and GPi are not well identified. The new edge map introduced in this section is more accurate, integrating information from the T_2W and SWI images together with the shape prior.

2.2.4 Anatomical constraints between adjacent structures

Overlap between adjacent segmented objects is often inevitable even if the global shape information and the new edge indicator function discussed in the previous sections are employed. Anatomical constraints for non-overlap and adjacency should be considered for more accurate segmentation of the basal ganglia (Paragios and Deriche, 2000a; Zimmer and Olivo-Marin, 2005; Lucas et al., 2012) (such constraints can be imposed for other anatomical segmentation tasks as well). In this section, a global penalty term constraining the propagation of each adjacent surface to avoid overlaps is considered and incorporated into our extended active surface model.

2.2.4.1 Level set evolution with anatomical constraints

A pre-segmented version obtained from our model (e.g., segmented SN in Figure 6) is utilized as a repulsion constraint for its adjacent structures. This means the pre-segmented objects act as a global force in opposite direction to the shape priors (and edge and curvature) of their neighboring objects during the segmentation process. Furthermore, adjacent structures are iteratively segmented, avoiding overlapping regions between them by constraining the over-segmentation of their adjacent structures. During the iterative process, the structures are corrected in order to obtain clear boundaries between them and to maximize the Dice's Coefficient (DC) values defined as

$$\mathrm{DC} = \frac{2(\mathrm{V_A} \cap \mathrm{V_B})}{\mathrm{V_A} + \mathrm{V_B}}, \tag{2.17}$$

where $\mathrm{V_A}$ and $\mathrm{V_B}$ are the respective volumes of structures A and B to be compared for their similarity measurement.

We consider the resulting surface in (2.13), whose adjacent structure to be segmented exists, as u_{adj}. It is represented by level-sets using a signed distance function. u_{adj} is fixed at this step of the iteration, and the negative distance between u_{adj} and the current evolving surface u adjacent to it acts as the repulsion force during the segmentation process. The surface evolution equation in the negative direction of the

distance between u_{adj} and u is given by (at a given discrete time t and with the constant weight λ_3)

$$u(t+1) = u(t) - \lambda_3 \Big(u_{adj}(t) - u(t)\Big). \tag{2.18}$$

The surface evolution equation with non-overlapping constraints in (2.18) is incorporated into the update expression (2.13) with shape priors and g_{new} as introduced in the previous sections,

$$u(t+1) = u(t) + \lambda_1\big(u^*(t) - u(t)\big) + \lambda_2\big(g_{new}\,(c+H)|\nabla u(t)| + \nabla g_{new}\cdot \nabla u(t)\big) - \lambda_3 \Big(u_{adj}(t) - u(t)\Big). \tag{2.19}$$

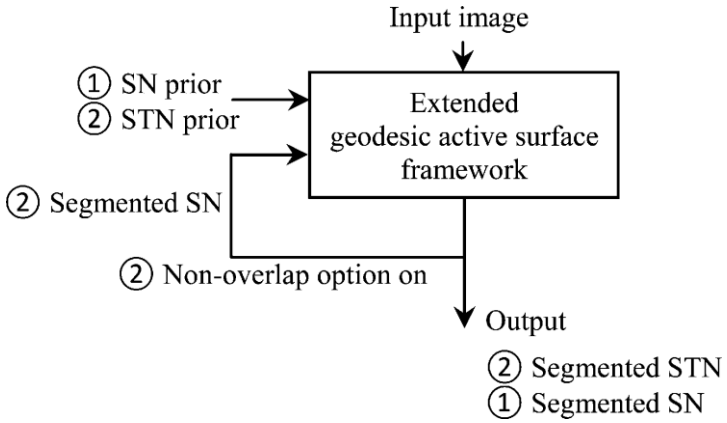

Figure 6: Iterative segmentation flow for SN and STN within modified GAS framework

2.2.4.2 Iterative process for non-overlapping structures

This process is iterated, so that different structures can be segmented using a specific set of non-overlapping constraints. Figure 6 shows such an iterative segmentation workflow for the substantia nigra (SN) and subthalamic nucleus (STN). First, SN is segmented without applying penalty for overlapping. If the structure does not have neighboring structures to be segmented, λ_3 is set to 0, disabling the non-overlap constraints. Initially segmented SN is utilized as the non-overlapping constraint to segment STN at the next iteration. Then, the segmented STN is also utilized to constrain and correct over-segmentation of SN. This process can be repeated until convergence (defined as the state where no significant changes in the segmentation of the desired structures occur, considering overlapping region and DC values at the same time). Variations of the SN and STN at each iteration are presented in Figure 7. Each structure is shown as a 2D contour on axial and coronal slices. Red, green, and blue contours represent segmented STN, segmented SN, and the "ground truth" (manual segmentation), respectively, for each structure. Initial segmentation results in Figure 7(a) show large overlapping regions, attributed to over-segmentation of each structure around unclear boundaries between SN and STN. The overlapping regions are considerably reduced, and segmentation results are corrected toward the ground truth, as the segmentation progresses.

Note that non-overlapping penalties can be additionally incorporated as the number of adjacent structures increases. For example, GPe has two adjacent structures - Pu and GPi (see Table 1) - and thus each structure is segmented with an initially segmented GPe. Segmentation of GPe at the next iteration is constrained by both pre-segmented Pu and GPi.

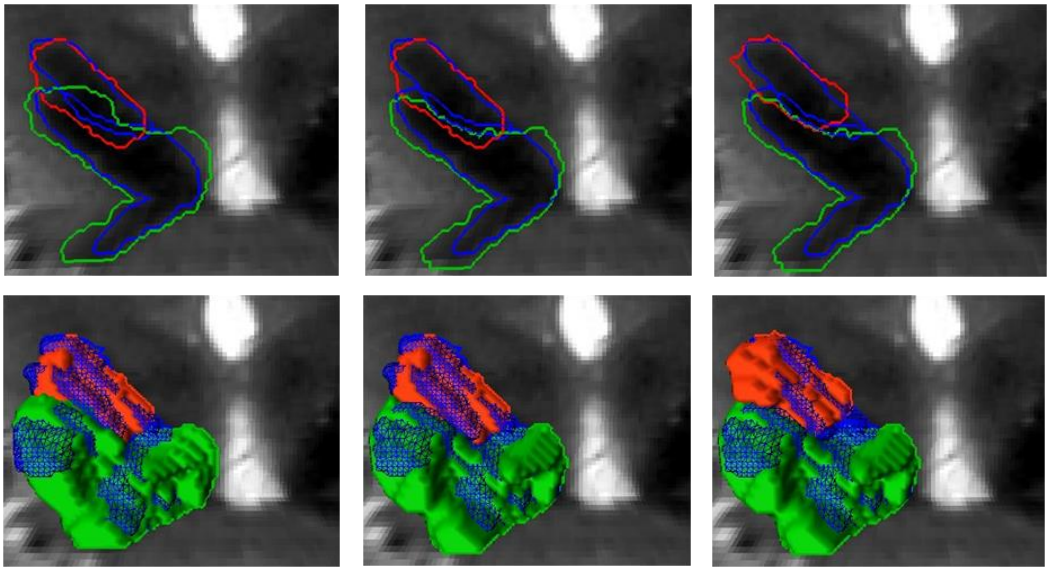

(a) (b) (c)

Figure 7: Segmentation results of SN and STN at each iteration. Top shows contours in both axial and coronal slices, and bottom represents the corresponding 3D structures. (a) First iteration: The green and red represent the first segmented SN without the constraint and the first segmented STN with the first SN, respectively. (b) Second iteration: The green and red represent the second segmented SN with the first STN and the first segmented STN with the first SN, respectively. (c) Third iteration: The green and red represent the second segmented SN with the first STN and the second segmented STN with the second SN, respectively. The blue represents manually segmented SN and STN.

Table 1: Corresponding non-overlapping constraints for each structure to be segmented

Structure	Overlapping constraints
GPe	GPi, Pu
GPi	GPe
SN	STN
STN	SN
CN	Tha
Pu	GPe
Tha	CN

The non-overlapping constraint introduced in this section improves the segmentation mostly for unclear boundaries between neighboring structures by providing each structure with global shape information about its neighboring structure, and the iteration process enables to further refine boundaries between those structures by the user intervention. Moreover, this could significantly aid in the segmentation when the input image has lower contrast or SNR such as in clinical 1.5T or 3T. In particular, this process is a critical feature for the accurate segmentation of basal ganglia structures to be presented in the next section.

2.3 Application to the segmentation of basal ganglia structures

2.3.1 Segmentation workflow

The workflow for the proposed semi-automatic volumetric segmentation process of the basal ganglia component and thalamus is shown in Figure 8. GPe and GPi are

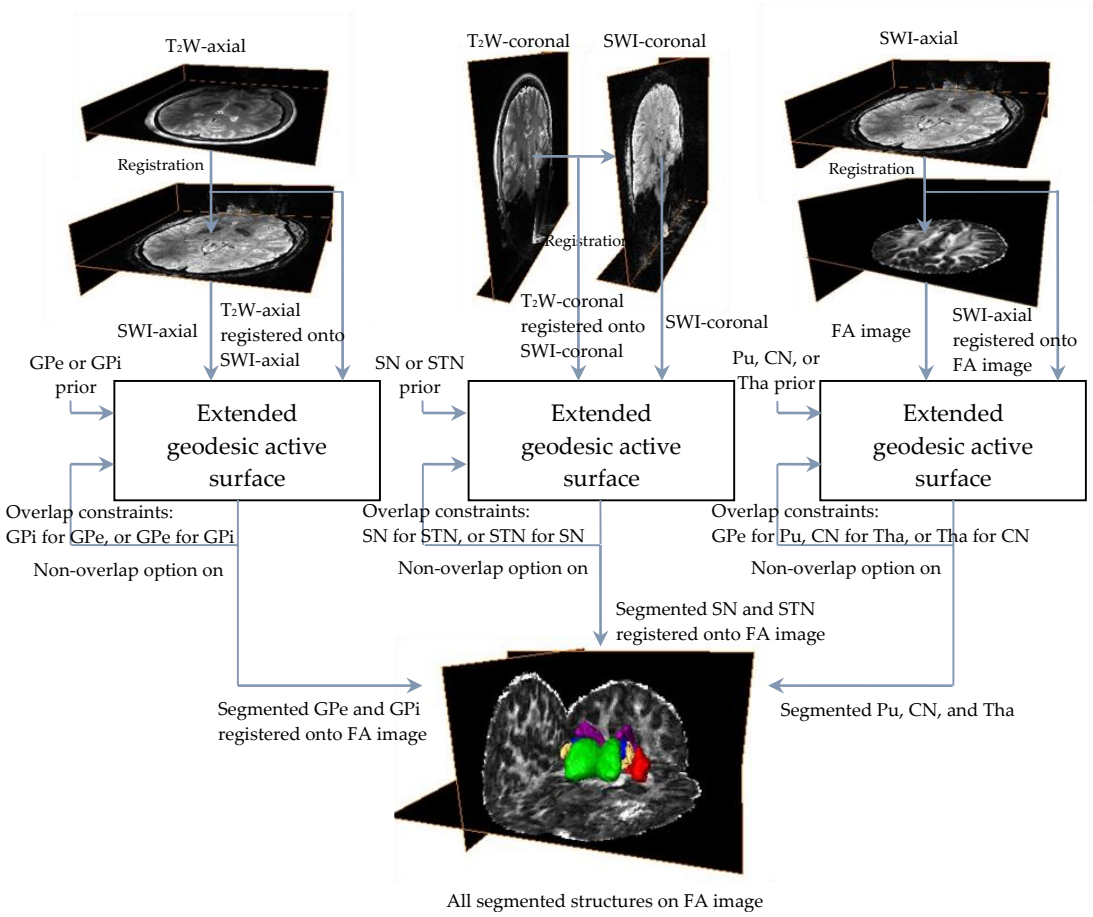

Figure 8: Schematic workflow for the semi-automatic 3D segmentation of basal ganglia components and thalamus.

segmented on the axial images since the *lamina pallid medialis* (Abosch et al., 2010) which represents boundaries between GPe and GPi is shown well in the axial SWI. SN and STN are segmented on the coronal images since this direction shows high contrast, allowing the delineation between SN and STN. Also, the FA image is utilized to segment Caudate Nucleus (CN), Putamen (Pu), and Thalamus (Tha). We fully utilize multi-modal images, combining SWI, T_2W, and FA from DWI to segment all the structures according to the

subject-specific analysis pipeline presented in Lenglet et al. (2012). More specifically, axial T_2W image registered onto the SWI, and axial SWI itself are utilized to generate an edge map for the segmentation of GPe and GPi. Coronal T_2W image registered onto the SWI, and coronal SWI itself, are utilized to segment SN and STN. CN, Pu, and Tha are segmented from the axial SWI registered onto the FA image, and the FA image itself.

2.3.2 Anatomical constraints between the basal ganglia structures

The training set for the shape priors consists of manual segmentations obtained from other subjects, or the same subject on other scan dates. Corresponding non-overlapping constraints for each structure are summarized in Table 1, considering the high probability of connection between neighboring structures presented in Lenglet et al. (2012). All segmented structures are finally overlapped on the desired modality after registration.

2.4 Experimental results

In this section, we present segmentation results of the basal ganglia component and thalamus on real 3D 7T MRI using our proposed method. Segmentation results are compared with those obtained with GAS (Caselles et al., 1997), GAS with shape priors (Leventon et al., 2000), GAS based on g′ in (2.14) with shape priors, GAS based on the optimal multi-modal image, g_{new} in (2.15), and our approach without non-overlapping constraints, validating the effects of the different GAS extensions in our proposed method. Additionally, we compare our proposed method with FSL FIRST (Woolich et al., 2009;

Patenaude et al., 2011) and FreeSurfer (Fischl et al., 2002, 2004), widely used single-modality tools for segmentation of sub-cortical regions. We quantitatively measure the performance of each approach using the DC (2.17) and visually analyze segmented volumes on the Amira software package (Visage Imaging), facilitating the simultaneous visualization of multiple structures.

2.4.1 Experimental environment

2.4.1.1 Implementation details

Our proposed method was implemented in the ITK/VTK framework which provides open source C++ libraries for image segmentation and registration. The implementation was also integrated into the 3D Slicer program (Pieper et al.), a free software package for image visualization and analysis. In particular, modularization of the implementation within the 3D Slicer program allows developers to test algorithms by tuning parameters easily and rapidly under the provided Graphical User Interface (GUI) environment. GAS (Caselles et al., 1997) and GAS with shape priors (Leventon et al., 2000) are currently available on ITK libraries and tested for the comparison. Our proposed method was built from ITK classes related to these approaches.

2.4.1.2 Data acquisition and preprocessing

We utilized five MRI datasets, including T_2W, SWI and FA (from DWI) on each one, scanned (under approved IRB) from five subjects using a 7T magnet at the Center for Magnetic Resonance Research of the University of Minnesota. Table 2 shows the used

training shape sets and manual segmentations as ground truth for each dataset and the corresponding subject. For each dataset (T_2W, SWI, and FA image) from 1 to 5, fourteen structures - left and right sides of GPe, GPi, SN, STN, CN, Pu, and Tha within the basal ganglia region - were manually segmented by an anatomical expert.

Dataset 6 is utilized to segment structures using training shapes (manually segmented structures) from all different subjects 1 to 5. Its segmentation results are evaluated only visually since manually segmented versions were not available. Also, sagittal T_1W data in addition to T_2W, SWI, and FA is included on dataset 6 to segment CN, Pu, and Tha, comparing our proposed model with FSL FIRST and FreeSurfer (note that they work only on T_1W data) (Woolrich et al., 2009; Patenaude et al., 2011; Fischl et al., 2002, 2004).

Detailed acquisition information for all datasets, the manual segmentation pipeline, and the registration process for each structure are presented in Lenglet et al. (2012).

Table 2: Training shape set and ground truth for each test and the corresponding subject

Test data set	Subject No.	Training shape set (each structure segmented manually from)	Ground truth (each structure segmented manually from)
1	1	2, 3, 4, 5	1
2	2	1, 3, 4, 5	2
3	3-a	1, 2, 4, 5	3
4	3-b	1, 2, 3, 5	4
5	4	1, 2, 3, 4	5
6	5	1, 2, 3, 4, 5	-

Training shape sets for the structures on each dataset are built by using the leave-one-out method (Siverman, 1986), e.g., training shape sets for test set 1 consist of manual segmentations for each structure from datasets 2, 3, 4, and 5, leaving the ones from dataset 1 out. Moreover, training shape sets for test sets 1, 2, and 5 are manually segmented versions from all the other subjects. The training shapes for each structure and the data are initially registered onto datasets within the same ROI using FSL FLIRT (FMRIB's Linear Image Registration Tool) (Jekinson et al., 2002), overlapping with structures to be segmented on the data. Alignment of training shapes by registration onto the test dataset is critical to capture variations between training shapes, dealing with the correspondence problem (Leventon et al., 2000). The variations in training shapes are measured by using PCA modeling (described in section 2.1.2) as the principle components. A shape prior is represented by shape (and pose) parameters (being estimated using a MAP approach) and the principle components, and guides the evolution of the surfaces toward the best fit.

Additionally, initial surfaces (i.e., coordinate points in three dimensional spaces) should be properly defined as a major part of the user intervention in our active surface based segmentation framework, and thus such surface points (e.g., three or four points within each target structure in this work) are chosen based on new edgemaps generated by exploiting multi-modal MRIs on each dataset in three dimensional space using the Amira visualization tool.

Finally, for the selection of the parameters (i.e., α_{low}, α_{high}, β_{low}, and β_{high}) generating the new edgemap and the weights of each constraint (e.g., propagation, shape prior, and non-overlapping penalty) for the surface evolution, one of the datasets is firstly used to specify such parameters. Initially set values are utilized for the segmentation of each structure from other datasets and then are tuned by quantitatively and visually evaluating the results.

2.4.2 Experimental results on the real MRI

2.4.2.1 Optimal combination of multi-modal MR images

Recently, direct visualization of deep brain sub-cortical structures by exploiting superior image contrast on high resolution SWI and T_2W at 7T was presented in Abosch et al., 2010 and Lenglet et al., 2012. Furthermore, Lenglet et al. (2012) provided the subject-specific analysis pipeline which enables localization of sub-cortical structures by combining a pair of SWI and T_2W or FA images (process done manually there). More specifically, GPe and GPi were manually segmented by combining axial SWI and T_2W images. Also, SN and STN were identified by combining coronal SWI and T_2W images. The FA image and axial SWI were simultaneously utilized to segment CN, Pu, and Tha. In this section, we investigate the optimal combination of multi-modal MR images, segmenting each structure on various combinations (e.g., T_2W+SWI, T_2W+FA, and FA+SWI), and quantitatively evaluating segmentation results from the one of datasets (note that intensity properties of single modal images are consistent over datasets).

For dataset 3, GPe and GPi are segmented using the corresponding training shapes and by three combinations, i.e., (1) axial SWI and axial T_2W image registered onto axial SWI, (2) axial T_2W image registered onto axial SWI and FA image registered onto axial SWI, and (3) axial SWI and FA image registered onto axial SWI. Also, SN and STN are segmented using the corresponding training shape set and by three combination, i.e., (1) coronal SWI and coronal T_2W image registered onto coronal SWI, (2) coronal T_2W image registered onto coronal SWI and FA image registered onto coronal SWI, and (3) coronal SWI and FA image registered onto coronal SWI. Finally, CN, Pu, and Tha are segmented using the corresponding training shapes and by three combinations, i.e., (1) axial SWI registered onto FA image and axial T_2W image registered onto FA image, (2) axial T_2W image registered onto FA image and FA image, and (3) FA image and axial SWI registered onto FA image.

Note that GPe, GPi, SN, and STN are manually segmented on the high resolution SWI and T_2W, while CN, Tha, and Pu are manually segmented on the low resolution FA image. Therefore, we utilized data registered onto higher resolution image (SWI) to segment GPe, GPi, SN, and STN and onto lower resolution data (FA) to segment CN, Tha, and Pu for more accurate comparison with the corresponding manual versions.

Moreover, each structure is iteratively segmented while applying the non-overlapping constraint, thereby reducing overlap with adjacent structures and maximizing the DC value within our proposed framework.

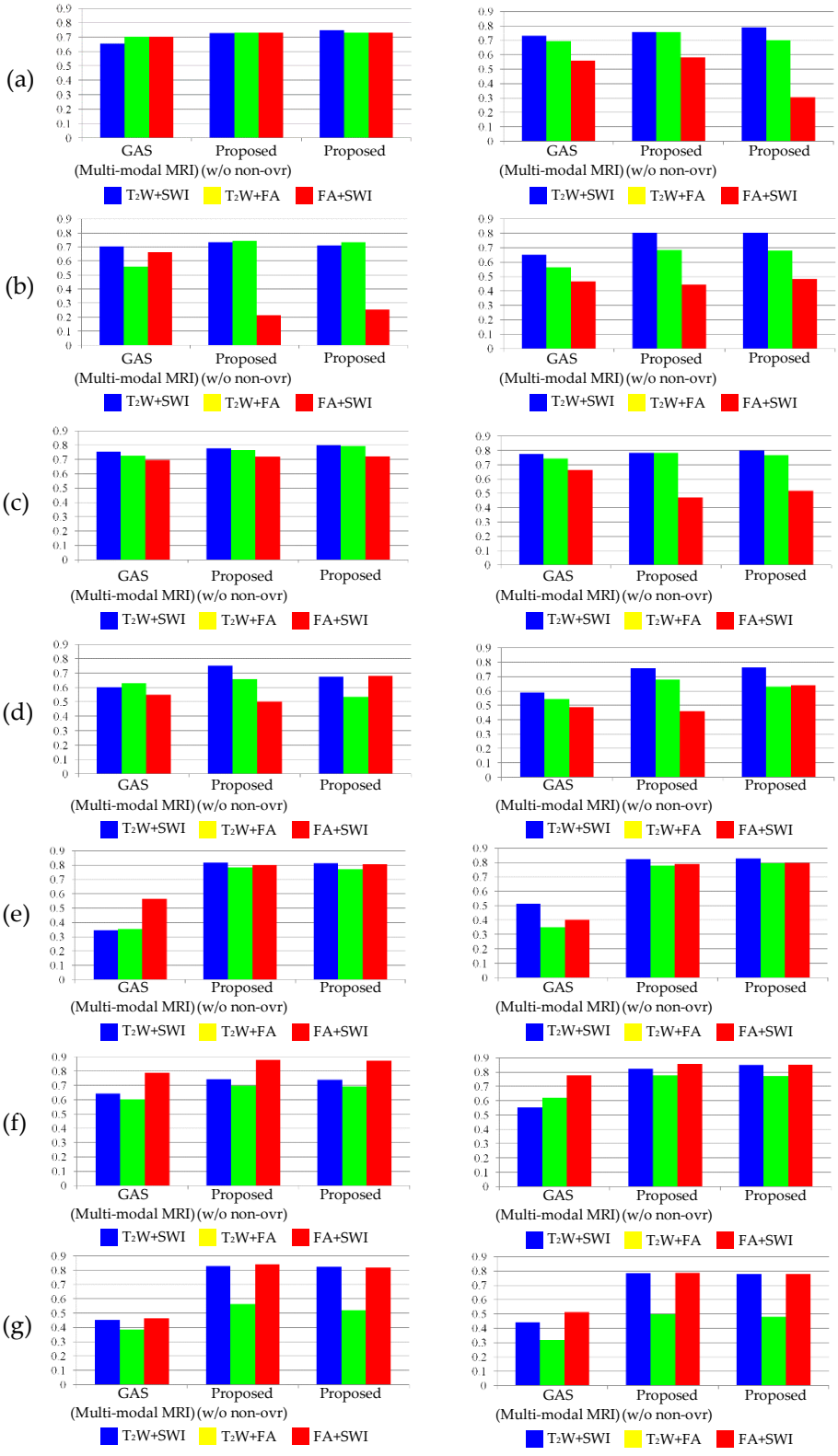
(a)
(b)
(c)
(d)
(e)
(f)
(g)
0.9
0.8
0.7
0.6
0.5
0.4
0.3
0.2
0.1
0
GAS
Proposed
Proposed
(Multi-modal MRI)
(w/o non-ovr)
T2W+SWI
T2W+FA
FA+SWI

Figure 9: DC values of segmentations from GAS and our proposed model (without and with non-overlapping constraints), based on three combinations of two single-modal images for each structure. (a) GPe. (b) GPi. (c) SN. (d) STN. (e) CN. (f) Tha. (g) Pu. The left and right columns represent left and right structures, respectively. The blue, green, and red represent the combination of T_2W and SWI, T_2W and FA, and FA and SWI, respectively.

For the comparison with our proposed segmentation method based on multi-modal images, we apply the multi-channel image based active contour model (Sapiro, 1996; Sandberg and Chan, 2005) to classical edge based active contour, thereby using two different contrast MR images. For that purpose, classical GAS is extended to utilize multi-modal images by employing a new edge indicator function introduced in our approach. All the structures are segmented using GAS, and using our proposed model without non-overlapping constraints, based on three combinations again. Finally, DC values between segmented structures and their corresponding manually segmented versions for each approach are calculated.

Figure 9 shows DC values between segmentations obtained from each approach based on three multi-modal MR combinations and their corresponding manual versions for each structure. We observe that our proposed approach based on combination of T_2W and SWI for GPe, GPi, SN, and STN yields better segmentation results than other combinations. In particular, overall segmentation results on FA image combined with SWI were inaccurate (see DC values for GPi and STN in our proposed model in Figure 9). On the other hand, CN, Tha, and Pu were more accurately segmented with the combination of FA and SWI than other combinations. Based on these experiments, we can see that SWI

provides additional anatomical details around GPe, GPi, SN, and STN regions; while T_2W identifies more clearly structural information within those ROIs than the FA image. For CN, Tha, and Pu, we can see that FA image provides more detailed anatomical information than T_2W image within the structures, and SWI still shows obvious boundaries around the regions. In addition, we can observe that shape priors and non-overlapping constraints within our proposed framework contributed to improve the overall segmentation accuracy (see DC values between tested approaches on the combination of T_2W and SWI for GPe, GPi, SN, and STN, and on the combination of FA and SWI for CN, Tha, and Pu in Figure 9).

2.4.2.2 Quantitative and visual evaluation

Segmentation results from our proposed model based on the optimal combination of multi-modal images (as described in the previous section) for each of the structures on the datasets from 1 to 5 in Table 2 are presented in this section. More specifically, GPe and GPi are segmented using the corresponding training shapes and by combining axial SWI and axial T_2W images registered onto axial SWI. SN and STN are segmented using the corresponding training shape set, and by combining coronal SWI and coronal T_2W images registered onto coronal SWI. CN, Pu, and Tha are segmented using the FA image and axial SWI registered onto the FA image with corresponding training shape set. For the comparison, all the structures are also segmented using GAS, GAS with shape priors, GAS based on g' with shape priors, based on the single-modality image, and GAS based on

multi-modal images. In particular, for approaches using the single modal image, GPe and GPi are segmented on the axial T_2W image registered onto axial SWI or the axial SWI, respectively. Similarly, SN and STN are segmented on coronal T_2W images registered onto coronal SWI or coronal SWI. Also, the FA image or axial SWI registered onto the FA image are utilized to segment CN, Pu, and Tha. Finally, DC values between segmented structures and their corresponding manually segmented versions for each approach are calculated.

Segmentation results for dataset 3 (similar results are obtained for the other data), represented as 2D contours with superimposed ground truth (blue contour) and 3D volumes, for each structure, are shown using the Amira environment in Figures 10-13. In particular, for segmentation results based on multi-modal images (Figures 10-11 (d)-(f) and 13), we present color maps (on the manual segmentation) representing surface distances between each segmentation result and its manual one for more clear visual comparison. Figure 14 shows the 3D manual segmentation on the same dataset 3.

DC values of each segmented result for datasets 1–5 during the non-overlapping iterative process are summarized in Table 3. In addition, Figure 15 presents average DC values and standard deviation errors for all the structures and tested segmentation algorithms on datasets 1–5.

In Figures 10-11 (a)-(c) and 12 we observe that the segmentation results are visually improved by incorporating the shape prior term. Moreover, more accurate segmentation

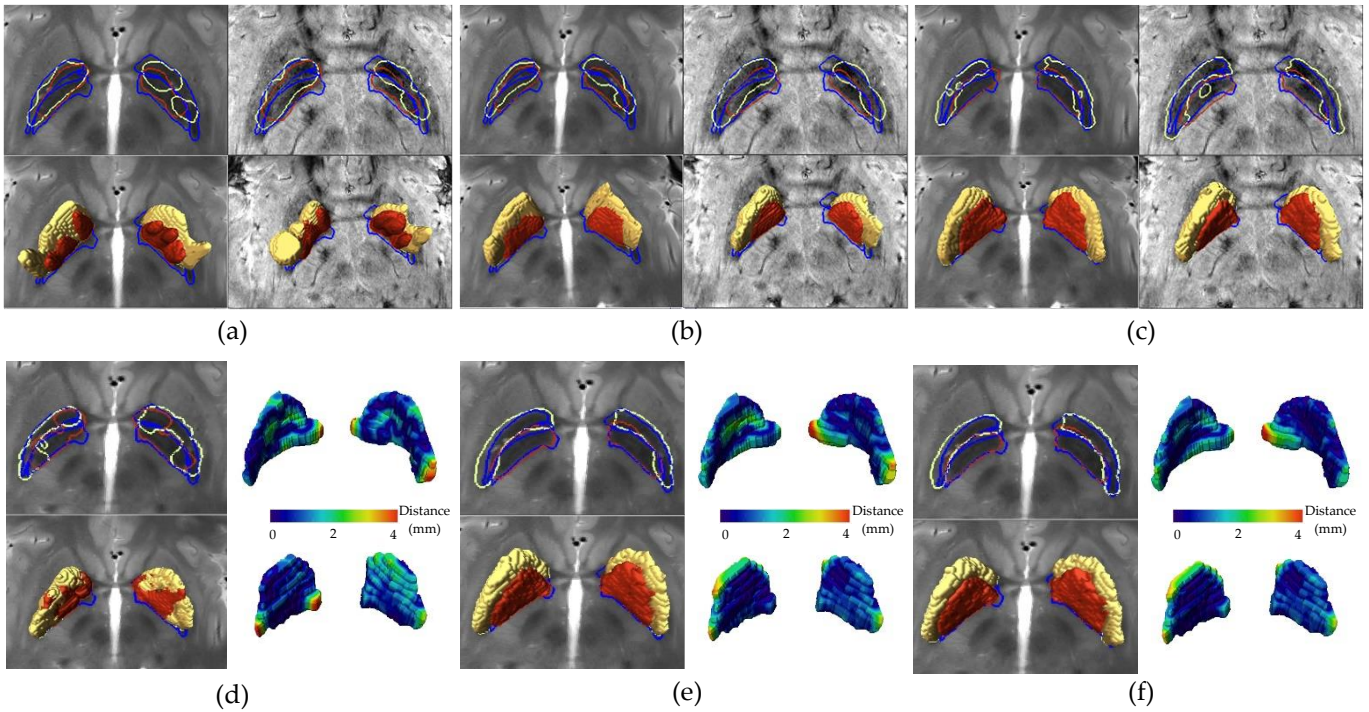

Figure 10: Comparison of segmentation results for GPe and GPi on dataset 3. The light green and brown represent GPe and GPi, respectively. The blue contours represent manual segmentations. Top and bottom in each figure represent contours and volumetric segmentations, respectively. Figures (a), (b), and (c) show segmentation results of GAS, GAS with shape prior using g, GAS with shape prior using g′ on axial T_2W image (left column) and axial SWI (right column), respectively. Figures (d), (e), and (f) are segmentation results of GAS, the proposed approach without non-overlapping constraints, and the proposed approach, respectively, with surface distance maps (right column, top: GPe, bottom: GPi) on axial T_2W image combined with axial SWI.

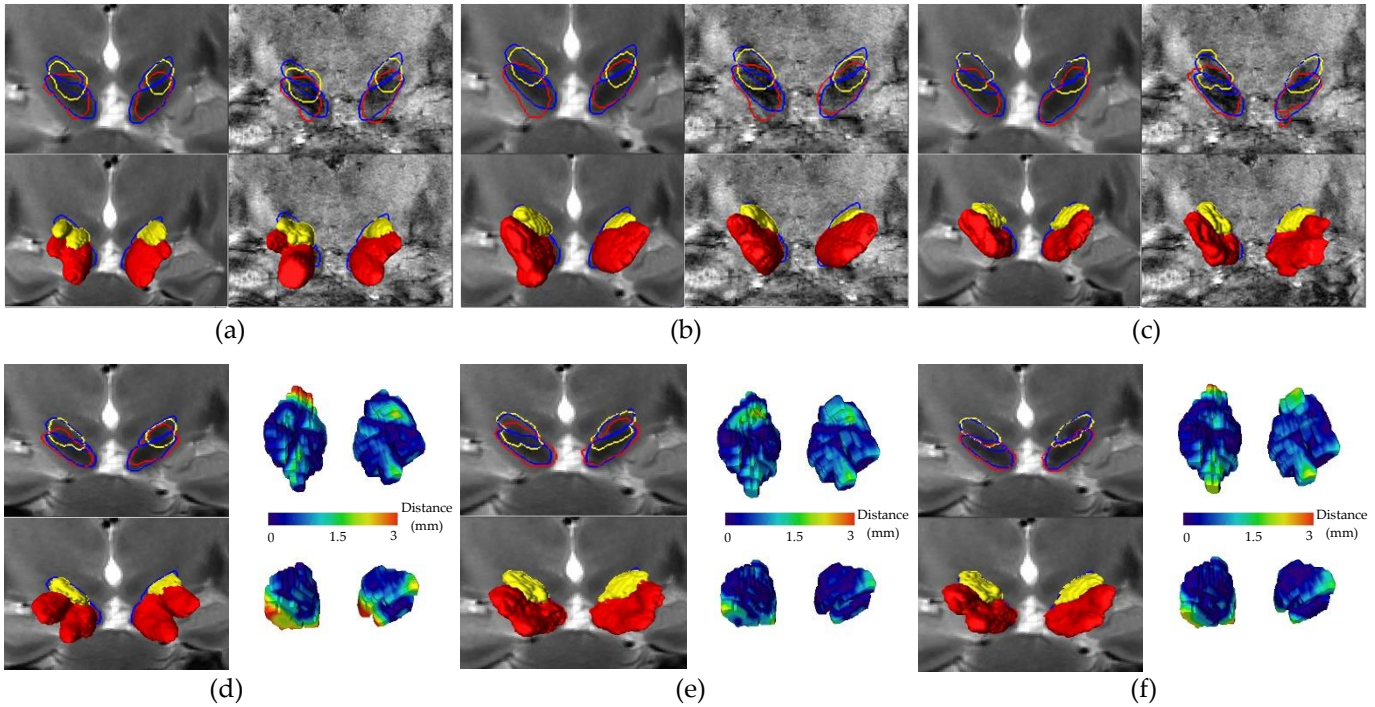

Figure 11: Comparison of segmentation results for SN and STN on dataset 3. The red and yellow represent SN and STN, respectively. The blue contours represent manual segmentations. Top and bottom in each figure represent contours and volumetric segmentations, respectively. Figures (a), (b), and (c) show segmentation results of GAS, GAS with shape prior using g, GAS with shape prior using g′ on coronal T_2W image (left column) and coronal SWI (right column), respectively. Figures (d), (e), and (f) are segmentation results of GAS, the proposed approach without non-overlapping constraints, and the proposed approach, respectively, with surface distance maps (right column, top: SN, bottom: STN) on coronal T_2W image combined with coronal SWI.

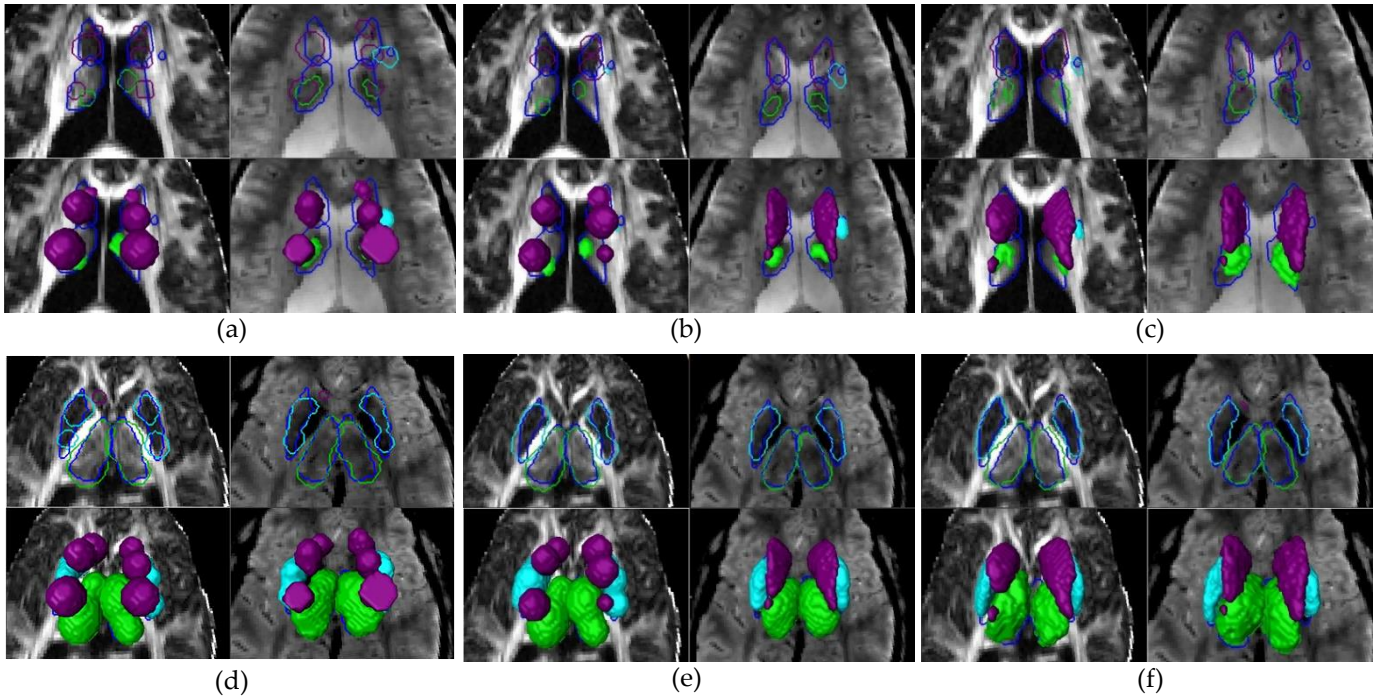

Figure 12: Comparison of segmentation results from the single-modality based approaches for CN, Tha, and Pu on dataset 3. The violet, dark green, and cyan represent CN, Tha, and Pu, respectively. The blue contours represent manual segmentations. Top and bottom in each figure represent contours and volumetric segmentations, respectively. Figures (a), (b), and (c) show segmentation results in the one view of CN and Tha from GAS, GAS with shape prior using g, and GAS with shape prior using g' on FA image (left column) and SWI (right column), respectively. Figures (d), (e), and (f) are segmentation results in another view of CN, Tha, and Pu from GAS, GAS with shape prior using g, GAS with shape prior using g' on FA image (left column) and SWI (right column), respectively.

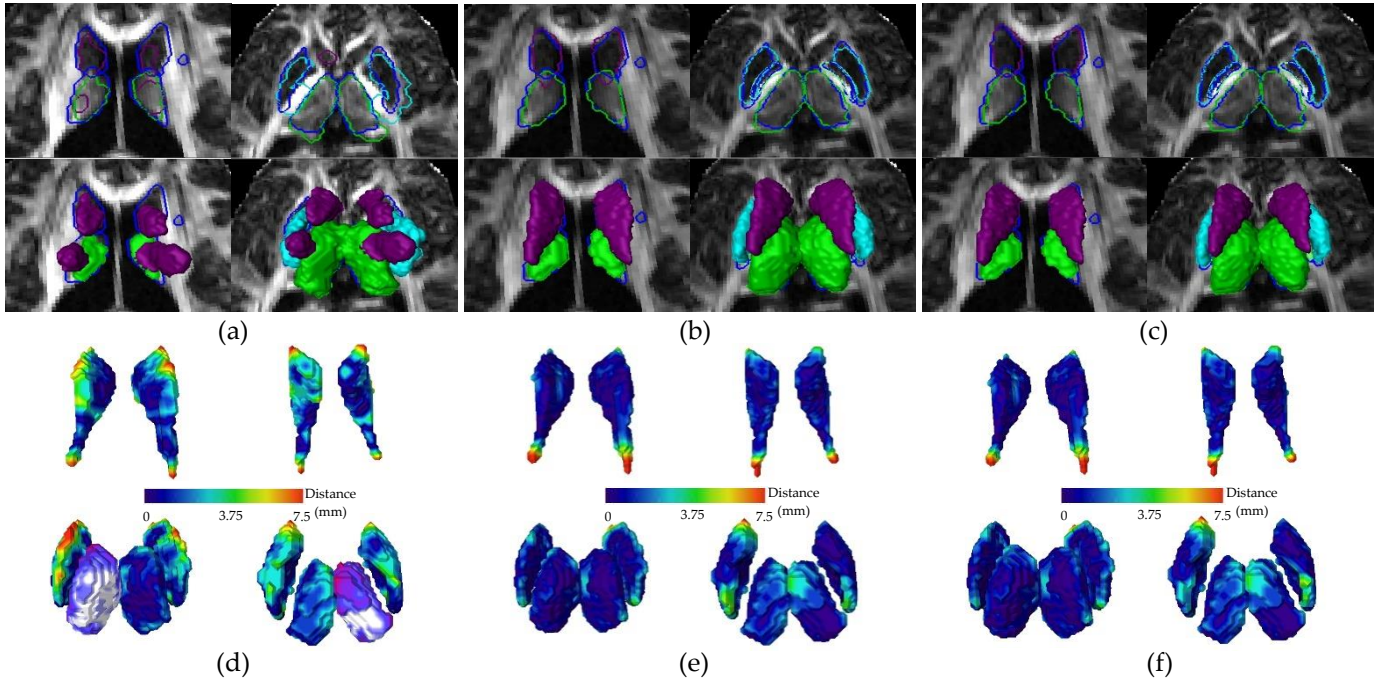

Figure 13: Comparison of segmentation results from the multi-modality based approaches for CN, Tha, and Pu on dataset 3. Figures (a), (b), and (c) show segmentation results in the one view (left) of CN and Tha and another view (right) of CN, Tha, and Pu from GAS, the proposed approach without non-overlapping constraints, and the proposed approach, respectively, on the FA image combined with axial SWI. The violet, dark green, and cyan represent CN, Tha, and Pu, respectively. The blue contours represent manual segmentations. Top and bottom in each figure represent contours and volumetric segmentations, respectively. GPe (light green) segmented on T_2W combined with SWI (i.e., segmented GPe in Figure 10(f)) is incorporated as contours in (b) and (c), respectively, to see overlaps between Pu and GPe. Note that overlaps between Pu and GPe in (c) are considerably reduced (see top right of (b) and (c)). Figures (d), (e), and (f) are corresponding surface distance maps (Top: CN, bottom: Pu and Tha, left: top view, right: bottom view).

results are obtained when using the new edge detection function (see Figures 10-11 (d)-(f) and 13). Note that segmentation results from GAS based on multi-modal images show better performance (yielding higher DC values) than those from GAS and even GAS with a shape prior term on the single-modal image (see GPe and SN in Figure 15). However, its segmented surfaces are unrefined since it does not exploit prior shape information (see Figures 10-11(d) and 13(a)). Overall results still includes over- and under-segmented areas and overlapping regions between neighboring structures, whereas our complete approach shows significantly improved segmentation results with reduced overlapping regions (see Figures 10-11(f) and 13(c) and (f) and especially, their surface distance maps on the overlapping regions). Additionally, our approach yields overall higher DC values (See Figure 15).

We also observe that while the DC values for left STN, right SN, CN, and Pu with a single-modality image (using GAS based on g or g′ with shape priors) are similar to those of our approach, their visual segmentation results were inaccurate due to underand oversegmentation and overlapping regions between neighboring structures (see Figures 11(b) and (c) and 12(b), (c), (e), and (f)]. Furthermore, the proposed approach with non-overlapping constraints yields significantly reduced overlapping regions between neighboring structures even though their DC values are similar to those without non-overlapping penalty. Specifically, overlapping regions between SN and STN segmented using our proposed approach were significantly reduced, comparing to those without

non-overlapping penalty (see Figures 11(e) and (f)), whereas their DC values are similar to or even slightly lower than those without non-overlapping penalty (e.g., 0.67 (0.7 without non-overlapping) for left STN and 0.76 (0.76 without non-overlapping) for right STN on dataset 3).

In addition, overall DC values are increased or maintained during the iterative segmentation process within our approach (see Table 3). In the few cases where the DC values are reduced after iteration, we still note that our approach shows clear delineation between adjacent structures, whereas manual segmentations have overlapping regions (also see Figure 11(f) and DC values of left SN and STN on dataset 3 in Table 3). This means that those manual segmentations were not completely well defined around boundaries, even if they were produced by an anatomy specialist.

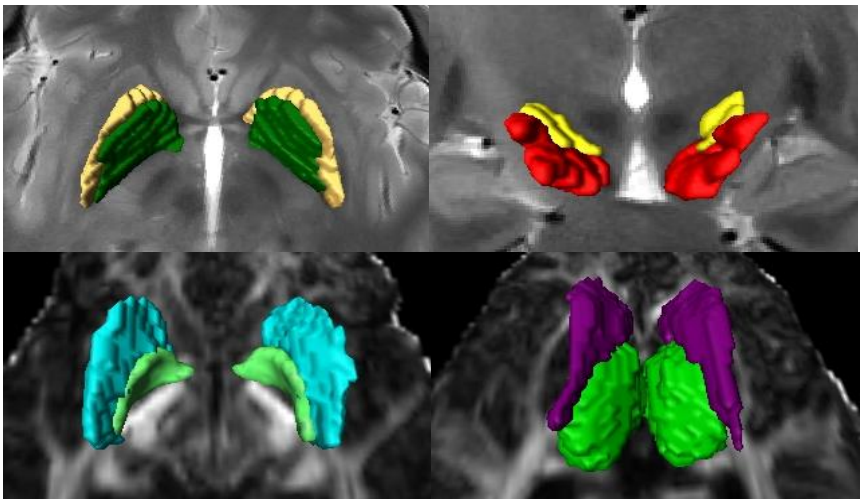

Figure 14: Manual segmentations for each structure on dataset 3. Top left shows GPe (light green) and GPi (brown) on the axial T_2W. Top right represents SN (red) and STN (yellow) on the coronal T_2W. Bottom left shows Pu (cyan) and GPe (light green) on the FA image. Bottom right represents CN (violet) and Tha (dark green) on the FA image.

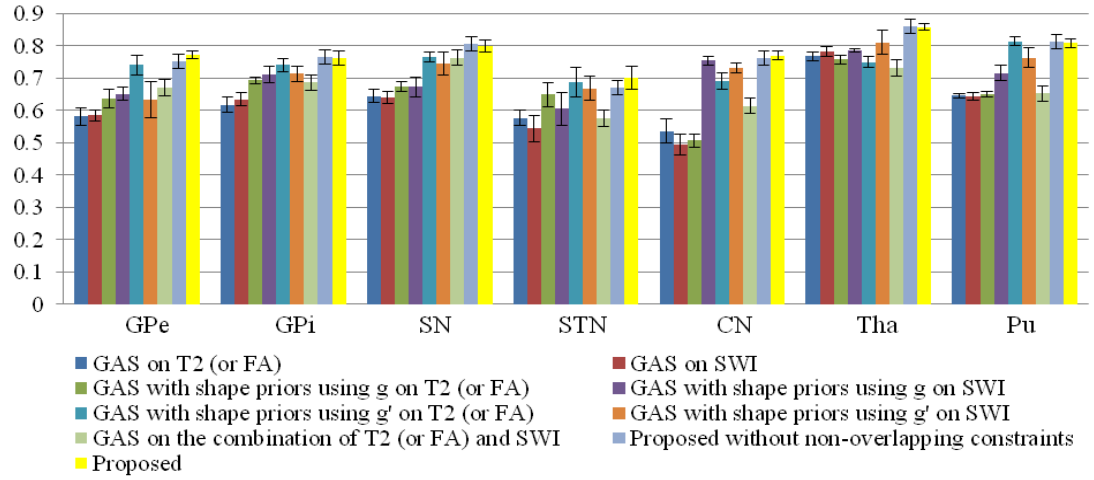

(a)

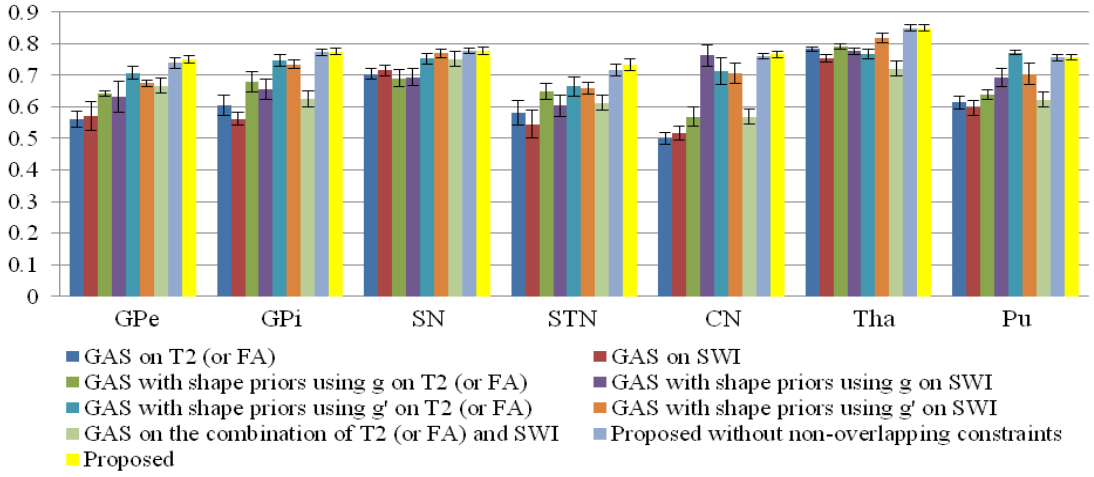

(b)

Figure 15: Average DC values and standard deviations of segmented results for each approach on data set from 1 to 5. Figures (a) and (b) represent DC values for left and right structures, respectively.

Table 3: DC values of the proposed approach during the iterative process for each data set

Data	Iteration	GPe Left	GPe Right	GPi Left	GPi Right	SN Left	SN Right	STN Left	STN Right	CN Left	CN Right	Tha Left	Tha Right	Pu Left	Pu Right
1	1st	0.754(F)	0.686	0.757	0.743(F)	0.834	0.752	0.617(F)	0.665(F)	0.779	0.739	0.837(F)	0.856(F)	0.784	0.744
	2nd	0.755	***0.715***	***0.727***	***0.742***	***0.841***	***0.757***	0.63	***0.688***	***0.783***	***0.743***	***0.839***	***0.857***	***0.784***	***0.744***
	3rd	***0.754***	-	-	-	-	-	***0.638***	-	-	-	-	-	-	-
2	1st	0.774(F)	0.741	0.819	0.775(F)	0.82(F)	0.796(F)	0.768	0.732	***0.721***	0.762	***0.85(F)***	0.809(F)	0.82	0.739
	2nd	***0.78***	***0.742***	***0.82***	***0.784***	0.82	***0.793***	***0.802***	***0.72***	-	***0.762***	-	***0.811***	***0.82***	***0.739***
	3rd	-	-	-	-	***0.804***	-	-	-	-	-	-	-	-	-
3	1st	0.728(F)	0.789	0.622	0.803(F)	0.786	0.765	0.751(F)	0.757(F)	0.799(F)	0.791(F)	0.872	0.851	0.817	0.78
	2nd	0.737	***0.791***	***0.711***	***0.804***	0.812	0.768	0.686	0.743	0.803	0.784	0.872	***0.851***	***0.817***	***0.78***
	3rd	***0.748***	-	-	-	***0.8***	***0.801***	***0.673***	***0.763***	***0.805***	***0.798***	***0.872***	-	-	-
4	1st	0.817	0.755	0.816(F)	0.783(F)	0.789(F)	0.752	0.724	0.711(F)	0.772	0.764	0.889(F)	0.856(F)	0.85	0.78
	2nd	***0.817***	***0.75***	0.802	***0.765***	0.785	0.75	0.73	0.719	0.773	***0.765***	0.887	***0.855***	***0.85***	***0.78***
	3rd	-	-	***0.80***	-	***0.752***	***0.757***	***0.69***	***0.761***	***0.775***	***-***	***0.888***	-	-	-
5	1st	0.745	0.752	0.749(F)	0.764(F)	Coronal SWI and T2W data were not available				0.763	0.763	0.844(F)	0.872(F)	0.774	0.744
	2nd	0.759	***0.751***	0.753	***0.781***					***0.764***	***0.763***	***0.842***	***0.872***	***0.774***	***0.744***
	3rd	***0.762***	-	***0.75***	-					-	-	-	-	-	-

(F) indicates the first segmented one for adjacent structures, and bold italic numbers (blue) are final DC values after iteration. Note that segmentation for SN and STN on data set 5 was not tested since coronal data was not available.

Next, we work with dataset 6, where the ground truth is not available and thus it requires only qualitative evaluation. Particularly, this dataset includes T_1W image. We further compare commonly used segmentation tools (e.g., FSL FIRST and FreeSurfer), which work on only this modal MR image, with our proposed framework based on the combination of T_1W image and another single-modal MR image, especially for CN, Pu, and Tha structures. Similarly in previous experiments, we performed experiments using our proposed model by combining the T_2W image and SWI to segment GPe, GPi, SN, and STN in axial and coronal directions, respectively. The FA image, registered onto higher resolution SWI, is combined with SWI to segment CN, Pu, and Tha. In particular,

segmented CN, Pu, and Tha are visually compared with those obtained by using the low resolution FA image on dataset 3 to see whether the low resolution FA image affects the segmentation accuracy. Additionally, GAS based on multimodal images is tested for the comparison. Figures 16–18 show the results, demonstrating the improvements obtained with our proposed approach. We observed that the segmentation results on dataset 6 are comparable with the results on dataset 3 even if training shapes from all the different subjects were simultaneously employed. Also, we can see that CN, Tha, and Pu segmented on the higher resolution FA image combined with SWI provides more accurate and detailed structural information than those segmented on the lower resolution FA image combined with SWI.

In addition, we tested our proposed model and GAS (extended to utilize multimodal images) on sagittal T_1W data (registered onto axial SWI) combined with T_2W, SWI, or FA image, comparing with FSL FIRST and FreeSurfer, widely used single-modality segmentation tools. We should note that FSL FIRST and FreeSurfer do not work on T_2W, SWI, or FA image, which provides more anatomical information than T_1W within sub-cortical structures (Abosch et al., 2010) and do not segment GPe, GPi, SN, and STN. Therefore, T_1W image was applied and tested to segment only CN, Pu, and Tha. Also, we visually compared with GAS, GAS with shape priors, and GAS based on g′ with shape priors on single T_1W data, respectively (see Figure 19). Figure 20 shows segmentation results of FSL FIRST and FreeSurfer on T_1W data.

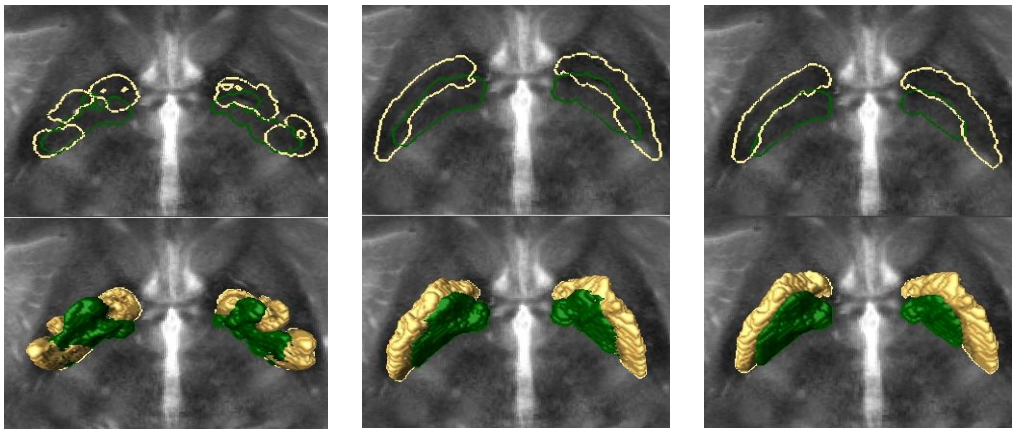

(a) (b) (c)

Figure 16: Comparison of segmentation results from the multi-modality based approaches for GPe and GPi on dataset 6. The light green and brown represent GPe and GPi, respectively. Top and bottom in each figure represent contours and volumetric segmentations, respectively. Figures (a), (b), and (c) show segmentation results of GAS, the proposed approach without non-overlapping constraints, and the proposed approach, respectively, on the axial T_2W image combined with axial SWI.

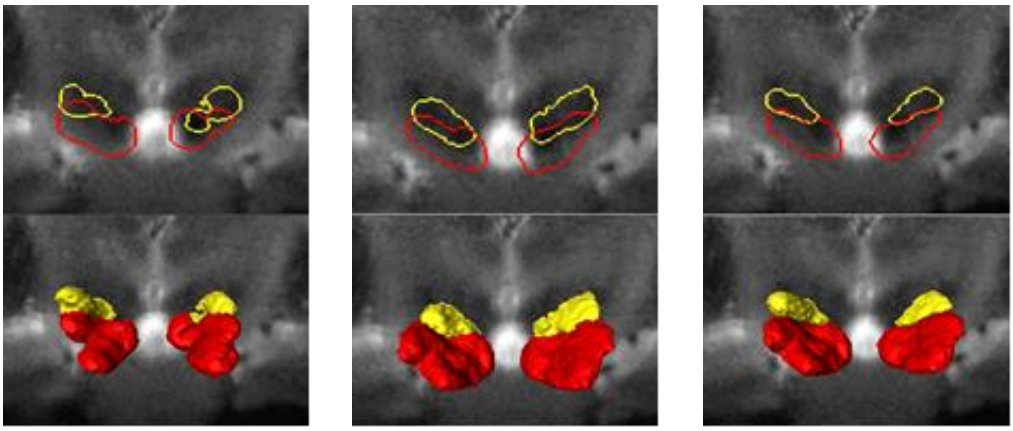

(a) (b) (c)

Figure 17: Comparison of segmentation results from the multi-modality based approaches for SN and STN on dataset 6. The red and yellow represent SN and STN, respectively. Top and bottom in each figure represent contours and volumetric segmentations, respectively. Figures (a), (b), and (c) show segmentation results of GAS, the proposed approach without non-overlapping constraints, and the proposed approach, respectively, on the coronal T_2W image combined with coronal SWI.

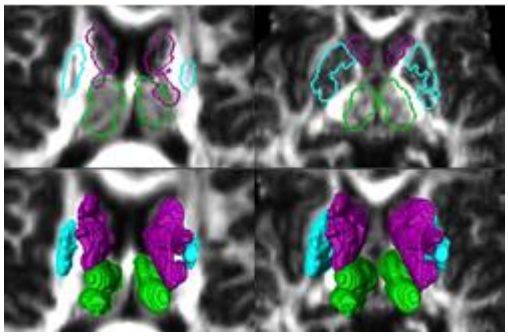

(a)

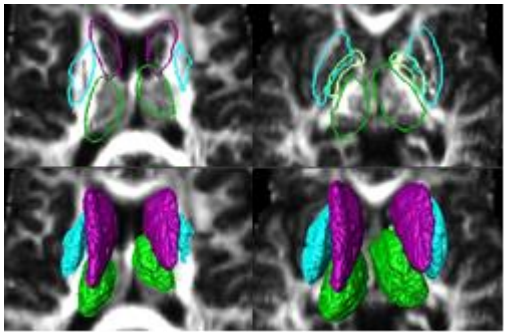

(b)

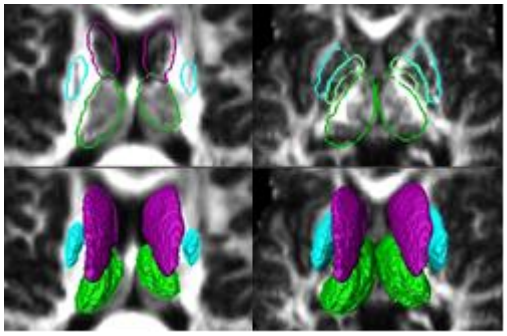

(c)

Figure 18: Comparison of segmentation results from the multi-modality based approaches for CN, Tha and Pu on dataset 6. The violet, dark green, and cyan represent CN, Tha, and Pu, respectively. Top and bottom in each figure represent contours and volumetric segmentations, respectively. Figures (a), (b), and (c) show segmentation results in the one view (left column) and another view (right column) of CN, Tha, and Pu from GAS, the proposed approach without non-overlapping constraints, and the proposed approach, respectively, on the FA image combined with axial SWI. GPe (The light green) segmented on T_2W combined with SWI (i.e., segmented GPe in Figure 16(c)) is incorporated as contours in (b) and (c), respectively, to see overlaps between Pu and GPe. Note that overlaps between Pu and GPe in (c) are considerably reduced (see top right of (b) and (c)).

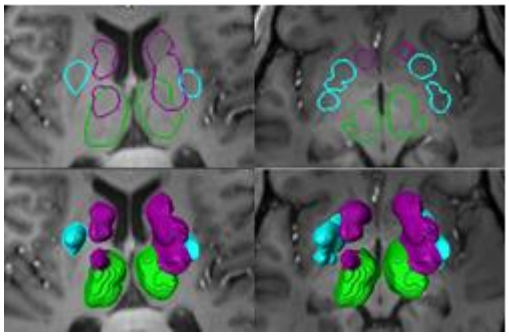

(a)

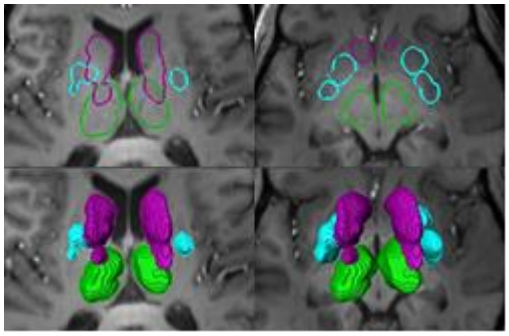

(b)

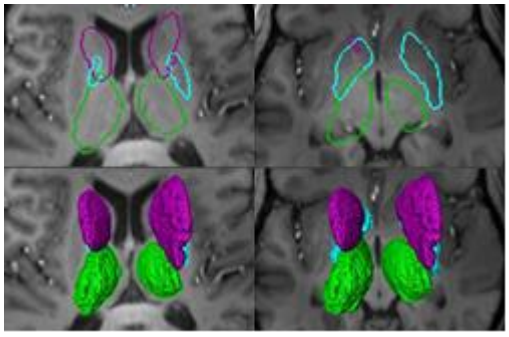

(c)

Figure 19: Comparison of segmentation results from the single-modality based approaches on T_1W image for CN, Tha, and Pu (dataset 6). The violet, dark green, and cyan represent CN, Tha, and Pu, respectively. Top and bottom in each figure represent contours and volumetric segmentations, respectively. Figures (a), (b), and (c) show segmentation results of GAS, GAS with shape prior using g, and GAS with shape prior using g' on T_1W image, respectively. Two views for CN, Tha, and Pu are shown in left and right columns.

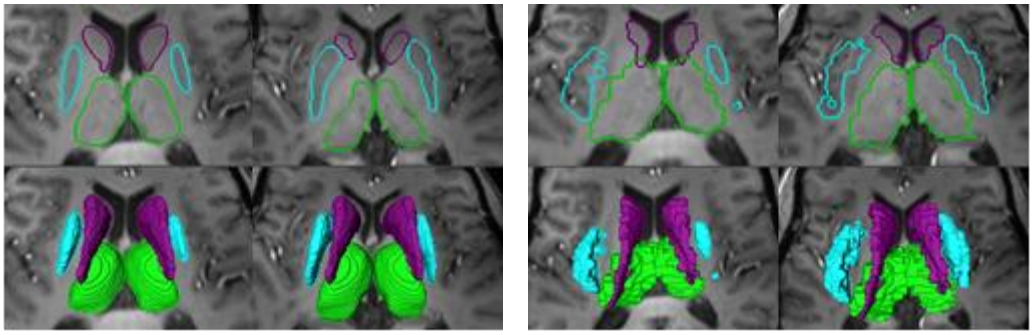

(a) (b)

Figure 20: Segmentation results from FSL FIRST and FreeSurfer on T_1W image for CN, Tha, and Pu (dataset 6). The violet, dark green, and cyan represent CN, Tha, and Pu, respectively. Top and bottom in each figure represent contours and volumetric segmentations, respectively. Figures (a) and (b) show segmentation results of FSL FIRST and FreeSurfer, respectively. Two views for CN, Tha, and Pu are shown in left and right columns.

We observe that the obtained FSL FIRST segmentation results are qualitatively better when compared with other previous techniques, including our proposed model tested here (see segmentation results of FSL FIRST in Figure 20(a)), while segmentation results obtained using FreeSurfer include incorrectly segmented regions (see left Pu regions in Figure 20(b)). Note that segmentation outputs (in the FreeSurfer space) should be registered onto the test data. We should note that both approaches are based on probabilistic learning models, which require a highly computational cost for segmentation (Fischl et al., 2002, 2004; Woolrich et al., 2009; Patenaude et al., 2011) while our model extends classical and simple edge-based segmentation model. For example, FSL FIRST takes over 15 min to segment CN, Tha, and Pu (including two-stage registration of test

data onto the MNI152 template (Patenaude et al., 2011)). Moreover, FreeSurfer works only for the whole brain segmentation, taking over 10 h.

On the other hand, our approach requires few minutes per each structure. Note that the preprocessing (e.g., registration of training sets onto test data and between two single-modal MR images) can be also initially performed within a few minutes prior to the segmentation.

Our approach shows qualitatively comparable results, which demonstrates that the segmentation performance on only the low contrast T_1W data is improved by the new edge indicator function, exploiting detailed edge information of SWI or FA image (see Figure 21(g)-(i)) with a prior shape model and non-overlapping constraints. We also observe that the segmentation results on the combination of FA image and SWI (considered as the optimal combination in the previous section) exhibit better performance than those of T_1W combined with FA image, SWI, and T_2W image (see Figures 18(c) and 21(g)–(i)).

To conclude, in this experiment, we have demonstrated that the combination of edge map from multimodal images, shape priors, and non-overlapping constraints within our proposed approach contributes to clear improvements on the quality of sub-cortical structures segmentation.

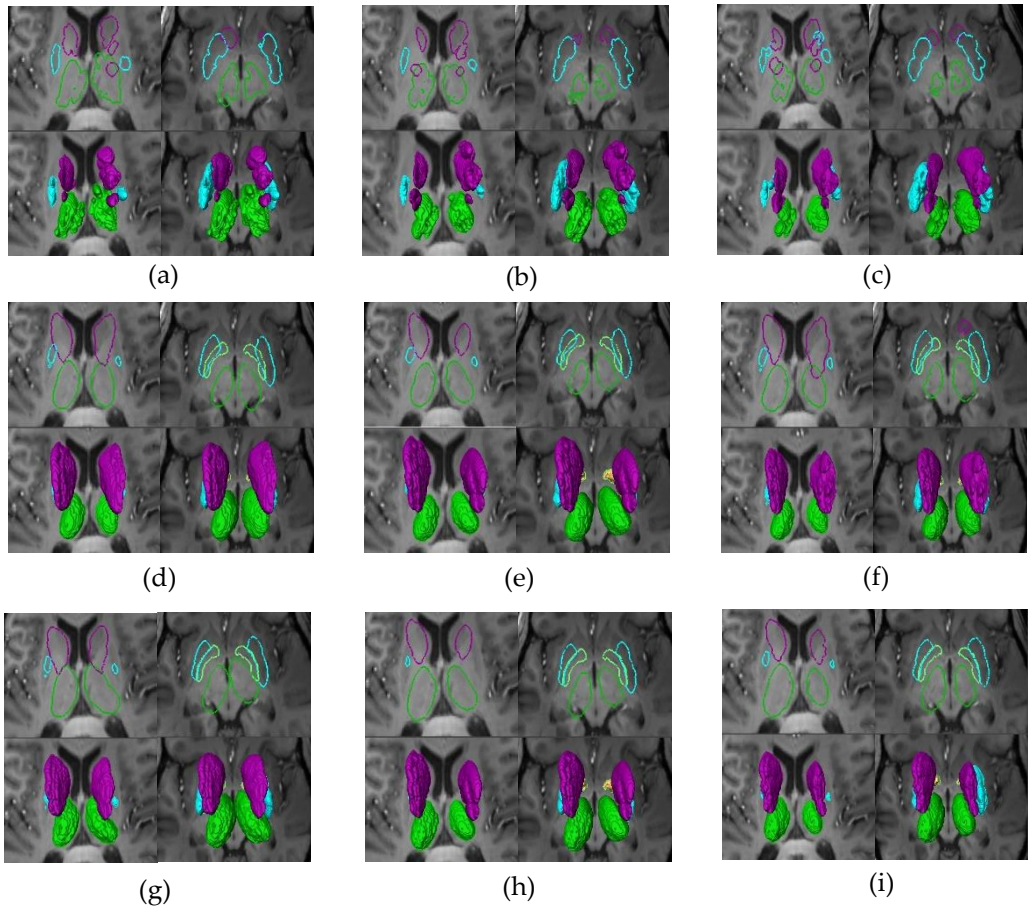

Figure 21: Comparison of segmentation results from the multi-modality based approaches on T_1W data combined with FA image, SWI, or T_2W image for CN, Tha and Pu (dataset 6). The violet, dark green, and cyan represent CN, Tha, and Pu, respectively. Top and bottom in each figure represent contours and volumetric segmentations, respectively. First row (i.e., figures (a), (b), and (c)) show segmentation results of GAS. Second row (i.e., figures (d), (e), and (f)) show segmentation results of the proposed approach without non-overlapping constraints. Third row (i.e., figures (g), (h), and (i)) show segmentation results of the proposed approach. First (i.e., figures (a), (d), and (g)), second (i.e., figures (b), (e), and (h)), and third (i.e., figures (c), (f), and (i)) columns represent segmentation results of each approach on T_1W combined FA, SWI, and T_2W, respectively. The left and right sides in each figure are two views for CN, Tha, and Pu. GPe (The light green) segmented on T_2W combined with SWI (i.e., segmented GPe in Figure 16(c)) is incorporated as contours in (d)-(i) to see overlaps between Pu and GPe. Note that overlaps between Pu and GPe in figures (g)-(i) are considerably reduced (see top right of (d)-(i)).

2.5 Discussion

From the quantitative evaluation of segmentation on different combinations of two MRI modalities, we observe that the combination of T_2W and SWI within GPe, GPi, SN, and STN region, and FA and SWI within CN, Pu, and Tha region, exhibits better segmentation results than other combinations. Note that these combinations are consistent with those utilized for each structure in manual segmentation (Lenglet et al., 2012). Furthermore, we demonstrated that global shape constraints (i.e., shape priors and non-overlapping penalty) within our proposed approach, lead to significant improvement on the segmentation quality of neighboring sub-cortical structures.

Although the proposed approach performs volumetric segmentation of complex and adjacent structures such as the basal ganglia and thalamus, showing overall accurate results, several factors can be further considered to prove its effectiveness in practical cases.

The proposed method exploits edge information from only two single-modal MR images, where each structure is fairly or even partially visible. The segmentation performance will be improved by incorporating more sufficient edge information if other single-modal images acquired at different 7 T MRI protocols are additionally available (e.g., FLASH 2-D T^*_2 weighted imaging (Kerl et al., 2012)).

However, combination of all the different image modalities does not necessarily ensure better results, since some structures might not be well identified on the specific

modal MR image. As seen in Figure 21(g)–(i), overall segmentation results of CN, Pu, and Tha are not as accurate as those obtained from FSL FIRST, even if the performance on only the low contrast T_1W data is improved by exploiting detailed edge information of SWI or FA image which provides more anatomical information than T_1W image within sub-cortical structures (Abosch et al., 2010) with shape constraints. Note that thalamus regions on the T_1W image are homogenous due to its low contrast (Abosch et al., 2010), and thus utilization of the edge information is limited within our proposed approach. In particular, those structures are more accurately segmented on the combination of FA image and SWI within our proposed model (see Figure 18(c)).

Therefore, the optimal combination for the complementary use of edge information from more single-modal MR images from different MR protocols, particularly, where target structures are fairly visible, should be considered to improve the segmentation quality in our proposed framework.

Our proposed model performed the segmentation by exploiting only 5 training shapes (from all the clinical data), whereas FSL FIRST was trained using 336 manually labeled T_1W images (Patenaude et al., 2011). This low number of training data might be critical when aiming at having segmentation models adapted to a population with specific age or disease. Particularly, we consider exploiting shape prior information of sub-cortical structures within normal controls or a specific patient group (e.g., elderly patients with advanced PD for applications to the DBS) to remove biases from each subgroup. This

work aims to demonstrate an effective way of exploiting superior contrast and SNR properties of the high-field MR data from an individual subject with additional constraints for shapes (within a specific subgroup) and non-overlapping within a simple segmentation framework, but not to analyze shape changes of the target structures among or even within the specific population. We assume that the shape variation of structures is not significant within each subgroup, and this allows the small size of training sets in our proposed framework.

Nevertheless, anatomical analysis of structures within a subgroup of specific patients or even among subgroups needs to be further investigated (Daniluk et al., 2010; Bossa et al., 2011; McKeown et al., 2008; Shen et al., 2012; den Dunnen and Staal et al., 2005). If there exists a significant variability in shape and pose among target structures even within the specific population, the large size of training sets might provide more reliable information about the structures (Daniluk et al., 2010).

Additionally, we need to analyze the effect of using or not using shape priors obtained from the same subject at the different time (e.g., the datasets 3 and 4) to validate segmentation results without biases for a specific shape. This might be important in a practical case where we should utilize shape priors from all the different subjects. As presented in Table 3, in some structures, segmentations on the other datasets yield higher DC values than those on the datasets 3 and 4. Furthermore, we did not observe significant shape variations among our datasets (Lenglet et al., 2012). From these points, we cannot

conclude that there are biases when segmentation on the dataset 3 or 4 utilizes shape information from the same subject at the different date. We aim to more accurately segment sub-cortical structures from specific subjects but not to compare segmentation results of each dataset and thus exploit shape priors available at the different date from the same subject. This might provide more reliable information for the segmentation, even if we do not observe it from our experimental results. However, we should also note that for practical applications of a segmentation framework, shape priors, particularly, in small size of training sets, need to be built from all the different subjects.

Finally, our proposed approach requires several empirically set parameters. Moreover, some of such parameters (e.g., initial surface coordinate points) mainly affect the segmentation quality. Although parameters are considerably reduced in a semiautomatic segmentation way, we should further investigate the dependency between such parameters, thereby significantly reducing the number of them.

In Chapter 3, a particular application of using 7T MR structures to guidance of targeting structures for DBS surgery is presented. Specifically, I address a shape prediction problem of brain sub-cortical structures which are not normally identifiable on standard clinical data (1.5 MRI) by learning statistical shape and pose relationships between multiple adjacent structures (from the ultrahigh-field (7T) MR imaging), which might have relatively small variations within a specific subgroup (e.g., PD patients).

3. Automatic localization of clinical DBS target structures via robust shape relationship learning from ultrahigh-field MR atlases

3.1 Introduction

3.1.1 Deep brain stimulation and the need for accurate direct targeting

Deep brain stimulation (DBS) surgery is a widely used neurosurgical intervention for the treatment of neuro-degenerative diseases such as Parkinson's disease (PD), Essential tremor, and psychiatric disorders (Dormont et al., 2010; Kim et al., 2010; Krack et al., 2010; Limousin et al., 1998; Mallet et al., 2007; Patel et al., 2008; The Deep-Brain Stimulation for Parkinson's Disease Study Group, 2001; Volkmann, 2007). In particular, it has been reported that the DBS of the subthalamic nucleus (STN) structure has important clinical efficacy for PD and potentially obsessive compulsion disorder (OCD) (Dormont et al., 2010; Limousin et al., 1998; The Deep-Brain Stimulation for Parkinson's Disease Study Group, 2001; Volkmann, 2007; Xiao et al., 2014a). Accurate positioning of the electrodes into the proper target structures is critical for a successful DBS procedure, since slight misplacement even within the target region may result both in lack of response and severe side effects (Hamid et al., 2005; Kerl et al., 2012; Mallet et al., 2007; Patel et al., 2008; Starr et al., 2002; Xiao et al., 2014a). For this reason, various targeting approaches have been investigated for the STN localization during the DBS procedure. Some of the most commonly used of those methods refer to anatomical information such as the inter-commissural distances and the ventricles, based on (histology) atlases, to localize the STN

(Dormont et al., 2010; Zonenshayn et al., 2000). However, in such indirect single-subject atlas-based targeting procedures, the variability in the position and size of the STN across individual subjects needs to be further analyzed in the context of large populations to evaluate their applicability (Daniluk et al., 2010; Kerl et al., 2012). Recent studies have started to address this issue by assessing the variability in the position and size of the STN based on the mid-commissural point across PD patients (Daniluk et al., 2010; Xiao et al., 2014a).

More recently, multiple atlases based DBS targeting approaches have been proposed (Xiao et al., 2014a; Xiao et al., 2014b; D'Albis et al., 2014). These studies provided promising results for visualization of the STN for DBS surgery on 3 Tesla (T) MR datasets. Xiao et al. (2014a) statistically analyzed morphometric variability of DBS structures obtained by a majority voting of propagated labels from multiple 3T MR atlases to the query patient 3T MR test data. D'Albis et al. (2014) provided a pipeline for DBS planning and postoperative validation, and their proposed segmentation mainly relies on the registration between atlases with labeled structures and the 3T MR test data. While encouraging initial results are obtained with these techniques, it is still not feasible to apply them in the *clinical scenario* based on the low quality 1.5T (and even 3T) MR datasets. The approach here proposed is not about more traditional registration and label propagation, but about selectively using a high-quality MR database and learned structures relationships to predict the DBS target.

In practice, to validate the location of the DBS target region, electrophysiological measurements, such as microelectrode recording (MER), that are lengthy and might result in increased risks for hemorrhage, are utilized during the surgery. These are often complemented with patient's behavioral feedback, since in the vast majority of DBS procedures the subject is awake.

More reliable targeting approaches are based on the direct visualization and localization of the STN (or DBS target in general) on the individual patient's MRI for safe and time-efficient DBS targeting (Dormont et al., 2010; Xiao et al., 2014b). With recent advances in ultra-high magnetic fields, 7T MR imaging techniques allow us to directly identify small and complex anatomical structures due to its visual benefits - the superior contrast and high resolution (Abosch et al., 2010; Cho et al., 2010; Kerl et al., 2012), and their clinical feasibility has been proven addressing a wide range of artifacts in several studies (Duchin et al., 2012; Zitella et al., 2015). Furthermore, patient-specific three dimensional (3D) structures and their connectivity within the Basal ganglia and thalamic have been modeled, exploiting the benefits of 7T MRI, especially with the combination of multi-contrast MR images such as susceptibility-weighted image (SWI) and T_2-weighted (T_2W) image (Abosch et al., 2010; Kim et al., 2014; Lenglet et al., 2012). However, such high-field MR machines are limited for clinical use due to significantly increased costs, the DBS targeting structures need to be localized on low-field clinical 1.5T or 3T MRI.

Unfortunately, such high quality visualization is not always possible with such standard clinical MRI protocols.

In addition to the general target localization, the accurate segmentation that provides spatial information such as location, dimension, and orientation of the DBS target structures in 3D is also a pre-requisite for the optimal electrode placement. This is in part due to the potential of lower therapeutically benefits and/or side-effects resulting from inadequate positioning of the DBS electrode inside the STN. Manual segmentation is both time consuming and mainly driven by anatomical subjectivity due in part to the lack of clear target visualization with clinical MRI protocols. It is challenging to even manually localize or segment the STN structure on the clinical MRI since it is a small and complex shape with relatively unclear boundaries with its adjacent structure (i.e., substantia nigra (SN)). Contrary to this, superior contrast and high resolution at 7T MR imaging enable us to directly identify and visualize the STN, including for example the border between SN and STN.

3.1.2 Automatic segmentation

Of numerous automatic segmentation techniques, statistical shape model-based segmentation such as active shape model (ASM) and active appearance model (AAM) have shown their effectiveness in various medical imaging applications (Cerrolaza et al., 2012, 2015; Cootes et al., 1995; Frangi et al., 2002; Heimann and Meinzer, 2009; Sung et al., 2007). ASM statistically models the variability of target structures across subjects and

searches for the best-fit by minimizing criteria that combine the shape model and the subject-specific information. AAM models the appearance of the whole region within the object across training data and then minimize the difference between appearances of the model and target image. In addition to the availability of the training set, the accuracy of the segmentations mainly depends on the (minimization) initialization and the quality of the actual input (i.e., subject) data (Rogers et al., 2000). Recently, morphological variations of brain structures across populations have been analyzed using such statistical shape models (Jakab et al., 2012; Shen et al., 2012). We will use extensions of these models to automatically segment the predictors in the clinical data and also to further refine the actual prediction.

3.1.3 Shape prediction

Recent studies have proposed regression-based shape prediction approaches using statistical shape models, considering correlations between different structures (Baka et al., 2011; Blanc et al., 2012; Rao et al., 2008). Sub-cortical brain structures are predicted by combining canonical correlation analysis and partial least squares regression (PLSR) in Rao et al. (2008). Several regression models for the shape prediction are compared, considering the uncertainty on landmark points (Baka et al., 2011), and incorporating relevant predictors to further improve femur and tibia predictions based on their sparse observation (Blanc et al., 2012). Most recently, regression forest models were employed to efficiently localize bounding boxes of anatomical structures in CT (Criminisi et al., 2013).

Mishina (2010), instead of using the regression approach, built a joint input-output distribution model. Furthermore, estimation of confidence regions for the predicted target shape has been investigated (Blanc et al., 2009; Blanc and Szekely, 2012; Mishina, 2010). These shape prediction methods enable us to estimate the target structures even on data with limited information within the regions of interest (Blanc et al., 2009). We design new prediction strategies based on the combination of the clinical data with the 7T database.

3.1.4 Our contribution

The aim of this work is to automatically localize and visualize clinical DBS target structures such as the STN on the patient-specific clinical (1.5T) MR data, thereby opening the door for direct targeting. To predict the STN, which is not identifiable on such standard clinical data, we explicitly exploit learned spatial relationship with its neighboring structures. Since it is challenging to even manually segment the STN on the clinical MR datasets, such MRI does not allow us to build high quality training data for a statistical shape relationship-learning model. Also, the uncertainty of the predicted output might be attributed to the large variability of learned information from various training subsets. The influence of such training subsets in the prediction accuracy needs to be considered in order to reduce biases from training datasets.

To address these issues, this work introduces a robust prediction model for reliably detecting STN-DBS targets on clinical low-field MRI, automatically learning shape dependencies between the STN and its predictors from the most influential high-

field MR atlases available in a large high-quality dataset. A key contribution is to first utilize clinical 1.5T MRI and its corresponding 7T MRI pair from the same patient to construct high-quality training data. High quality shape information on the 7T MR training data is transferred onto a patient-specific 1.5T MRI. A bagging process is applied in regression models to reduce the variability of learned information, thereby achieving confidence regions. Additionally, the contribution of multiple training subsets in the prediction is estimated, learning the mapping between pose related features for each training subset and the prediction accuracy. Finally, given manually or automatically segmented predictors from the patient's clinical 1.5T MR data, we obtain a final probability map as a weighted ensemble of predicted STN volumes from the learned 7T MR shape relationships.

In Section 3.2 we describe the pre-processing for building high quality training data and segmenting predictors, followed by mathematical descriptions of the proposed prediction framework. Prediction results, evaluation, and their analysis on the clinical dataset from PD patients are presented in Section 3.3. Finally, we discuss the prediction results in Section 3.4 and conclude the work in Chapter 4.

A part of this work will be submitted to NeuroImage (Kim et al., 2015d). Preliminary results were also presented in Kim et al. (2015a, 2015b, and 2015c).

3.2 Methods

3.2.1 Overview

We address the localization problem of DBS target structures on standard clinical 1.5T MRI, learning dependencies between the target structure and its predictors from most influential high-field MR atlases in a large high-quality database. High quality shape information on high-field 7T MR training data is transferred for DBS targeting onto the clinical low-field MRI from a query patient. DBS target structure and its corresponding predictors are represented as the coordinates of surface points, in correspondence, across the training sets, and parameterized as poses and shape principal components. Bagged regression methods then determines the relationships between the target and its predictors in the parameterized space, reducing the prediction uncertainty. Additionally, the contribution of each training subset to the prediction is estimated via a machine learning approach to obtain higher confidence regions. Given predictors as identified on standard clinical MR data from a query patient, the 3D DBS target structure is obtained as a probability map using the learned relationships with estimated influence scores. Next sections describe each component of the proposed prediction framework in detail, followed by its application to the guidance of STN-DBS targeting.

3.2.2 Database pre-processing

Ultrahigh-field 7T MRI and its corresponding clinical 1.5T MRI pair from 46 patients were obtained at the Center for Magnetic Resonance Research, University of

Minnesota, under approval of the Institutional Review Board at the University of Minnesota. The non-uniformity on 7T T_1W MR images was corrected using FSL FAST (Woolrich et al., 2009). Brain extraction was performed on T_1W images from 7T and 1.5T using FSL's Brain Extraction Tool (Smith, 2002). The resulting 7T T_1W MR images were linearly registered onto T_1W 1.5T image pairs from the same patients using the FSL FLIRT (FMRIB's Linear Image Registration Tool, Greve and Fischl, 2009; Jenkinson and Smith, 2001; Jenkinson et al., 2002). For each 7T MR Dataset, T_2W and SWI coronal images were utilized to segment the DBS target structure and its predictors within the Basal ganglia and thalamus region (Lenglet et al., 2012; Kim et al., 2014). 1.5T T_2W MR images were utilized to segment predictors of the target structure from query patients. The acquisition protocol for 7T and 1.5T MRIs, respectively, used in this work is presented in Appendix A.

3.2.3 Building high quality patient-specific training data

Our work aims at automatically localizing DBS target structures which are not normally identifiable on standard clinical 1.5T MRI. For that purpose, we learn shape relationships between the target structure and its predictors (which can be identified in the clinical data) using regression methods. However, it is challenging to even manually segment DBS target structures on the clinical 1.5T MRI (in contrast with high-field MRIs) in order to construct high quality training shapes for such learning models. In order to address this problem, we exploit our database of pairs of 7T and 1.5T MRIs from the same

patient, learning high quality shape relationships from the high-field MRI training sets applicable after that to the localization of DBS target structures on the clinical low-field MRI (when of course only the low-field/quality clinical MRI is available).

DBS target structure and its predictors within the Basal ganglia and thalamus are manually or automatically segmented from 7T MR training datasets according to a subject-specific analysis pipeline (Lenglet et al., 2012; Kim et al., 2014). We will discuss in detail how to define predictors for DBS target structures in sections 3.2.4 and 3.2.7. For each query patient, similar atlases (out of 45 patients) in our database are chosen based on the 1.5T T_2W images mutual information (MI) within the ROI (Aljabar et al., 2009).

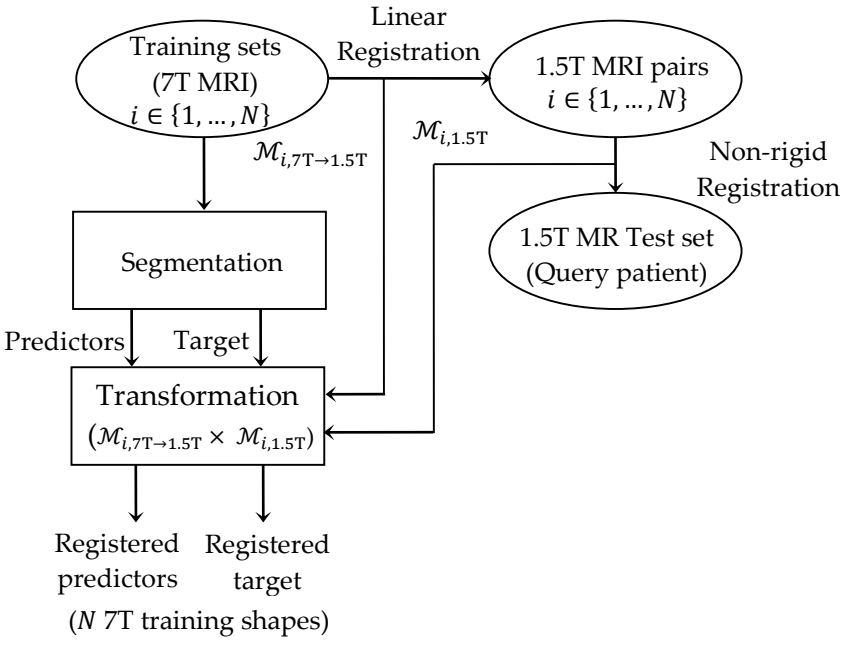

Figure 22: Registration process between each 7T MR training subset (from similar patients) and 1.5T MR test data (from a query patient).

Segmented 7T MR structures from similar atlases were first registered onto 1.5T T_2W data with a co-registration protocol between 7T and its 1.5T T_1W MRI pair, using the FSL FLIRT and following Duchin et al. (2012).

Registered 7T MR structures (onto 1.5T MR pairs) from similar atlases need to be normalized into the same coordinate space as the 1.5T MR test data of the query patients due to pose variability, including different locations and orientations of patients during the scans (Bossa et al., 2011) and the resolution disparity between different MR modalities or magnetic fields. This also allows correctly extracting shape and pose parameters of predictors for the 1.5T MR test data with respect to 7T MR training shapes on the common coordinate space. For this purpose, we non-linearly register 1.5T T_2W MR training data and corresponding registered 7T MR structures onto 1.5T T_2W MR test data using the Advanced Normalization Tools (ANTS, Avants and Gee, 2004; Avants et al., 2011a, 2011b). Figure 22 shows the overall registration processes between 7T MR training data and 1.5T MR test data of a query patient.

3.2.4 Automatic segmentation of patient-specific predictors

Prediction accuracy is influenced by the degree of correlation between the DBS target and its predictor structures. Recent studies have reported that pairs of adjacent brain structures are highly correlated (Rao et al., 2006, 2008). Therefore, predictors for the DBS target in sub-cortical structures need to be chosen by considering the spatial adjacency with the target structure. Also, brain sub-cortical structures used as predictors

should be easily detectable on the clinical low-field MR data. However, it is still a challenging task to accurately and automatically segment the most useful predictors on standard clinical MRI due to their low contrast around the boundary. In this section, we discuss how to obtain such predictors on the patient-specific clinical low-field MRI in a fully automatic way.

3.2.4.1 A unified model for learning shape, textures, and local intensity

Active shape model (ASM, Cootes et al., 1995), active appearance model (AAM, Cootes et al., 2001), and their numerous variants have been successfully applied to solve many image segmentation challenges, particularly for facial expression recognition and medical image analysis. However, these two independent models have drawbacks such as high sensitivity to the initialization and noisy background, respectively. Recently, and as adopted here, a combined model of ASM and AAM was proposed to address such problems and produce more accurate results in a fully automatic fashion. This combined approach simultaneously models a target shape, textures within a target region, and intensity profiles around its boundary; see Sung et al. (2007) for details.

3.2.4.2 High-field MR shape and appearance learning based deformable segmentation

As described in Section 3.2.3, we are given 7T MR training images and corresponding segmented structures for DBS target and its predictors, registered onto the 1.5T T_2W MRI from a query patient. We need to automatically find predictors to predict the DBS target structure on the 1.5T T_2W MRI using information within the unified model

mentioned above (Sung et al., 2007). Figure 23 represents the proposed automatic segmentation process. We learn high quality shape information, appearances within the structure, and local intensity profile around its boundary from the registered 7T MR training images and corresponding segmented predictors. Given the 1.5T T_2W MRI for a query patient, we obtain the fitting result for predictors with optimal parameters, iteratively minimizing the AAM and ASM error terms using the learned information as the initialization.

The normalized appearances within the boundary of predictors between 7T MR training images and its 1.5T MR pairs from the same patients are similar (i.e., they are fairly visible on the 1.5T MRI), although 7T MRIs provide more details due in part to its superior contrasts (Duchin et al., 2012). Furthermore, an initial shape model is obtained

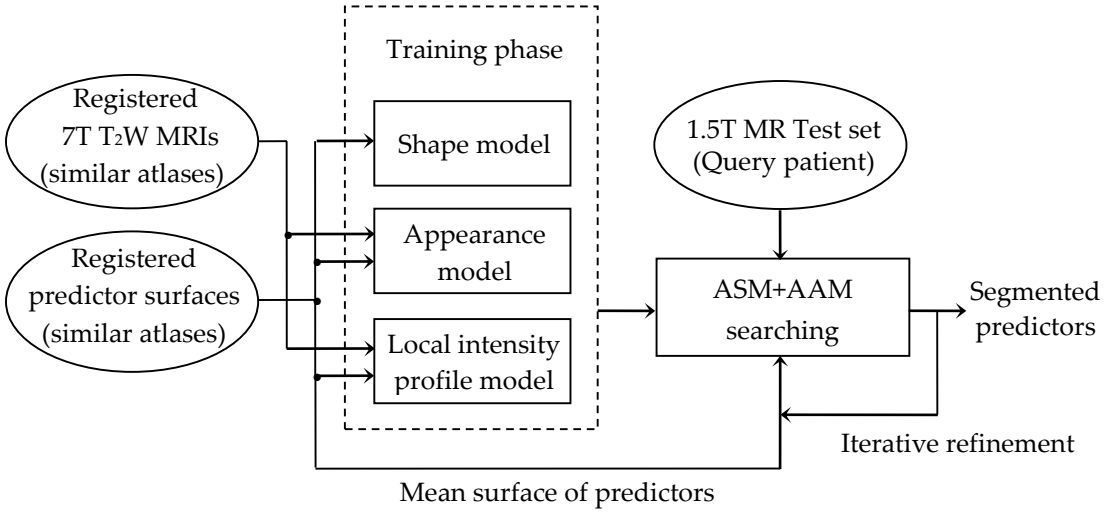

Figure 23: Automatic segmentation process of predictors on standard clinical MR data from a query patient.

from nonlinearly registered similar atlases to a query patient, thus providing a good enough initialization for deformable segmentation. Note that it is still hard to directly segment the DBS target with the model or via multiple atlases-based labeling fusion since appearances and boundaries of the DBS target on the 1.5T MRI of a query patient are not differentiable from those of its adjacent predictors. We will exemplify this in Section 3.2.7 and validate with experimental results.

3.2.5 Ensemble shape prediction

Our proposed approach provides an ensemble of predicted binary volumes for the DBS target structure, exploiting learned shape relationships between the target structure and its predictors from random subsets of 7T MR training sets. An overall scheme of the prediction framework is presented in Figure 24 (Kim et al., 2015a; Kim et al., 2015b). We describe additional details next.

3.2.5.1 Pose and shape parameterization of anatomical structures

Statistical shape models enable us to exploit prior information about shape variations, learned from a set of training shapes. Common statistical shape models are based on a point distribution model (PDM), which first represents the shapes by a set of landmark points (i.e., vertices in a mesh) distributed along its surface, and then models the shape variation (Cootes et al., 1992, 1995). Particularly, the correspondence among landmark points of training shapes is required in order to capture shape variations and build a regression model for shape prediction.

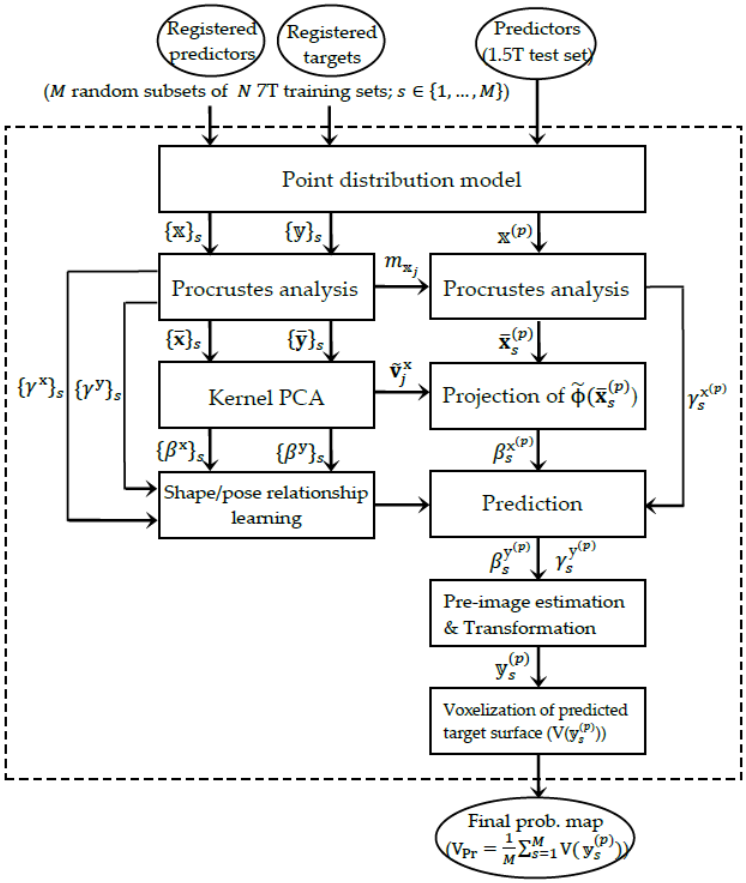

Figure 24: Overall scheme of the ensemble prediction framework (Kim et al., 2015a, 2015b).

A minimum description length (MDL) based approach has been recognized as an effective shape correspondence method (Styner et al., 2003). To obtain such landmarks in correspondence across a set of training shapes, we adopt a recent MDL-based method that first generates landmarks by conformally mapping a spherical mesh parameterization to the training shapes, and then optimizes the correspondence via gradient descent (Heimann et al., 2005, 2006).

In our prediction framework, three dimensional shapes of predictors and the DBS target structure, for M random subsets of N training sets, are represented as the coordinate of surface points, $\mathbb{x}_{i,s} \in \mathbb{R}^{n_\mathrm{x} \times 3}$ and $\mathbb{y}_{i,s} \in \mathbb{R}^{n_\mathrm{y} \times 3}$, respectively, for $i \in \{1, \dots, N\}$ and $s \in \{1, \dots, M\}$, where n_x and n_y is the number of surface points for predictors and target structures respectively. Column vectors $\mathbf{x}_{i,s} \in \mathbb{R}^{3n_\mathrm{x}}$ and $\mathbf{y}_{i,s} \in \mathbb{R}^{3n_\mathrm{y}}$ are obtained by concatenating all the coordinates:

$$\mathbf{x}_{i,s} = (x_{1,1}, x_{1,2}, x_{1,3}, \dots, x_{n_\mathrm{x},1}, x_{n_\mathrm{x},2}, x_{n_\mathrm{x},3})^\mathrm{T},\ \mathbf{y}_{i,s} = (y_{1,1}, y_{1,2}, y_{1,3}, \dots, y_{n_\mathrm{y},1}, y_{n_\mathrm{y},2}, y_{n_\mathrm{y},3})^\mathrm{T} \quad (3.1)$$

Additionally, we denote surfaces of predictors and the predicted target structure on the test data as vectors $\mathbf{x}^{(p)} \in \mathbb{R}^{3n_\mathrm{x}}$ and $\mathbf{y}^{(p)} \in \mathbb{R}^{3n_\mathrm{y}}$, respectively. We aim at estimating a set of surface points of the target structure $\mathbf{y}^{(p)}$ from the surface of its predictors $\mathbf{x}^{(p)}$ on the test data using the spatial relationship between the target structure $\{\mathbf{y}_i\}_s \in \mathbb{R}^{3n_\mathrm{y} \times N}$ and its predictors $\{\mathbf{x}_i\}_s \in \mathbb{R}^{3n_\mathrm{x} \times N}$ for each random subset of training sets.

Shape parameters and poses of the target structure and its predictors across the training set and predictors on the test data are obtained from their aligned surface landmark points, in order to extract their spatial relationship in a lower dimensional space. More specifically, the generalized Procrustes analysis (Cootes et al., 1992; Gower, 1975) is performed on each predictor $\mathbb{x}_{i,s}$ and the target structure $\mathbb{y}_{i,s}$ with respect to their mean shapes $m_{\mathbb{x}_s}$ and $m_{\mathbb{y}_s}$, respectively, across training sets, removing poses from shapes. The

alignment process yields pose parameter vectors $\{\gamma_i^{\mathrm{x}}\}_s \in \mathbb{R}^{10\times N}$ and $\{\gamma_i^{\mathrm{y}}\}_s \in \mathbb{R}^{10\times N}$ including translations $t \in \mathbb{R}^3$, scaling factors $s \in \mathbb{R}^3$, and entries of a 3D rotation matrix $r \in \mathbb{R}^4$ for each random subset of training sets. Also, a pose parameter vector ${\gamma_s}^{\mathrm{x}^{(p)}} \in \mathbb{R}^{10}$ for predictors $\mathbb{x}^{(p)}$ on the test data is calculated with respect to $m_{\mathbb{x}_s}$.

Aligned column vectors $\bar{\mathbf{x}}_{i,s}$ and $\bar{\mathbf{y}}_{i,s}$ (into $m_{\mathbb{x}_s}$ and $m_{\mathbb{y}_s}$) in each training subset are then modeled in lower dimensional space using shape parameterization methods such as principal components analysis (PCA). In this particular context, we employ a kernel PCA (KPCA), a non-linear extension of PCA, in order to increase the predictive potential by considering non-linear relationships between training shapes (Guo, 2010).

In KPCA, the input space (e.g., $\bar{\mathbf{x}}_i \in \mathbb{R}^{3n_{\mathrm{x}}}$, for simplicity, we remove s for each training subset) is non-linearly mapped into a feature space $\mathcal{F}$ by

$$\phi : \mathbb{R}^{3n_{\mathrm{x}}} \rightarrow \mathcal{F}, \qquad \bar{\mathbf{x}}_i \rightarrow \phi(\bar{\mathbf{x}}_i). \tag{3.2}$$

The covariance matrix $\mathbf{C}$ in the feature space $\mathcal{F}$ is defined as

$$\mathbf{C} = \frac{1}{N}\sum_{i=1}^{N} \tilde{\phi}(\bar{\mathbf{x}}_i)\tilde{\phi}(\bar{\mathbf{x}}_i)^T, \tag{3.3}$$

where $\tilde{\phi}(\bar{\mathbf{x}}_i)$ is the centered map given by $\phi(\bar{\mathbf{x}}_i) - \bar{\phi}_{\mathrm{x}}$, denoting the mean of the ϕ map by $\bar{\phi}_{\mathrm{x}} = \sum_{i=1}^{N} \phi(\bar{\mathbf{x}}_i)$. Linear PCA in the feature space $\mathcal{F}$ involves solving the eigenvalue

problem $\mathbf{C}\mathbf{v}^{\mathrm{x}} = \lambda\mathbf{v}^{\mathrm{x}}$, where $\mathbf{v}^{\mathrm{x}} \in \mathcal{F}\backslash\{0\}$ are eigenvectors and λ are non-zero eigenvalues of the covariance matrix $\mathbf{C}$. Substituting the covariance matrix $\mathbf{C}$ into the eigenvalue problem, we obtain

$$\mathbf{C}\mathbf{v}^{\mathrm{x}} = \frac{1}{N}\sum_{i=1}^{N}(\widetilde{\phi}(\bar{\mathbf{x}}_i) \cdot \mathbf{v}^{\mathrm{x}})\widetilde{\phi}(\bar{\mathbf{x}}_i). \tag{3.4}$$

As this implies that all the eigenvectors $\mathbf{v}^{\mathrm{x}}$ lie in the span of $\widetilde{\phi}(\bar{\mathbf{x}}_1),\ldots, \widetilde{\phi}(\bar{\mathbf{x}}_N)$ (Schölkopf et al., 1998, 1999), $\mathbf{v}^{\mathrm{x}}$ can be represented as

$$\mathbf{v}^{\mathrm{x}} = \sum_{i=1}^{N} a_i\, \widetilde{\phi}(\bar{\mathbf{x}}_i), \tag{3.5}$$

where a_i are coefficients for $i \in \{1, \ldots, N\}$. The equivalent eigenvalue problem is then considered as

$$(\widetilde{\phi}(\bar{\mathbf{x}}_i) \cdot \mathbf{C}\mathbf{v}^{\mathrm{x}}) = \lambda(\widetilde{\phi}(\bar{\mathbf{x}}_i) \cdot \mathbf{v}^{\mathrm{x}}). \tag{3.6}$$

Substituting (3.4) and (3.5) into (3.6) and introducing a centered kernel matrix $\widetilde{\mathbf{K}} \in \mathbb{R}^{N\times N}$ with entries $\widetilde{\boldsymbol{\kappa}}_{ij} = \tilde{k}(\bar{\mathbf{x}}_i, \bar{\mathbf{x}}_j)$, where $\tilde{k}(\bar{\mathbf{x}}_i, \bar{\mathbf{x}}_j) = (\widetilde{\phi}(\bar{\mathbf{x}}_i) \cdot \widetilde{\phi}(\bar{\mathbf{x}}_j))$ for $i, j \in \{1, \ldots, N\}$ (Mika et al., 1999; Schölkopf et al., 1998, 1999), we obtain $\widetilde{\mathbf{K}}^2\mathbf{u} = N\lambda\widetilde{\mathbf{K}}\mathbf{u}$, arriving at its

equivalent eigenvalue problem in the matrix form with $\tilde{\lambda} = N\lambda$ (Schölkopf et al., 1998, 1999),

$$\widetilde{\mathbf{K}}\mathbf{U} = \mathbf{\Lambda}\mathbf{U}, \tag{3.7}$$

where $\mathbf{U} \in \mathbb{R}^{N\times N}$ is the unitary matrix whose column vectors $\mathbf{u}_i = [a_{i,1}, \dots, a_{i,N}]^T$ represent eigenvectors and $\mathbf{\Lambda} \in \mathbb{R}^{N\times N}$ is the diagonal matrix of eigenvalues $\tilde{\lambda}_i$ for $i \in \{1, \dots, N\}$. Note that $\widetilde{\mathbf{K}}$ is calculated by $\mathbf{HKH}$, where $\mathbf{H} \in \mathbb{R}^{N\times N}$ is the matrix given by $\mathbf{I} - \frac{1}{N}\mathbf{1}\mathbf{1}^T$ with the identity matrix $\mathbf{I} \in \mathbb{R}^{N\times N}$ and the column vector $1 \in \mathbb{R}^{N\times 1}$ with all 1's entries, centering $\mathbf{K} \in \mathbb{R}^{N\times N}$ with entries $\boldsymbol{\kappa}_i = k(\bar{\mathbf{x}}_i, \bar{\mathbf{x}}_j)$, where $k(\bar{\mathbf{x}}_i, \bar{\mathbf{x}}_j) = (\phi(\bar{\mathbf{x}}_i) \cdot \phi(\bar{\mathbf{x}}_j))$ for $i, j \in \{1, \dots, N\}$ (Kwok and Tsang, 2004; Ma and Zabaras, 2011). Here, we choose the commonly used Gaussian kernel $k(\bar{\mathbf{x}}_i, \bar{\mathbf{x}}_j) = exp(-\|\bar{\mathbf{x}}_i - \bar{\mathbf{x}}_j\|^2/2\sigma^2)$, with a parameter σ controlling the width of the kernel.

The qth eigenvector of the covariance matrix $\mathbf{C}$ in the feature space $\mathcal{F}$ from (3.5) solving the kernel eigenvalue problem of (3.7) can be obtained by

$$\mathbf{v}_q^{\mathrm{x}} = \sum_{i=1}^{N} a_{q,i}\, \widetilde{\phi}(\bar{\mathbf{x}}_i), \tag{3.8}$$

where $q \in \{1, \dots, N\}$. Normalizing $\mathbf{v}_q^{\mathrm{x}}$ (i.e., $\mathbf{v}_q^{\mathrm{x}\,T}\mathbf{v}_q^{\mathrm{x}}$=1), we obtain the q th orthonormal eigenvector $\tilde{\mathbf{v}}_q^{\mathrm{x}}$ of the covariance matrix $\mathbf{C}$ in the feature space as

$$\tilde{\mathbf{v}}_q^{\mathrm{x}} = \sum_{i=1}^{N} \tilde{a}_{q,i}\, \widetilde{\phi}(\bar{\mathbf{x}}_i), \tag{3.9}$$

where $\tilde{a}_{q,i} = a_{q,i} / \sqrt{\tilde{\lambda}_q}$. The resulting qth kernel principal components $z_{q,j}^{\mathrm{x}}$ can then be calculated by projecting the $\widetilde{\phi}$ map of each predictor $\bar{\mathbf{x}}_j$ in the training set onto $\tilde{\mathbf{v}}_q^{\mathrm{x}}$ as

$$z_{q,j}^{\mathrm{x}} = (\tilde{\mathbf{v}}_q^{\mathrm{x}} \cdot \widetilde{\phi}(\bar{\mathbf{x}}_j)) = \sum_{i=1}^{N} \tilde{a}_{q,i}\, (\widetilde{\phi}(\bar{\mathbf{x}}_i) \cdot \widetilde{\phi}(\bar{\mathbf{x}}_j)) = \sum_{i=1}^{N} \tilde{a}_{q,i}\, \tilde{k}\left(\bar{\mathbf{x}}_i, \bar{\mathbf{x}}_j\right), \tag{3.10}$$

where the centered kernel vector $\tilde{k}\left(\bar{\mathbf{x}}_i, \bar{\mathbf{x}}_j\right)$ can be calculated from $k\left(\bar{\mathbf{x}}_i, \bar{\mathbf{x}}_j\right)$ (Kwok and Tsang, 2004).

When the dimension of the feature space $\mathcal{F}$ is infinite, the eigenvalue problem on the covariance matrix $\mathbf{C}$ is not solvable (Schölkopf et al., 1998, 1999). Kernel methods enable us to obtain the principal components in feature space without explicitly computing the ϕ mapping (the "kernel trick").

In our prediction framework (Figure 24), kernel principal components for eigenvectors $\tilde{\mathbf{v}}^{\mathrm{x}}$ ordered by the first r largest eigenvalues $\tilde{\lambda}$ in the feature space (i.e., $r \ll N$) are stored as shape parameter vectors $\beta_{i,s}^{\mathrm{x}}$ for each predictor $\bar{\mathbf{x}}_{i,s}$ for each training subset s:

$$\beta_{i,s}^{\mathrm{x}} = [z_{1,i}^{\mathrm{x}}, \ldots, z_{r,i}^{\mathrm{x}}]^T. \tag{3.11}$$

Similarly, shape parameter vectors $\beta_{i,s}^{\mathrm{y}}$ for each target structure $\bar{\mathbf{y}}_{i,s}$ in each training subset are obtained by projecting $\widetilde{\phi}(\bar{\mathbf{y}}_i)$ onto eigenvectors $\tilde{\mathbf{v}}^{\mathrm{y}}$ ordered by the first r largest eigenvalues of the covariance matrix of $\widetilde{\phi}(\bar{\mathbf{y}}_i)$ in the feature space,

$$\beta_{i,s}^{\mathrm{y}} = [z_{1,i}^{\mathrm{y}}, \dots, z_{r,i}^{\mathrm{y}}]^T, \tag{3.12}$$

where $z_{r,i}^{\mathrm{y}} = (\tilde{\mathbf{v}}_r^{\mathrm{y}} \cdot \widetilde{\phi}(\bar{\mathbf{y}}_i))$. Additionally, shape parameter vectors ${\beta_s}^{\mathrm{x}^{(p)}}$ for a predictor on the test data can be calculated by projecting the $\tilde{\phi}$ map of the predictor vector $\bar{\mathbf{x}}^{(p)}$ onto eigenvectors $\tilde{\mathbf{v}}^{\mathrm{x}}$ corresponding to the first r largest eigenvalues of the covariance matrix $\mathbf{C}$ of $\widetilde{\phi}(\bar{\mathbf{x}}_i)$,

$${\beta_s}^{\mathrm{x}^{(p)}} = [z_1^{\mathrm{x}^{(p)}}, \dots, z_r^{\mathrm{x}^{(p)}}]^T, \tag{3.13}$$

where $z_r^{\mathrm{x}^{(p)}} = (\tilde{\mathbf{v}}_r^{\mathrm{x}} \cdot \widetilde{\phi}(\bar{\mathbf{x}}^{(p)}))$.

Now let us assume that shape parameters of the target structure ${\beta_s}^{\mathrm{y}^{(p)}}$ are predicted from ${\beta_s}^{\mathrm{x}^{(p)}}$ on the test data using the relationship between $\{\beta_i^{\mathrm{x}}\}_s$ and $\{\beta_i^{\mathrm{y}}\}_s$ across the training set in our prediction framework (see also Figure 24), and similarly pose parameters of the ${\gamma_s}^{\mathrm{y}^{(p)}}$ are predicted from ${\gamma_s}^{\mathrm{x}^{(p)}}$ on the test data using the relationship

between $\{\gamma_i^{\mathrm{x}}\}_s$ and $\{\gamma_i^{\mathrm{y}}\}_s$ for each training subset. We need to reconstruct the landmark points of the target $\bar{\mathbf{y}}_s{}^{(p)}$ in the input space from the predicted $\beta_s{}^{\mathrm{y}(p)}$ in the feature space.

Finally, we obtain this way the complete shape of the target $\mathbf{y}_s{}^{(p)}$ from $\bar{\mathbf{y}}_s{}^{(p)}$ with predicted pose parameters $\gamma_s{}^{\mathrm{y}(p)}$. Note that the projection of $\widetilde{\phi}(\bar{\mathbf{y}}_s{}^{(p)})$ onto the subspace spanned by the eigenvectors $\tilde{\mathbf{v}}^{\mathrm{y}}$ corresponding to the first r largest eigenvalues of the covariance matrix of $\widetilde{\phi}(\bar{\mathbf{y}}_i)$ in the feature space is given by

$$\mathcal{P}\widetilde{\phi}(\bar{\mathbf{y}}_s{}^{(p)}) = \sum_{q=1}^{r} z_q^{\mathrm{y}(p)}\, \tilde{\mathbf{v}}_q^{\mathrm{y}}, \tag{3.14}$$

where $z^{\mathrm{y}(p)}$ are r predicted principal components of $\beta_s{}^{\mathrm{y}(p)}$. Also, we obtain $\mathcal{P}\phi(\bar{\mathbf{y}}_s{}^{(p)})$ with $\bar{\phi}_{\mathrm{y}} = \sum_{i=1}^{N} \phi(\bar{\mathbf{y}}_{i,s})$ as

$$\mathcal{P}\phi(\bar{\mathbf{y}}_s{}^{(p)}) = \sum_{q=1}^{r} z_q^{\mathrm{y}(p)}\, \tilde{\mathbf{v}}_q^{\mathrm{y}} + \bar{\phi}_{\mathrm{y}}. \tag{3.15}$$

The reconstruction problem of $\bar{\mathbf{y}}_s{}^{(p)}$ (i.e., pre-image estimation $\bar{\mathbf{y}}_{\mathrm{est}}^{(p)}$ in the original space, where $\phi(\bar{\mathbf{y}}_{\mathrm{est}}^{(p)}) \cong \mathcal{P}\phi(\bar{\mathbf{y}}_s{}^{(p)})$) is ill-posed since the ϕ mapping is not invertible for non-linear kernel functions (Rasmussen et al., 2012; Schölkopf et al., 1998, 1999). Several studies have been proposed to address this non-linear optimization problem in KPCA (Kwok and Tsang, 2004; Ma and Zabaras, 2011; Mika et al., 1999; Rathi et al., 2006). Mika et al. (1999) proposed an iterative approach which minimizes the squared distance

between $\phi(\bar{\mathbf{y}}_{\text{est}}^{(p)})$ and $\mathcal{P}\phi(\bar{\mathbf{y}}_s{}^{(p)})$, but suffers from local minimum and initialization problems. Kwok and Tsang (2004) estimated the pre-image from a relationship between the feature space distance $\tilde{d}(\mathcal{P}\phi(\bar{\mathbf{y}}^{(p)}), \phi(\bar{\mathbf{y}}_{i,s}))$ and the corresponding distance $d(\bar{\mathbf{y}}_{\text{est}}^{(p)}, \bar{\mathbf{y}}_{i,s})$in input space, based on multidimensional scaling. However, this requires highly computational costs. More recently, a reconstruction approach which only utilizes the feature space distance without the iteration component was proposed by Rathi el al. (2006). Also, Ma and Zabaras (2011) proposed a local linear interpolation based approach which only uses the input space distances between the estimated pre-image and nearest neighbors for stochastic input modeling. We here employ the more reliable and faster reconstruction approach presented by Rathi el al. (2006) to estimate $\bar{\mathbf{y}}_s{}^{(p)}$ in our prediction problem.

In this section, we showed how to extract shape parameters (i.e., $\{\beta_i^{\text{y}}\}_s$ and $\{\beta_i^{\text{x}}\}_s$) and poses (i.e., $\{\gamma_i^{\text{y}}\}_s$ and $\{\gamma_i^{\text{x}}\}_s$) for the target structure and its predictors for each training subset using statistical analysis to capture their variation in the low dimensional space. We next focus on the prediction problem for the shape and pose of the target from those of its predictors on the test data. This is done by investigating the relationship between shape parameters and poses, respectively, across random subsets of the training set, using the regression model described in the next section.

3.2.5.2 Bagging PLSR based learning

This section addresses the linear regression problem of finding the dependency between the shape parameters and poses of the DBS target structure and its predictors in the training set. We first exploit the popular PLSR technique (Abdi, 2010; Krishnan et al., 2011; Rao et al., 2008; Wold, 1982; Wold et al., 2001). PLSR extends multi-linear regression and finds principal factors (i.e., latent vectors) within a set of predictors **X** to predict a set of response vectors **Y** so that the covariance between them is maximal. We apply a bagging procedure (Breiman, 1996) in the model to learn the information, reducing the variability and providing confident regions for the problem.

In our prediction problem, for each training subset, **X** contains a set of centered shape parameters $\{\tilde{\beta}_i^{\mathrm{x}}\}^T$ or poses $\{\tilde{\gamma}_i^{\mathrm{x}}\}^T$ for predictors and **Y** contains a set of centered shape parameters $\{\tilde{\beta}_i^{\mathrm{y}}\}^T$ or poses $\{\tilde{\gamma}_i^{\mathrm{y}}\}^T$ for the target (later to be STNs) in the training set, where $\tilde{\beta}_i = \beta_i - \sum_{i=1}^{N} \beta_i$ and $\tilde{\gamma}_i = \gamma_i - \sum_{i=1}^{N} \gamma_i$ are obtained by centering the shape parameters β_i and poses γ_i. When predictors consist of multiple structures, we extract the pose and shape parameters for each and concatenate them. For example, shape and pose parameter vectors for the left and right side of a predictor on the training sets are concatenated as $\tilde{\beta}_i^{\mathrm{x}} = (\tilde{\beta}_{i,\mathrm{left}}^{\mathrm{x}} ; \tilde{\beta}_{i,\mathrm{right}}^{\mathrm{x}})$ and $\tilde{\gamma}_i^{\mathrm{x}} = (\tilde{\gamma}_{i,\mathrm{left}}^{\mathrm{x}} ; \tilde{\gamma}_{i,\mathrm{right}}^{\mathrm{x}})$, and shape and pose parameter vectors for left and right side of a predictor on the test data are also concatenated as $\beta^{\mathrm{x}^{(p)}} = (\beta_{\mathrm{left}}^{\mathrm{x}^{(p)}} ; \beta_{\mathrm{right}}^{\mathrm{x}^{(p)}})$ and $\gamma^{\mathrm{x}^{(p)}} = (\gamma_{\mathrm{left}}^{\mathrm{x}^{(p)}} ; \gamma_{\mathrm{right}}^{\mathrm{x}^{(p)}})$.

The PLSR decomposes **X** and **Y** by finding latent matrices **T** and **F** (Abdi, 2010; Krishnan et al., 2011; Wold, 1982; Wold et al., 2001),

$$\mathbf{X} = \mathbf{T}\mathbf{P}^T, \ \mathbf{Y} = \mathbf{F}\mathbf{G}^T \ \text{ with } \ \mathbf{F} = \mathbf{T}\mathbf{B} + \boldsymbol{\varepsilon}, \tag{3.16}$$

where **P** is a loading matrix of **X**, **G** is a weight matrix of **Y**, **B** is a diagonal matrix of regression weights, and **ε** is the regression error. The latent vectors **t** and **f** of latent matrices **T** and **F**, respectively, are obtained by finding two weight vectors **w** and **g** such that linear combinations of columns of **X** and **Y** have maximum covariance, meaning that $\mathbf{t}^T\mathbf{f}$ is maximal:

$$\mathbf{t} = \mathbf{X}\mathbf{w}, \ \ \mathbf{f} = \mathbf{Y}\mathbf{g} \ \text{ with } \mathbf{w}^T\mathbf{w} = 1, \mathbf{t}^T\mathbf{t} = 1. \tag{3.17}$$

Specifically, **w** and **g** are iteratively updated and then the obtained latent vectors **t** and **f** are subtracted from **X** and **Y**, respectively, by the nonlinear iterative partial least squares approach (Abdi, 2010; Rao et al., 2008). The iteration continues until **X** become a null matrix. Finally, the response vectors **Y** are predicted as

$$\mathbf{Y} \cong \mathbf{T}\mathbf{B}\mathbf{G}^T = \mathbf{X}\mathbf{B}_{PLS}, \tag{3.18}$$

where $\mathbf{B}_{PLS} = \mathbf{P}^{T+}\mathbf{B}\mathbf{G}^{T}$, with $\mathbf{P}^{T+}$ the Moore-Penrose pseudo inverse of $\mathbf{P}^{T}$ (Abdi, 2010; Krishnan et al., 2011).

Let $\mathbf{B}_{PLS}^{\beta}$ and $\mathbf{B}_{PLS}^{\gamma}$ be regression coefficients for shape parameters and poses, respectively, between the target and its predictors in each training subset, obtained by performing the PLSR in our prediction problem. Given shape parameters ${\beta_s}^{\mathrm{x}^{(p)}}$ and poses ${\gamma_s}^{\mathrm{x}^{(p)}}$ for a predictor for each training subset on the test data, shape parameters ${\beta_s}^{\mathrm{y}^{(p)}}$ and poses ${\gamma_s}^{\mathrm{y}^{(p)}}$ for the target are then predicted as

$$ {\beta_s}^{\mathrm{y}^{(p)}} = {\beta_s}^{\mathrm{x}^{(p)}{}^{T}}\mathbf{B}_{PLS}^{\beta}, \quad {\gamma_s}^{\mathrm{y}^{(p)}} = {\gamma_s}^{\mathrm{x}^{(p)}{}^{T}}\mathbf{B}_{PLS}^{\gamma}. \tag{3.19} $$

3.2.5.3 Regression forests based learning

This section addresses the regression problem for learning non-linear mapping (for shape and pose parameters) between a target structure and its predictors using a random forest model (Kim et al., 2015b). Regression forests (RF) (Breiman, 2001; Criminisi et al., 2013) use an ensemble of regression trees, learned on random subsets of training data, to estimate output parameters with high confidence. In our prediction framework, an ensemble of predictions is obtained by using the learned regression trees on training subsets. Each tree learns how to optimally split training sets maximizing the information gain $\mathrm{I_k}$ on each node k,

$$\xi_k^* = \arg\max_{\xi_k} I_k, \tag{3.20}$$

where $I_k = H(s) - \sum_{u=\{L,R\}} p_u H(s_u)$ and ξ^* is an optimal threshold on a weak learner model. $H(s)$ is the entropy of each random training subset s, and p_u is a fraction of the training subset on the left or right child node. Training each regression tree amounts to minimizing the uncertainty of the conditional distributions $p(\beta^y|\beta^x)$ and $p(\gamma^y|\gamma^x)$ (e.g., multivariate Gaussian models) for shape and pose parameters, respectively, of target structures, given predictors over the training set. After forest training, the learned conditional distributions are stored at leaf nodes of each tree.

Given shape parameters $\beta^{x(p)}$ and poses $\gamma^{x(p)}$ for predictors in each training subset s a query patient data, the input features traverse each learned tree t and stop at leaf nodes. We here consider that the number of training subsets is the same as the number of trees (i.e., $t = s$). Probabilities for predicted shape and pose parameters of a target structure, $p_s\left(\beta^{y(p)}\middle|\beta^{x(p)}\right)$ and $p_s\left(\gamma^{y(p)}\middle|\gamma^{x(p)}\right)$, are obtained from the distributions stored at the leaf nodes. Finally, shape and pose parameters of a target structure for each tree are estimated by

$$\tilde{\beta}_s^{\,y(p)} = \arg\max_{\beta^{y(p)}} p_s\left(\beta^{y(p)}\middle|\beta^{x(p)}\right) \text{ and } \tilde{\gamma}_s^{\,y(p)} = \arg\max_{\gamma^{y(p)}} p_s\left(\gamma^{y(p)}\middle|\gamma^{x(p)}\right). \tag{3.21}$$

3.2.5.4 Shape prediction as a probability map

The predicted shape parameters ${\beta_s}^{y^{(p)}}$ for the target structure (each side) in the feature space are reconstructed into surface points $\bar{\mathbf{y}}_{\text{est}}^{(p)}$ in the input space using the mentioned pre-image estimation approach and then transformed by the predicted pose parameters ${\gamma_s}^{y^{(p)}}$, yielding a complete predicted region of the target ${\mathbb{y}_s}^{(p)}$.

After iterating the prediction for M random subsets (i.e., the number of trees in RF), a final probability map is calculated as an ensemble of the predicted binary volumes, $\mathrm{V}_{\text{pr}} = \frac{1}{M}\sum_{s=1}^{M} \mathrm{V}(\mathbb{y}_s^{(p)})$, giving a probability interpretation of the prediction confidence.

3.2.6 Robust prediction model

The ensemble prediction models introduced in the previous section do not consider the influence of each training subset to generate the final probability map of predicted targeting structures. If more influential training subsets, for a specific patient, are known, the prediction accuracy can be further improved, reducing the bias from the learned information. In this section, we present a robust prediction framework that enables us to estimate the contribution of each training subset to the prediction; Figure 25 (Kim et al., 2015c).

3.2.6.1 Estimating influence of atlases to prediction

We learn the non-linear mapping between features from training subsets and the prediction accuracy on different patients using a regression forest (RF) model. Pose related parameters (i.e., $\{\gamma^{x}\}$, $\{\gamma^{y}\}$, ${\gamma^{x}}^{(p)}$, and ${\gamma^{y}}^{(p)}$) are chosen as features f for each random

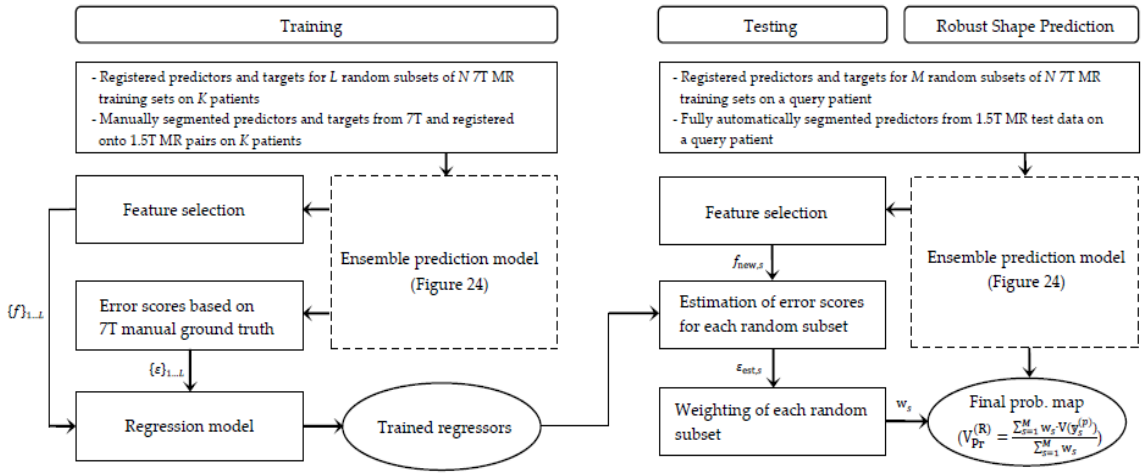

Figure 25: Robust prediction framework (Kim et al., 2015c)

subset, since the poses for the target and its predictors on the training set and patient data are highly correlated with the prediction accuracy. During the regression forest training, the prediction using L random subsets of N 7T MR training sets on K patients is performed within our prediction framework (see Figure 24). Prediction results for each random subset are then evaluated, calculating an error score that averages measurements from the 7T (manual) ground truth,

$$\varepsilon = \mu_g\left(\epsilon_g/\delta_g\right) + \mu_l(\epsilon_l/\delta_l) + \mu_o(\epsilon_o/\delta_o) + \mu_v(\epsilon_v/\delta_v) + \mu_{\mathrm{DC}}((1-\mathrm{DC})/\delta_{\mathrm{DC}}) \qquad (3.22)$$

where ϵ_g, ϵ_l, ϵ_o, and ϵ_v are distances between prediction and ground truth segmentation, respectively, for centers, sizes, orientation angles, and volumes. DC is the overlapping ratio of volumes, $(\,2(\mathrm{V_A}\cap\mathrm{V_B})/\,(\mathrm{V_A}+\mathrm{V_B})\,)$, where $\mathrm{V_A}$ and $\mathrm{V_B}$ are the volumes of the

prediction and ground truth segmentation, respectively. Also, μ and δ are weights and upper-bounds for the corresponding errors. In this work, under acceptable error bounds for DBS targeting (i.e., ε<1), we set μ=[0.35 0.15 0.1 0.15 0.25] and δ=[1mm 1mm 15° 30mm^3 35%], weighting more ϵ_g and DC.

We again exploit the regression forest (RF) model (Breiman, 2001), which uses an ensemble of binary trees, learning the nonlinear mappings between features f and ε from each training random subset. Each tree optimally splits training samples, maximizing information gain among the distribution of error scores, and learned conditionals $\mathrm{p}_t(\varepsilon|f)$ are stored on leaf nodes. Given a query patient and each random sets of training sets, each feature f_{new} is pushed down on learned trees and stops at leaf nodes, resulting in $\mathrm{p}_t(\varepsilon_{new,s}|f_{new,s})$. The conditional distributions are averaged over all N_{tree} trees, and finally error scores of each random subset are estimated as

$$\varepsilon_{est,s} = \underset{\varepsilon}{\mathrm{argmax}}\left(\frac{1}{N_{tree}}\sum_{t=1}^{N_{tree}} \mathrm{p}_t(\varepsilon_{new,s}|f_{new,s})\right) \quad (3.23)$$

3.2.6.2 Weighted ensemble of shape predictions

For the M estimated error scores $\bar{\varepsilon}_{est,s}$, normalized to [0 1], a weighing function is defined as a sigmoid function $\mathrm{w}_s = \exp(-(\bar{\varepsilon}_{est,s})^3/\sigma^2))$, where σ is the mean of $\{\bar{\varepsilon}_{est,s}\}$. This allows an ensemble of predictions, with larger weighting learned information from training subset yielding lower error scores (i.e., more influential atlases for the prediction).

A final probability map on the query patient is computed by averaging predicted binary volumes from the M random subsets: $\mathrm{V}_{\mathrm{pr}}^{(\mathrm{R})} = \frac{\sum_{s=1}^{M} \mathrm{w}_s \cdot \mathrm{V}(\mathrm{y}_s^{(p)})}{\sum_{s=1}^{M} \mathrm{w}_s}$.

3.2.7 Application to clinical STN-DBS targeting

We apply our proposed prediction framework in surgical planning for DBS targeting of the subthalamic nucleus (STN). The STN is a small approximately convex structure which is divided into the motor territory (as the target area for DBS surgery for Parkinson's disease for example) in the postero-lateral region and the limbic territory of the anteromedial region, and is surrounded by several sub-cortical regions - zona incerta, medial lemniscus, Edinger-Westphal nucleus, internal capsule, Substantia nigra (SN), Red nuclei (RN), Interal globus pallidus (GPi), and Thalamus (Tha) (Abosch et al., 2010; Kerl et al., 2012). The DBS of the STN has shown its effectiveness for advanced PD and potentially OCD (Abosch et al., 2010; Cho et al., 2010).

Superior contrast and high resolution on the 7T MR data have enabled to directly visualize and identify sub-cortical structures within the Basal ganglia and thalamic, particularly, STN and its adjacent structures (Abosch et al., 2010, Cho et al., 2010; Kerl et al., 2012; Lenglet et al., 2012). Additionally, volumetric models of sub-cortical structures have been built by exploiting multi-contrast of SWI and T_2W images acquired at 7T, thereby providing the spatial information - location, dimension, and orientation - of the structures (Abosch et al., 2010; Lenglet et al., 2012). Nevertheless, since 7T MR data is not

widely available for clinical use, the STN localization on the conventional clinical MR data (1.5T) needs to be further taken into account.

Figure 26 shows SN, STN, GP and RN regions in both axial and coronal T_2W images obtained with the 1.5T and 7T MRI pair for the same patient, respectively. Axial T_2W 7T MR data was registered onto the T_2W 1.5T MR data for comparison (Duchin et al., 2012). For further comparison of 7T MR data with 1.5T MR data, see also Cho et al. (2010).

We observe that it is not possible to identify the STN from the SN, the GPi in the GP region on the 1.5T MR imaging, due to weak intensities and low SNR within those regions, whereas 7T MR imaging provides detailed information for those regions. The RN

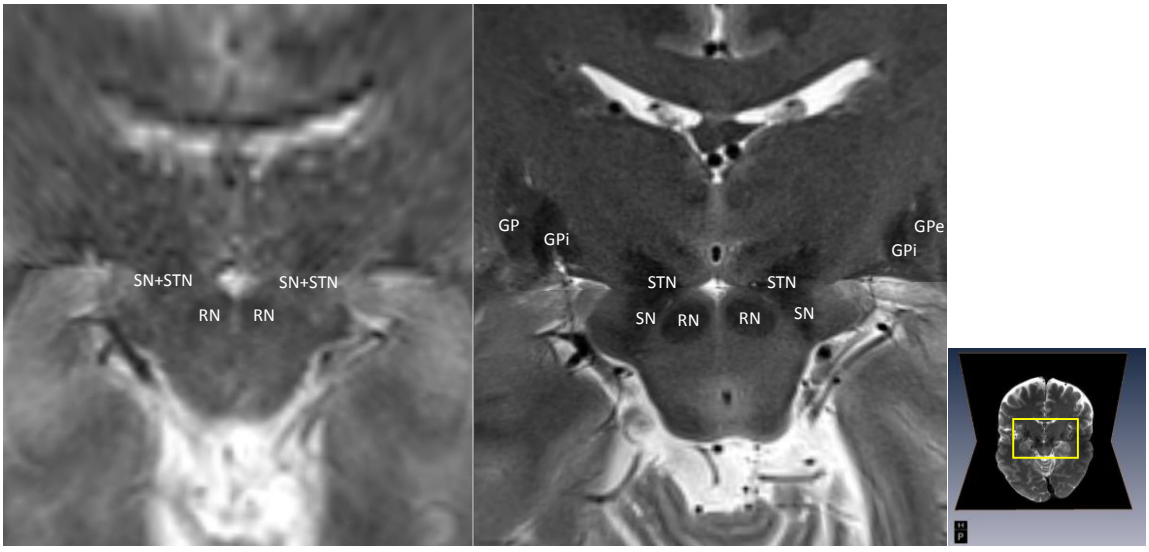

(a) (b)

Figure 26: Visual comparison of brain sub-cortical structures - SN, STN, RN, and GP regions - from (a) the 1.5T (current practice) and (b) 7T T_2W MRI (registered onto the 1.5T pair) in the axial and coronal plane.

and a combined region of SN and STN are fairly easy to identify compared to other structures on the 1.5T MR imaging, even if the regions are much more clearly visualized on the 7T MRI. Moreover, several studies have utilized the RN (e.g., relative positions of the STN to the RN) as the guidance to implant electrode into the STN during the DBS (Dormont et al., 2010; Hamid et al., 2005; Starr et al., 2002). A combined regions of SN and STN also has high correlation with the STN. Note again that our goal is to accurately localize the STN where it cannot be differentiated from those regions on the 1.5T MRI.

Accordingly, in a standard clinical scenario, we choose the RN and a combined region of SN and STN as a potential predictor of the STN. In our prediction framework, surface points for both hemispheres of the predictors - RN and a combined region of SN and STN - in the training sets obtained on the 7T MR imaging are represented as $\mathbb{x}_i$, and pre-segmented predictors on the test data are encoded as their surface landmark vectors $\mathbb{x}^{(p)}$, respectively., and the previously described prediction framework is applied.

3.3 Experimental results

3.3.1 Experimental setup

We selected 15 Parkinson's patients from 46 subjects in our database as test sets for clinical STN targeting. For each query patient, 16 similar atlases (out of 45 patients) were chosen based on the MI similarity metric on mid-brain regions including the Basal ganglia and thalamus of the 1.5T T_2W MRI. The SN, STN, and RN structures were manually segmented from 7T T_2W MRIs of the similar atlases (Lenglet et al., 2012; Kim et

al., 2014) and linearly registered onto the corresponding 1.5T T_2W MRI pairs, following the co-registration protocol (Duchin et al., 2012). 7T and 1.5T T_2W MRI pairs from 16 similar atlases and corresponding structures (registered onto 1.5T space) were then non-linearly transformed onto the 1.5T T_2W MR Test data (resampled to 0.5x0.5x0.5mm^3) of the query patient as in Figure 22. We automatically segmented the RN and combined region of SN and STN as potential predictors of the STN targeting on the 1.5T T_2W MRIs of 15 query PD patients based on 7T MR appearance, local intensity, and shape modeling (see also Figure 23). Finally, we used manually segmented predictors from 7T MRI (registered onto the 1.5T MRI pair) of the query patient for the STN prediction to investigate the influence of each predictor's quality to the prediction accuracy.

We randomly built M=10, 50, 100, 150, and 200 training subsets with size N=11 out of 16 similar atlases to test the effects of our ensemble prediction. For the robust framework, we performed forest training offline with N_{tree}=100, using features from L=28000 random subsets of N=11 from K=14 PD patients, leaving one out and estimated error scores online using the learned probabilistic mapping, given M random subsets and each predictor on each query patient.

3.3.2 Prediction measurements

Final probability maps of the STN prediction were thresholded by 0.3, and the prediction accuracy was evaluated by the DC, errors in centroid, dimension, orientation angles, and error scores between the predicted STN and its ground truth (manually

segmented STN) from the 7T T_2W MRI (registered onto 1.5T MRI pairs) over the 15 query patients.

In addition to the DC, we compute the centroids $\boldsymbol{g} = (g_{cor,}\, g_{sag,}\, g_{axi})$ in coronal, sagittal, and axial directions, the lengths of three semi-axes (radii) $\boldsymbol{l} = (l_{x,}\, l_{y,}\, l_z)$, and the orientation angles $\boldsymbol{o} = (\phi,\ \theta,\ \psi)$ for inertia ellipsoids of the predicted STNs (i.e., 3D binary volumes reconstructed from the predicted surface landmark points for the STN) and its manual segmentation, respectively, to analyze the similarity of their geometric information. More specifically, $\boldsymbol{g}$ is calculated as the mean of each coordinate for the landmark points; $\boldsymbol{l}$ is computed from the first three largest eigenvalues obtained by performing PCA for n_{y} centered landmark points; and $\boldsymbol{o}$ is obtained calculating the Euler angles from the rotation matrix which consists of the corresponding eigenvectors (Slabaugh, 1999). Finally, the errors (as $\mathcal{L}^2$ norm), $\boldsymbol{\epsilon_g}$, $\boldsymbol{\epsilon_l}$, and $\boldsymbol{\epsilon_o}$ between measurements of the manual ground truth and its predicted one are computed. An error score defined in (3.22) averages all the measurements (especially, used as a measure for the influence of each training subset in the prediction). Note that $\boldsymbol{\epsilon_g}$ and DC are considered the two most important error measures in practice since the DBS targeting of the STN is determined based on those parameters (e.g., its center or dorsal part).

In addition, and more importantly, we qualitatively investigated if small sub-regions (posterior-dorsal part) of the predictions are completely inside typical DBS targeting sub-regions (e.g., motor territory) of the ground truth STN (7T). Such validation

might demonstrate the clinical feasibility of our proposed approach for the automatic patient-specific direct targeting.

3.3.3 STN prediction results on standard clinical 1.5T MR datasets

In this section, prediction results of the STN on the clinical 1.5T MRI using our proposed approach are presented. The prediction accuracy in our framework is mainly influenced by the selected predictors for the DBS target structures, used training atlases, and shape relationship learning methods.

We first perform the STN prediction using automatically segmented predictors on each 1.5T MR test data and manually segmented predictors from 7T MRIs (registered onto 1.5T MRI pairs) of the same patients, respectively, with two bagging regression methods - bagged PLSR and RF. We also compare the prediction performance using each predictor - RN alone, SN+STN alone, and RN with SN+STN. Additionally, we predict the STN without and with the contribution of different training subsets to the prediction accuracy. Finally, we validate that our robust prediction approach on the clinical 1.5T MRI outperforms the basic multi-atlases based labeling fusion method and deformable segmentation framework (described in Section 3.2.4) and shows clinically acceptable results, compared to the MRI mapping of the post-operative electrode trajectory.

3.3.3.1 Evaluation of predictors

Each measurement for the automatic segmentation results of predictors – RN and SN+STN on 1.5T MRIs from manually segmented ones on the 7T MRIs (registered onto

the 1.5T MRIs) over 15 PD patients is summarized in Table 4. Center position and size of each automatically segmented predictor and its manual segmentation are comparable, based on average $\boldsymbol{\epsilon_g}$ and $\boldsymbol{\epsilon_l}$ around 1mm. However, $\boldsymbol{\epsilon_o}$ in automatically segmented RN structures is very large, and this might be attributed to their irregular sphere-like shapes (incorrect three semi-axes). Figure 27 visualizes surfaces of automatically segmented RN and SN+STN, comparing to manual segmentation from 7T (registered onto 1.5T MRI pairs) on the 15 PD patients. Complete shapes of automatically segmented predictors do not accurately match with their manual segmentation. However, we should note that manual versions were obtained from 7T MRIs, and thus visible (but unclear) regions on the 1.5T

Table 4: Averaged distance errors of centroids, lengths of semi-axes, and orientation angles between automatically segmented predictors (1.5T) and manual ground truth segmentations (7T), their volumes, and DC values from 15 query patients.

Side	Measurements	RN	SN+STN	RN and SN+STN
Left	$\boldsymbol{\epsilon_g}$ (mm)	0.91±0.41	1.06±0.49	0.83±0.35
	$\boldsymbol{\epsilon_l}$ (mm)	0.76±0.42	1.18±0.61	-
	$\boldsymbol{\epsilon_o}$ (degree)	126±87	19.2±12.3	-
	DC (%)	73.14±8	69.7±5.3	-
	Error score	1.74±0.73	1.57±0.61	-
	Volume (mm^3)	223.7±54.2 (259.5±53.7*)	637.2±151.4 (648.3±99.7*)	-
Right	$\boldsymbol{\epsilon_g}$ (mm)	1.17±0.64	1.18±0.69	1±0.52
	$\boldsymbol{\epsilon_l}$ (mm)	0.78±0.42	1.27±0.63	-
	$\boldsymbol{\epsilon_o}$ (degree)	108±102	22.4±10.4	-
	DC (%)	68.5±9.5	67.8±9.5	-
	Error score	1.79±0.65	1.83±0.76	-
	Volume (mm^3)	264.4±84 (257.2±64*)	716.1±216.8 (655.7±110.3*)	-

(*) represents volumes of manual segmentation

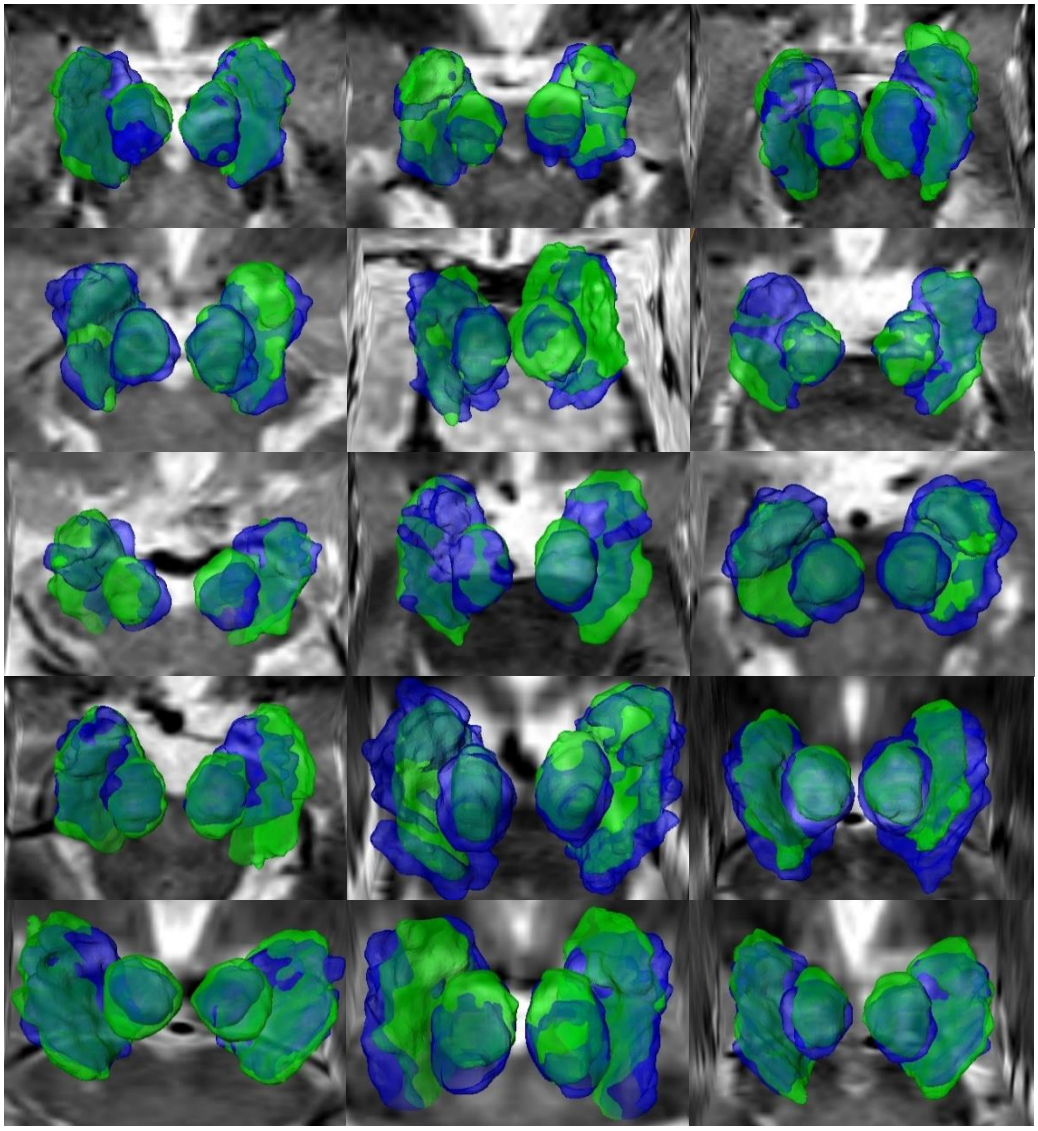

Figure 27: Visualization of automatically segmented predictors (green) - RN and a combined region of SN and STN - overlaid with their manual segmentations from the 7T MRI pairs (blue) on the axial plane of the 1.5T T_2W MRI from the 15 PD patients.

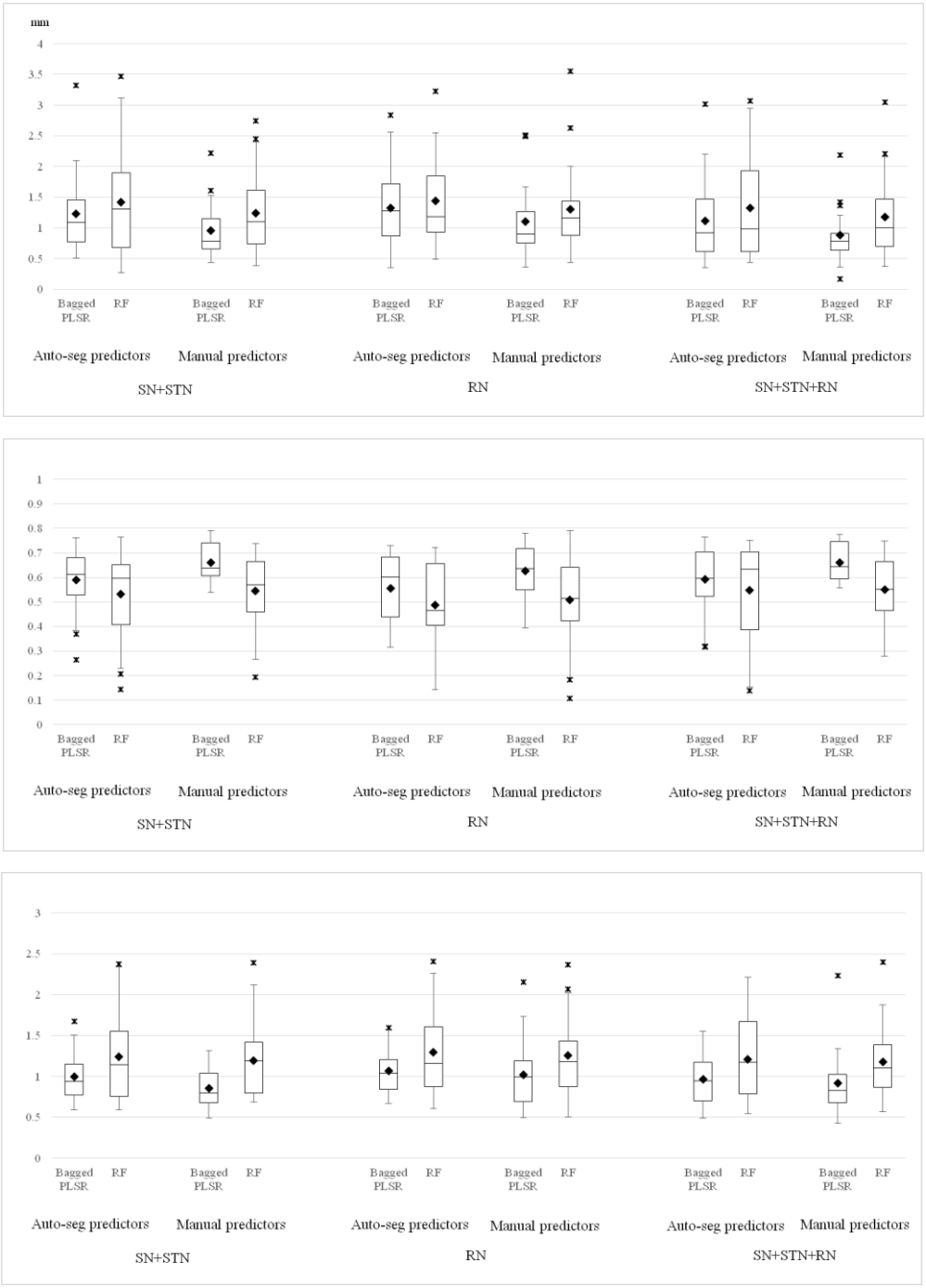

Figure 28: Box plots of (a) ϵ_g, (b) DC values, and (c) error scores for *left* predicted STNs with automatically and manually segmented predictors, respectively.

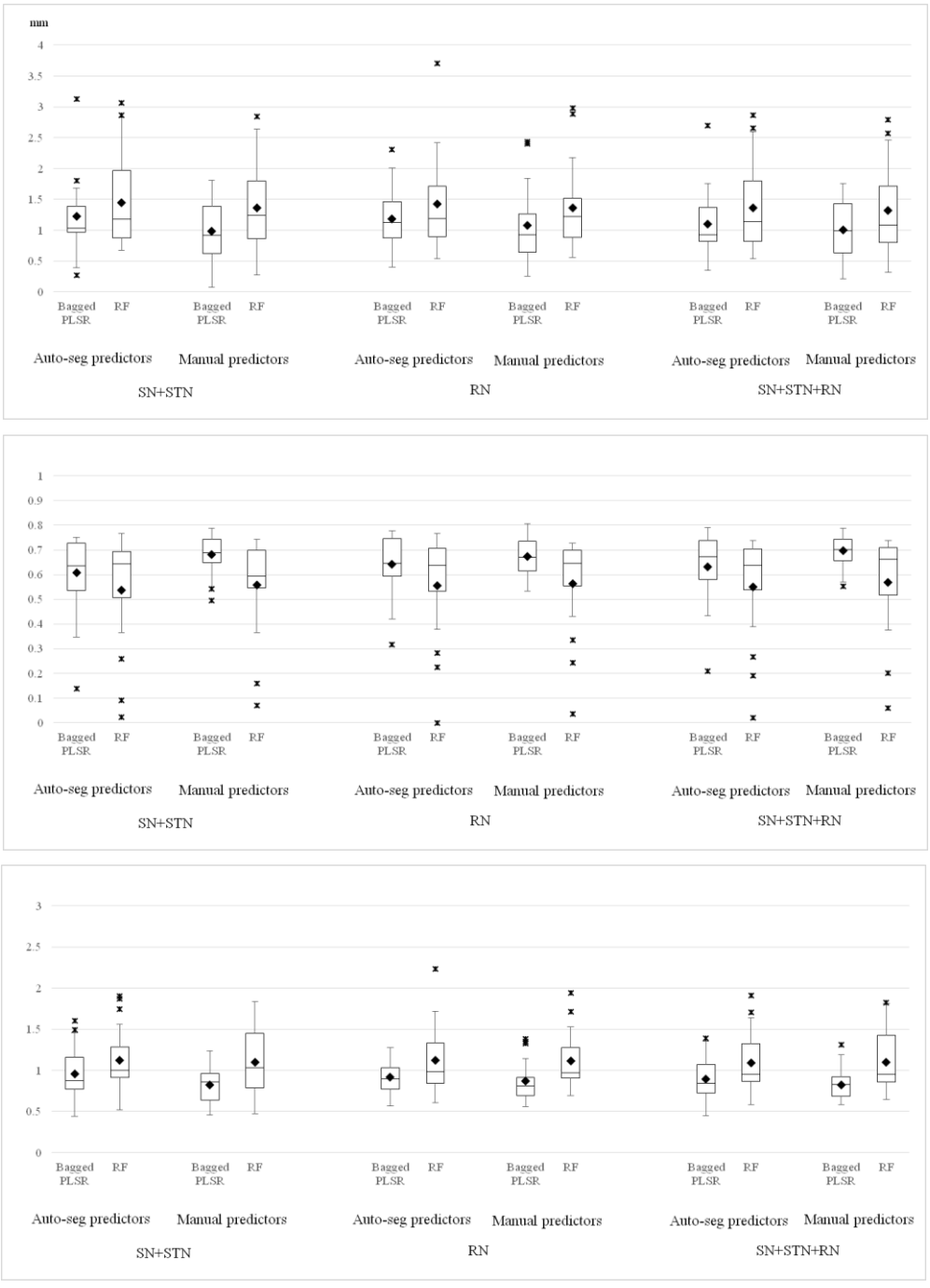

Figure 29: Box plots of (a) ϵ_g, (b) DC values, and (c) error scores for *right* predicted STNs with automatically and manually segmented predictors, respectively

MRI pairs might not fully reflect such 7T MR structures.

Figure 28 and 29 show ϵ_g, DC, and error scores for prediction results of the left and right STN using 100 training subsets with each predictor automatically segmented on the 1.5T test data and manually segmented on the 7T MRI (registered onto the 1.5T MRI pairs), respectively, over 15 PD patients.

Overall STN prediction using manually segmented predictors show better performance, yielding smaller ϵ_g, error scores and higher DC values ($p<0.05$) than using automatically segmented predictors. This explains that improving the quality of segmented predictors on the 1.5T test data considerably increases the prediction accuracy. Also, ensemble prediction by bagged PLSR based shape relationship learning produces significantly better results than using the RF method for all the cases of predictors ($p<0.05$ in ϵ_g and $p<0.01$ in DC and error scores for using manually segmented predictors and $p<0.05$ in ϵ_g, DC, and error scores for using automatically segmented predictors). Particularly, prediction results by the RF method using even manually segmented predictors are worse than those obtained with automatically segmented predictors using the bagged PLSR.

Additionally, we observe that prediction results using all the structures (i.e., RN with SN+STN) for both manually and automatically segmented predictors are slightly better than using other single structures. In other words, this means that using learned shape relationships between the STN and combination of SN, STN, and RN as predictors

is more useful for the STN prediction. We can see that the influence of large orientation angle errors in automatically segmented RNs to the prediction was not significant since prediction results using automatically segmented RNs are comparable to those using SN+STN structures.

We demonstrate that our ensemble predictions using the bagged PLSR with automatically segmented SN+STN and RN and 100 training subsets produces still comparable results to its manual ground truth from the 7T MRI pair, based on clinically feasible measurements ($\boldsymbol{\epsilon_g}$ = 1.11±0.71mm and 1.1±0.59mm, $\boldsymbol{\epsilon_l}$ = 0.92±0.6mm and 0.59±0.29mm, $\boldsymbol{\epsilon_o}$ = 14.5±9.7° and 15.9±10.7°, volume=118±24.5mm^3 and 113±22.6mm^3 (125.7±22.7mm^3 and 124±24mm^3 for manual ones), DC=59±14.4% and 63.1±15.2%, and error score=0.96±0.3 and 0.89±0.26 in left and right side, respectively), although using manually segmented predictors can further improve the prediction accuracy.

3.3.3.2 Effect of influential training subsets in prediction

With automatically segmented RN, combined region of SN and STN, and different numbers of training subsets (i.e., M=10, 50, 100, 150, and 200), the ensemble prediction based on bagged PLSR and RF, respectively, and robust prediction (for estimated error scores and true ones) were performed to test the contribution of influential training subsets to the prediction accuracy within our framework. Box plots of $\boldsymbol{\epsilon_g}$, DC, and error scores in the STN prediction results for all the cases are shown in Figure 30 and 31. Ensembles of the STN structures that were manually segmented on the 7T MRIs

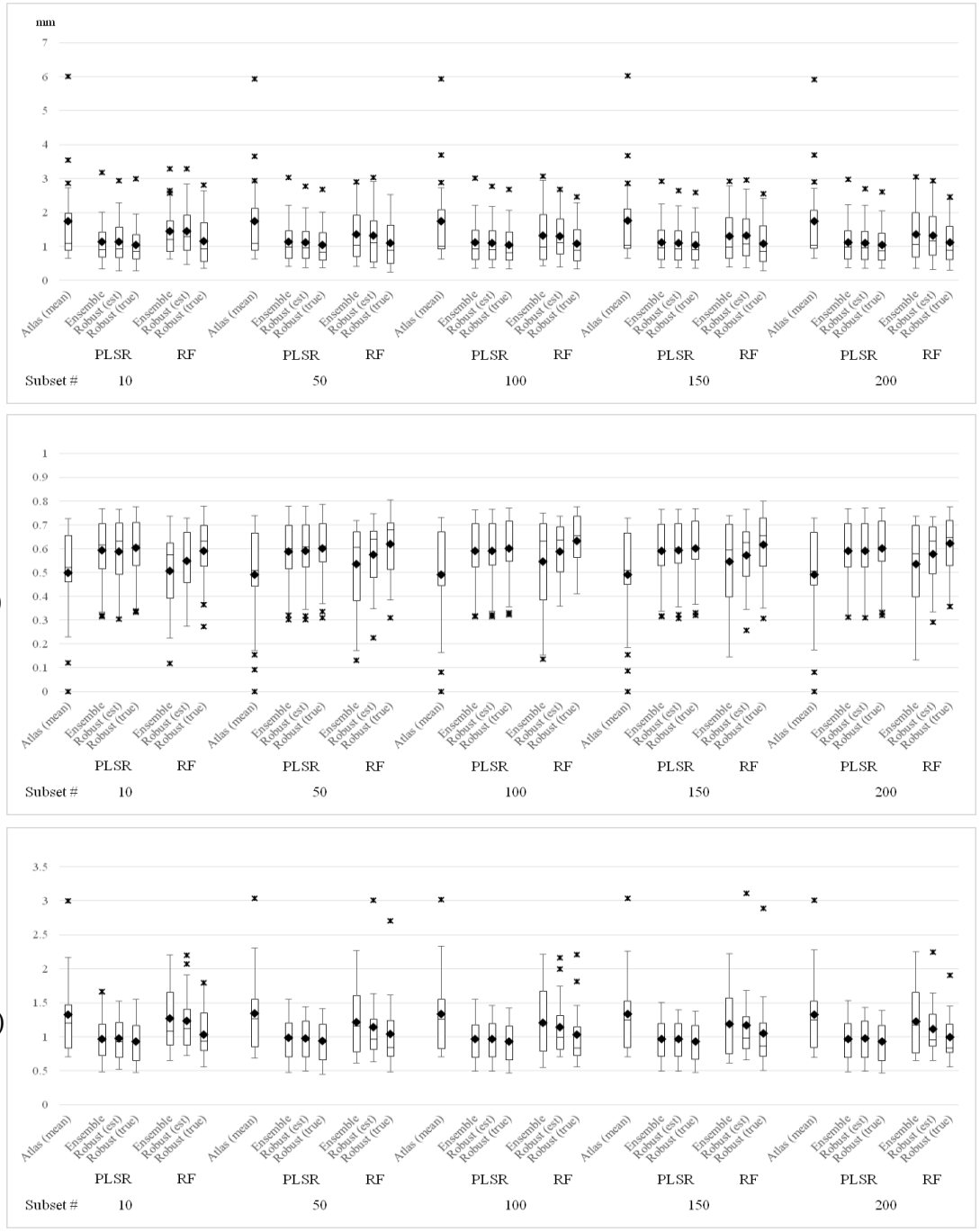

Figure 30: Box plots of (a) ϵ_g, (b) DC values, and (c) error scores for 7T MR atlases based mean STN (*left*), predicted STNs (*left*) using ensemble prediction (by bagged PLSR and RF learning), and robust prediction (for estimated error scores and true ones) with automatically segmented SN+STN and RN as predictors and a different number of random subsets.

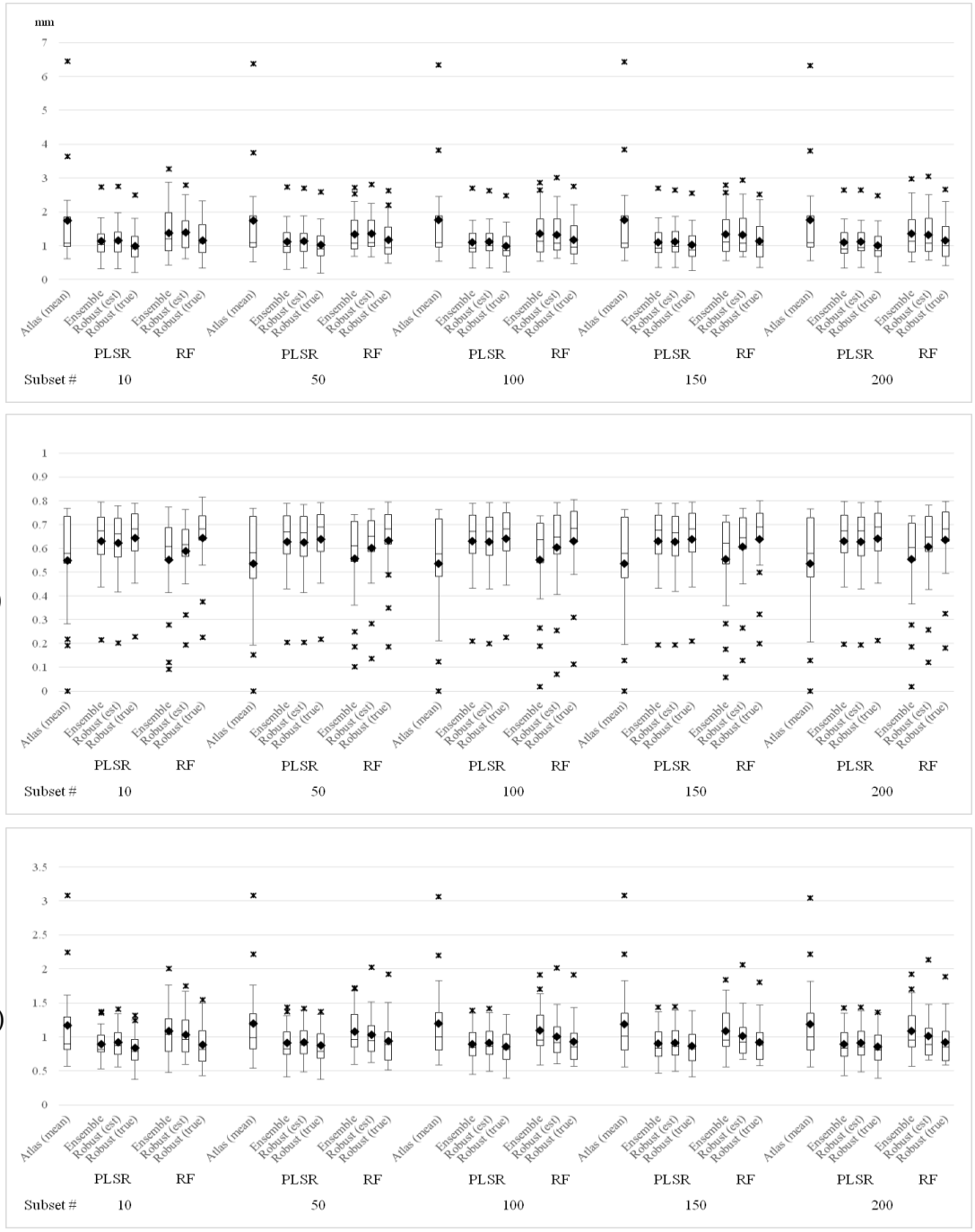

Figure 31: Box plots of (a) ϵ_g, (b) DC values, and (c) error scores for 7T MR atlases based mean STN (*right*), predicted STNs (*right*) using ensemble prediction (by bagged PLSR and RF learning), and robust prediction (for estimated error scores and true ones) with automatically segmented SN+STN and RN as predictors and a different number of random subsets.

(registered onto 1.5T MRI pairs) from different number of training subsets are also compared (i.e., probability map of binary volumes for the STN: $\frac{1}{M}\sum_{s=1}^{M} m_{y_s}$). Note that the 7T manual STNs from similar atlases were non-linearly registered onto the 1.5T MR test data of the query patient, and thus we consider the 7T atlases based mean STN as the basic multi-atlases based labeling fusion result that mainly relies on the registration quality (between 1.5T MRIs).

Overall prediction results on the 1.5T MR datasets over 15 PD patients are much closer to the manual ground truth STNs (7T) than the 7T atlases based mean STN for all the number of training subsets, showing the prediction potential within our proposed framework (especially, $p<0.5$ in $\boldsymbol{\epsilon_g}$, DC, and error scores for using the bagged PLSR). Using the bagged PLSR based learning still yields better STN prediction results than using the RF over all the number of training subsets (e.g., average 20% smaller in $\boldsymbol{\epsilon_g}$, 25% smaller in error scores, and 10% higher in DC). Particularly, prediction results using the RF mainly depend on the quality of the 7T atlases based mean STN. This means that such non-linear regression method might often fail to capture the correct information from highly variable shape relationships on training atlases.

We also observe that predictions using a large number of training subsets do not show a significant improvement. Prediction results from the small number of training subsets are comparable to those from large enough number of subsets. This might prove that the pre-selection of similar atlases for the query patient contributed to reducing the

variability of shape relationships between the STN and its predictors (see also similar results of 7T atlases based mean STNs for different number subsets). However, we should note that an ensemble of prediction results from a large enough number of training subsets might provide a good consensus, reducing the uncertainty in the prediction. For this reason, we typically use 100 random training subsets for the STN prediction.

Additionally, the robust prediction produces more accurate results than ensemble prediction, estimating error scores for each training subsets. This illustrates that training random subsets with lower error scores, meaning more influential atlases to the prediction contributes to increasing the accuracy. The improvement in the robust prediction with estimated error scores is not statistically significant. Robust prediction with true error scores from 7T manual ground truth STN is also presented for comparison ($p<0.01$ in all the measurements for using both the RF and the bagged PLSR from the ensemble prediction results). Particularly, robust prediction results using the RF are further improved than using the bagged PLSR. This might also explain that the robust framework properly compensates for less accurate prediction results, especially using the RF, showing the effect of the bias reduction. For example, the robust predictions with true error scores using the RF are comparable to even the ensemble prediction using the bagged PLSR (without considering the influential atlases). In other words, the ensemble prediction using the bagged PLSR still yields relatively small errors in measurements (average $\boldsymbol{\epsilon_g}$=1.1mm, DC=60%, and error scores=0.9), and thus the effect of the robust

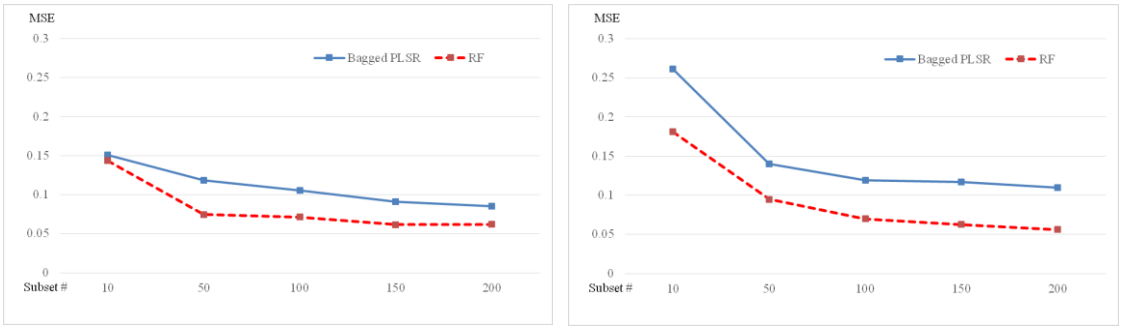

(a) (b)

Figure 32: Average MSE between estimated error scores and true ones (from 7T manual ground truth STN) for (a) predicted left STN and (b) predicted right STN using the bagged PLSR and the RF according to the different number of training subsets within the robust framework.

framework was not significant (see also the difference of measurements amongst ensemble, robust (with estimated error scores), and robust prediction (with true error scores) using the bagged PLSR and the RF, respectively, in Figure 30 and 31).

Figure 32 represents average mean squared errors (MSE) between estimated error score within our robust framework and true error scores (7T) for the different number of training subsets over 15 PD patients. The MSE of estimated error scores is lower in the RF than using the bagged PLSR. This might explain why the robust framework further improved ensemble prediction results when using the RF than using the bagged PLSR. Also, the smaller the number of training subsets, the higher the MSE of the estimated error scores. This also proves that the robust framework was more effective with large enough number of subsets (see differences between 10 subsets and 200 subsets when using the RF in Figure 30 and 31).

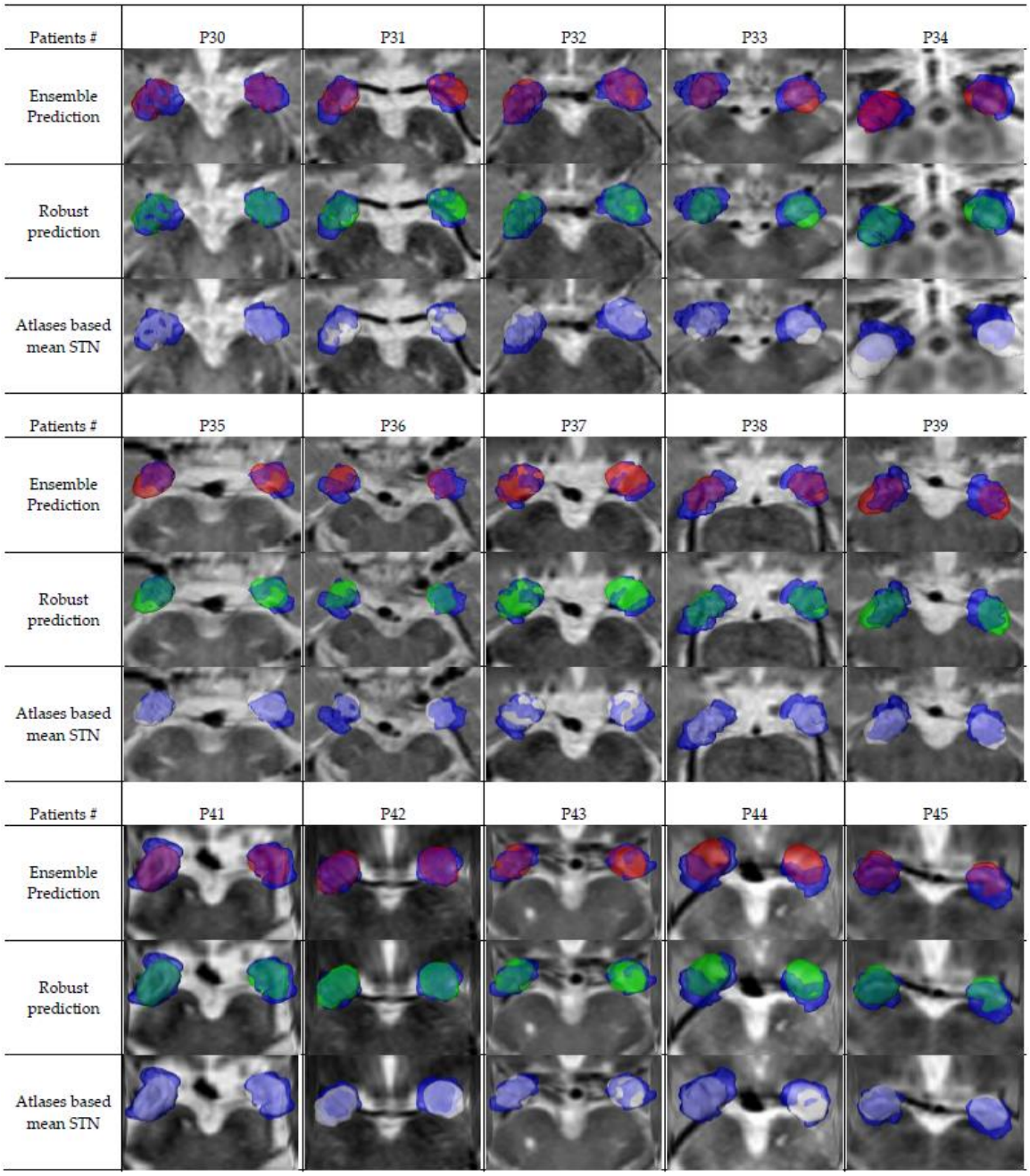
Patients #
P30
P31
P32
P33
P34
Ensemble Prediction
Robust prediction
Atlases based mean STN
Patients #
P35
P36
P37
P38
P39
Ensemble Prediction
Robust prediction
Atlases based mean STN
Patients #
P41
P42
P43
P44
P45
Ensemble Prediction
Robust prediction
Atlases based mean STN

(a)

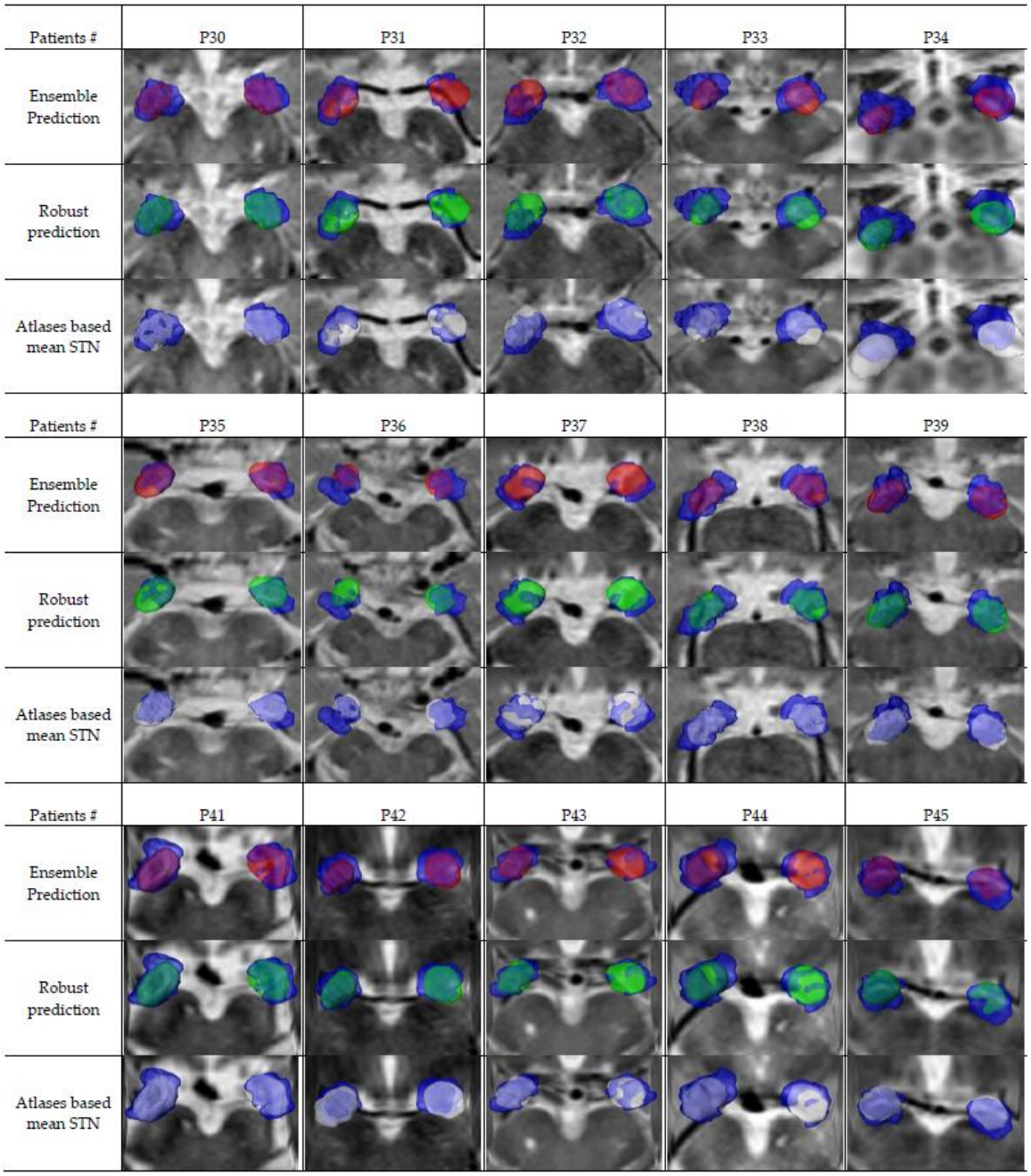

(b)

Figure 33: 3D visualization of ensemble prediction (red), robust prediction results (estimated error scores; green) with automatically segmented RN and SN+STN and 100 training subsets using (a) the bagged PLSR and (b) the RF, respectively, and ensembles of similar atlases based mean STNs (white), overlaid with the 7T manual ground truth (blue) on the axial plane of the 1.5T T_2W MRI from 15 PD patients.

Finally, Figure 33 displays 3D visualizations for ensemble, robust prediction results (with estimated error scores) of the STN using the bagged PLSR and the RF, respectively, with 100 training subsets and automatically segmented predictors, and ensembles of 7T atlases based mean STNs and compare them with the 7T manual ground truth STN on the 1.5T T_2W MRIs of the 15 PD patients. Visual difference between ensemble and robust prediction results is not significant (the improvement of the robust prediction in measurements was also small). Ensembles of 7T atlases based mean STNs are highly variable across patients, i.e., some of them are accurate, but some are very far from the ground truth.

3.3.3.3 Comparison with other segmentation methods

Statistical shape model based deformable segmentation such as the unified ASM and AAM introduced in Section 3.2.4 and various multi-atlases based labeling fusion methods have been widely applied to, in particular, facial landmark alignment and medical image segmentation challenges. However, such models assume that a test image has consistent appearances with training images, and target structures can be distinguished from adjacent structures on the test data. In other words, manual segmentation should be available on the training data and even on the test data. We aim at solving the localization problem of the structure which is not normally possible to identify on standard clinical low-field data. In our scenario, it is not feasible to manually segment the target structures on the test data, and thus it is hard to build high quality

training shapes. These reasons do not allow us to use such popular segmentation methods. Note that our approach exploits predictors that are fairly visible on the 1.5T MRI (segmented by applying ASM+AAM based deformable segmentation), instead of directly segmenting the STN. In this section, we compare our robust prediction results (using the bagged PLSR) with segmentation results using a unified ASM and AAM based deformable segmentation and majority voting results of the STNs from registered 16 similar atlases onto test data.

Figure 34 and 35 show box plots of each measurement for comparison. Also, significant values (p-value) in our robust prediction from two segmentation methods are summarized in Table 5. These results validate that our robust prediction results significantly outperform these important existing segmentation methods, especially under the scenario where the STN needs to be localized on the clinical 1.5T MR data. Finally, 3D visualization of the results, along with the 7T manual ground truth, is shown in Figure 36. Majority voting and deformable segmentation results are also highly variable across 1.5T MR datasets from patients. Specifically, two segmentation methods fail to correct inaccurate initialization (meaning far mean STNs of atlases from the target region). This could explain that the segmentation results mainly depend on the quality of test data that results in decreasing the accuracy of registration.

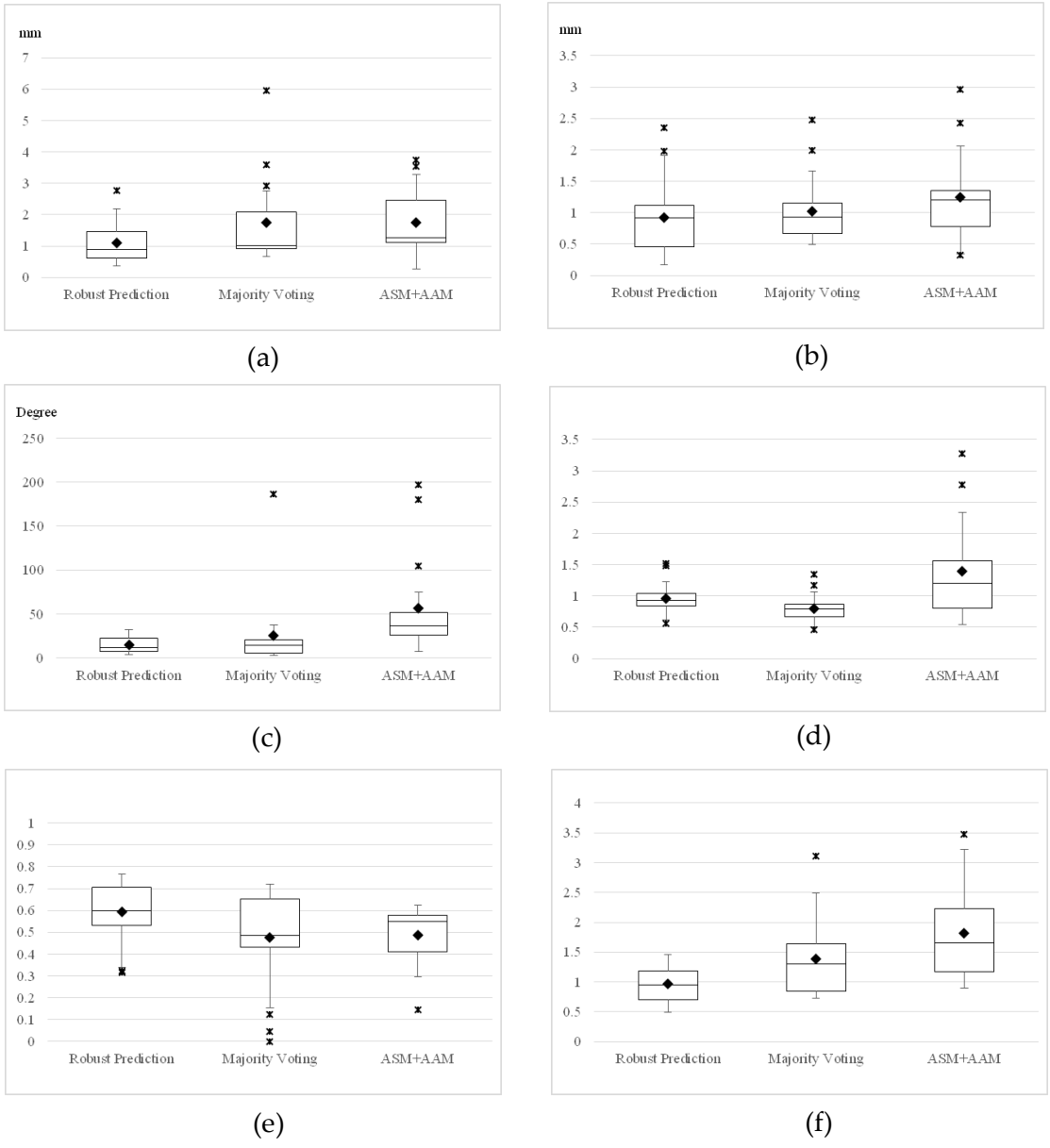

Figure 34: Box plots of (a) ϵ_g, (b) ϵ_l, (c) ϵ_o, (d) relative volume (V/V_{manual}), (e) DC values, and (f) error scores for our robust STN prediction (*left side*) (using the bagged PLSR with estimated error scores, 100 training subsets, and automatically segmented RN and SN+STN), segmentation results of the *left* STN using majority voting (from 16 similar atlases), and ASM+AAM based deformable shape fitting, respectively, across 15 PD patients.

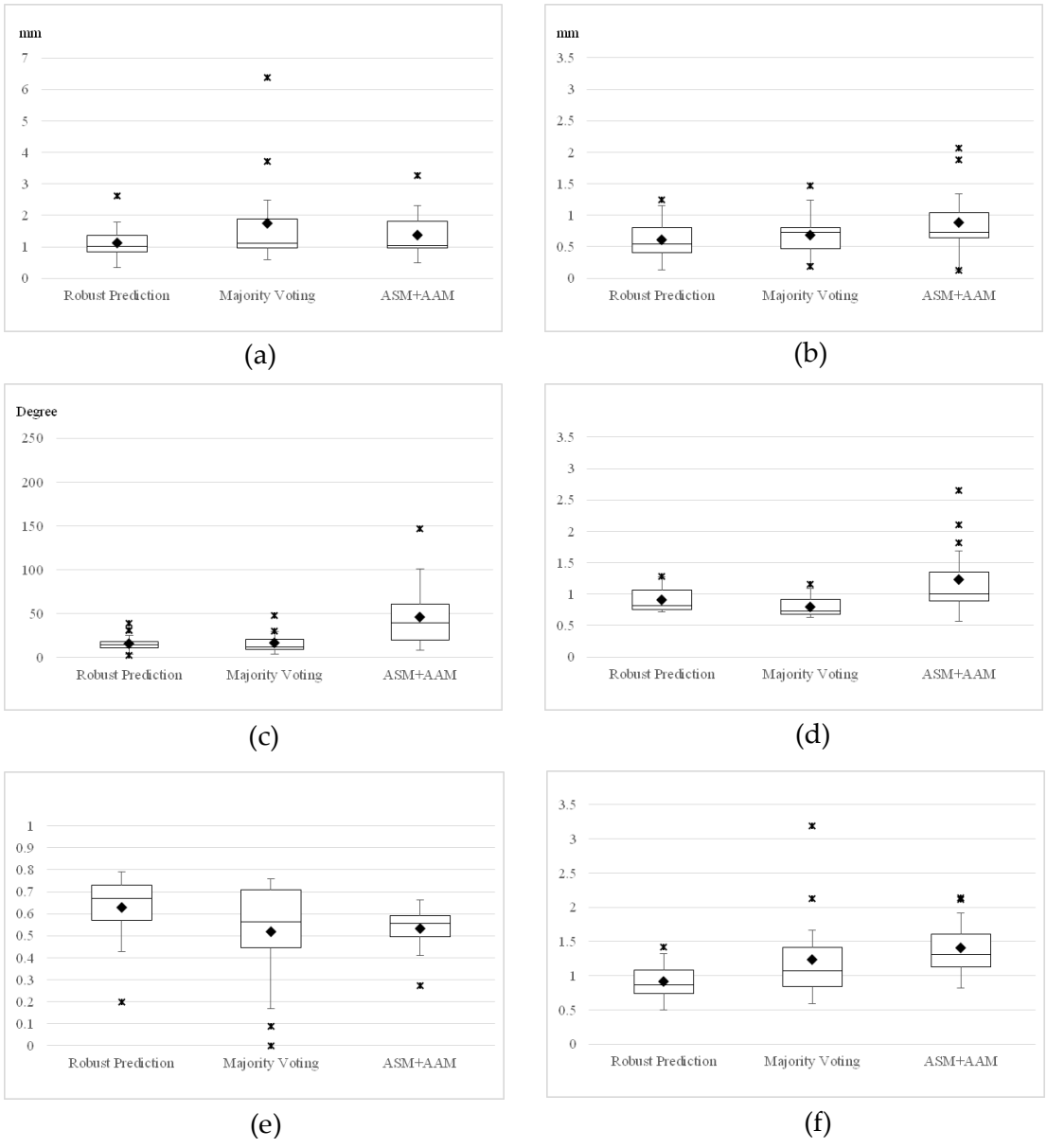

Figure 35: Box plots of (a) ϵ_g, (b) ϵ_l, (c) ϵ_o, (d) relative volume (V/V_{manual}), (e) DC values, and (f) error scores for our robust STN prediction (*right side*) (using the bagged PLSR with estimated error scores, 100 training subsets, and automatically segmented RN and SN+STN), segmentation results of the *right* STN using majority voting (from 16 similar atlases), and ASM+AAM based deformable shape fitting, respectively, across 15 PD patients.

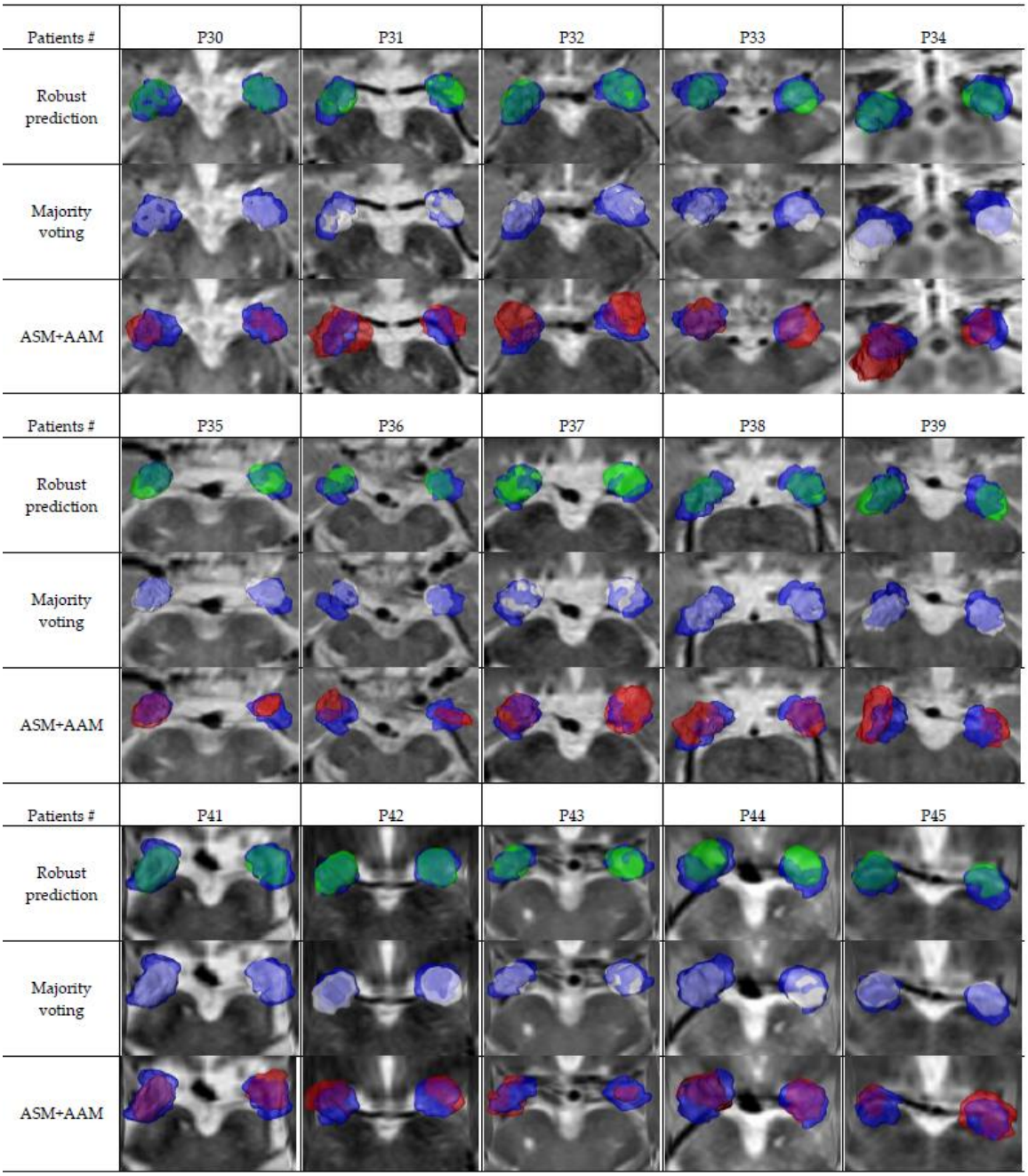

Figure 36: 3D visualization of our robust prediction (green) (using the bagged PLSR with estimated error scores, 100 training subsets, and automatically segmented RN and SN+STN), segmentation results of the STN using majority voting (from 16 similar atlases; white), and ASM+AAM based deformable shape fitting (red), respectively, overlaid with 7T manual ground truth (blue) on the axial plane of the 1.5T T_2W MRI from 15 PD patients.

Table 5: Statistical analysis for significance of each measurement in our robust prediction results (with estimated error scored) using the bagged PLSR from segmentation results using majority voting (from similar atlases) and ASM+AAM based deformable shape fitting, respectively, on the 1.5T T_2W MR datasets from 15 PD patients. The p-values correspond to one-tailed and paired two-sample t-tests. Significant values (p<0.05) are represented in bold.

Methods	p-values for left predicted STN						p-values for right predicted STN					
	ϵ_g (mm)	ϵ_l (mm)	ϵ_o (degree)	Relative Volume (V/V_{Manual})	DC (%)	Error score	ϵ_g (mm)	ϵ_l (mm)	ϵ_o (degree)	Relative Volume (V/V_{Manual})	DC (%)	Error score
Majority Voting	**0.04**	**0.03**	0.2	**0.00**	**0.005**	**0.01**	**0.04**	**0.02**	0.4	**0.00**	**0.01**	**0.02**
Deformable Segmentation (ASM+AAM)	**0.01**	0.08	**0.01**	**0.02**	**0.03**	**0.004**	**0.05**	0.06	**0.004**	**0.02**	**0.01**	**0.00**

3.3.3.4 Qualitative validation for guidance of the STN-DBS targeting

Our proposed approach has demonstrated accurate STN prediction results. To further validate its value for DBS direct targeting, we visually checked if small sub-regions (especially, in a posterior-dorsal part) of the predicted STN (obtained from our robust prediction using the bagged PLSR learning from 100 training subsets with automatically segmented RN and SN+STN – best results in all the cases), are placed inside typical DBS motor sub-regions from the ground truth STN obtained from 7T (registered onto 1.5T MR data).

We observed that 93.3% of our predicted results (28 out of 30, both sides of 15 PD patients) correctly hit the DBS targeting sub-regions. Figure 37 shows our robust prediction results (using the bagged PLSR with estimated error scores, 100 training

subsets, and automatically segmented RN and SN+STN) with clinically feasible measurements (ϵ_g=0.64 and 0.34mm, ϵ_l=0.25 and 0.86mm, ϵ_o=6.63 and 14°, volume=132.4 and 123.1 (V_{manual}=144.3 and 162.8), DC=76.6 and 79.1%, and error scores=0.49 and 0.66 in the left and right side, respectively), overlaid with the manual segmentation (7T) along with a post-operative electrode lead in the DBS targeting sub-region on the 1.5T T_2W MRI from a specific PD patient. This clearly illustrates that our proposed robust prediction approach provides a reliable way to guide the STN targeting for DBS surgery on the clinical 1.5T MR data.

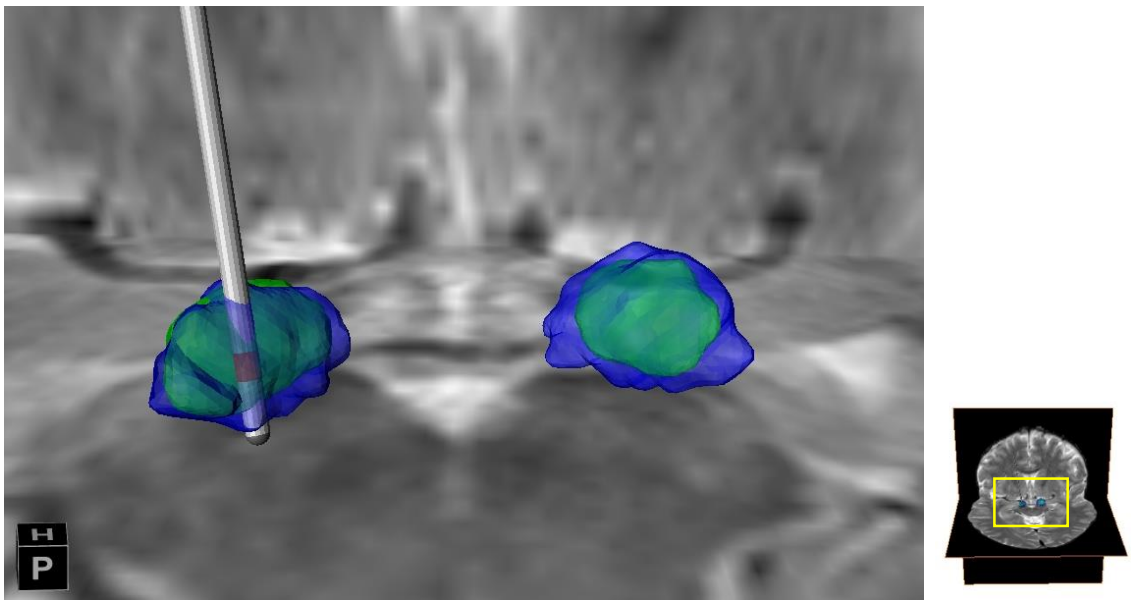

Figure 37: Visualization of a post-operative electrode image (gray; obtained from the standard post-op CT) in the DBS motor sub-region within our robust prediction result of the STN (green), overlaid with 7T ground truth manual segmentation (blue) on the axial plane of the 1.5T T_2W MRI from a specific patient.

3.4 Discussion

Overall experimental results validated that our proposed approach can automatically and accurately localize the STN on the clinical 1.5T MRI from PD patients.

We demonstrate that the quality of predictors mainly affects the prediction accuracy from prediction results using automatically and manually segmented predictors (7T), respectively. Particularly, ensemble prediction results obtained with manually segmented predictors using the bagged PLSR are slightly better than robust prediction results with estimation of influential training subsets (true error scores) and automatically segmented predictors (see ensemble results with manual SN+STN and RN using the bagged PLSR in Figure 28 and 29, and robust prediction (true error scores) with 100 subsets using the bagged PLSR in Figure 30 and 31). This finding explains that improving the segmentation of predictors might be more effective to increase the prediction accuracy when using bagged PLSR. On the other hand, when using the RF, classifying the influential training subsets was more effective to improve the prediction (see also ensemble results with manual SN+STN and RN using the RF in Figure 28 and 29 and robust prediction (true error scores) with 100 subsets using the RF in Figure 30 and 31).

Additionally, we observed that using a combined region of SN, STN and RN as predictors shows better prediction results than using each single structure. RNs are detectable on the 1.5T T_2W MRI and have been utilized as a guidance of the STN in previous studies (Dormont et al., 2010; Hamid et al., 2005; Starr et al., 2002). A combined

region of SN and STN that is highly correlated with the STN provides further useful information for the prediction.

The comparison of our prediction results with an ensemble of mean STNs from 7T MR atlases showed the predictive potential of our proposed approach. Mean STNs are calculated from subsets of similar atlases non-linearly registered onto the 1.5T MR test data of the query patient. This implies that some subsets might provide close mean STN to the real target on the patient, and others might be far from the target since non-linear registration mainly depends on the low quality appearance on the 1.5T MRIs. To handle such uncertainty issues in practice, we exploit learned shape relationships between the STN and its predictors, which are relatively more robust.

As shown in the prediction results with different number of training subsets (Figure 30 and 31), the prediction results with small number of training subsets are comparable to those with large number of subsets. An ensemble of mean STNs also shows such trend. This means that the similar atlases to the query patient and the ensemble from their subsets could already contribute to reducing the variability between random subsets (Aljabar et al., 2009), but do not further improve the results. In other words, we need to have additional information with respect to influential training subsets to the prediction in order to increase the accuracy. This motivated the development of our robust prediction framework that estimates the contribution of each training subset to the prediction.

When using the RF, the robust framework better showed its effectiveness, as presented in Figure 30 and 31. On the other hand, there was no significant improvement when using the bagged PLSR. We should note that the ensemble prediction using the bagged PLSR is much better than using the RF that often fails to capture the correct information in cases where the shapes from training subsets are highly variable (i.e., mean STN is far from true target). These facts could explain that more relevant features amongst training subsets producing good enough prediction need to be investigated to further reduce the estimation error so that it enables identification of more influential subsets, further improving the prediction. For instance, the difference between robust prediction results with estimate of error score and true ones, respectively, indicates the maximum improvement within the robust framework. Considering such estimation errors in practice, the robust prediction with large enough number of subsets could be more effective as shown in robust prediction results using the RF (Figures 30-32).

Overall predicted results produce low DC values (less than 70% of the considered acceptable value (Zou et al., 2004)), although the geometric measurements are still significantly better than in standard clinical scenarios, where it is not visible at all (e.g., $\epsilon_g \approx 1$mm, $\epsilon_l < 1$mm, and $\epsilon_o < 15^\circ$ for the best case). This might be attributed to the small volume of the STN and thresholding of an ensemble of predicted binary volumes. However, the normalization map provides a probability interpretation for confident target regions, and prediction results from large enough subsets may preserve the

geometry of the STN. Also, the manual segmentations were obtained from the 7T MRIs with clear texture or boundary information for the STN for the validation, while this is not available on the 1.5T MRI pairs of the query patient.

Recent 3T MR atlases guided direct DBS targeting approaches showed good results for visualization of the STN (Xiao et al., 2014a; Xiao et al., 2014b; D'Albis et al., 2014). However, it is still problematic to utilize such methods in standard clinical scenarios based on the 1.5T MR datasets. Manual labeling was performed, based on the intensity information of 3T MR atlases, and automatic-segmentation of the target structure on the query patient is done by the registration between 3T MR images, where they show appearance closer to 7T than 1.5T MR images. Therefore, it is hard to directly compare our approach with these methods on the 3T MR test data. However, since the quality of predictors and proper selection of similar atlases mainly affect prediction results within our approach as we aforementioned, using 3T MR test data might further improve the prediction accuracy, especially by exploiting the registration between 3T MR and 7T MR in our database.

Instead, we compared our approach with existing segmentation approaches – deformable segmentation (following our process for automatic segmentation of predictors in Section 3.2.4) and majority voting from multiple similar atlases on the 1.5T MRI. Note that manual segmentation of the STN to apply those approaches is not available on the 1.5T MR atlases, and thus we used manually segmented STN structures from 7T MRIs,

which is one of critical components of our pipeline. We demonstrated that our prediction results on the 1.5T MR patient data considerably outperform such segmentation approaches.

More importantly, for practical use, compared with the mapping of post-operative electrode trajectory, we validated that small sub-region of our robust predictions provides clinically acceptable localization of DBS leads within the motor region of ground truth STNs on standard clinical patient-specific data. We conclude that this work provides neuro-surgeons with reliable means for automatically targeting clinical target structures, where they cannot be normally seen on the clinical 1.5T MR data, reducing the need for lengthy intra-operative MER during the DBS surgery.

Our approach does not exploit intensity information within the STN for its localization. From the clinical perspectives, there still exist unclearly visible sub-parts of the STN boundary (e.g., superior-lateral part of the SN) even on the 1.5T T_2W MRI. However, it remains questionable if the information is consistent over 1.5T MR datasets from the large population of patients. If the region can be distinguished from the SN in an automatic way, the shape of the STN prediction can be further refined so that it enables more reliable targeting.

We should note that while we concentrated on STN prediction because of its relevance in Parkinson's DBS, being the most popular DBS target, the approach here presented can be exploited for predicting other structures as well.

Current processing time of our approach strongly depends on the pre-processing, including selection of similar atlases from our database, registration of the atlases onto the test data, and generation of surface points for structures in correspondence. Segmentation of multiple predictors and the prediction of the STN run in approximately 10 min. We plan to implement a fully automatic system to provide a user with a 3D model of the STN prediction within a few hours.

Finally, we are currently further validating our prediction with MER, and results on this will be reported elsewhere.

4. Conclusion

The first part of this dissertation has presented a novel active surface model for the segmentation of brain sub-cortical structures such as the basal ganglia and thalamus from ultrahigh-field MRI. Recent ultrahigh-field MR imaging facilitates direct visualization of such brain sub-cortical structures. Particularly, when multiple modalities (contrasts) are available, it allows clear delineation of adjacent structures, complementing with their visual properties. Manual segmentation is driven by operator subjectivity and inter- or intra-observer variability and also a tedious and time consuming for analysis of clinical cases in the large population of subjects. Therefore, an automatic segmentation process is required, effectively utilizing the visual benefits from multi-contrast high-field MRIs. In Chapter 2, a statistical shape model is employed to guide the evolving surface toward structures to be segmented on edge maps with limited information. A novel edge indicator function, exploiting the superior SNR and CNR of SWI at high-field MRI was introduced. This new edge indicator function generates features combining two edge maps obtained from the Laplacian of single MR modal images such as SWI, T_2W, or FA image with boundary information on the initial position of the given shape priors. Moreover, a non-overlapping repulsion force is added, iteratively delineating boundaries between neighboring objects and improving the overall quality of the segmentation. The clinical potential of the proposed approach for the segmentation of basal ganglia

components critical for DBS surgery was demonstrated with experiments on multi-modal 7T MRIs.

In the second part of this dissertation, a shape prediction framework to facilitate the STN targeting during the DBS surgery was presented. Current standard clinical MRI (1.5T or 3T) machines and protocols do not allow for direct visualization of the STN. As such, DBS surgeries today use lengthy and potentially risky the MER to verify targeting regions. With advances in ultrahigh-field (7T) MRI systems, such brain sub-cortical structures are easily visible; however, such high-fields are still limited for clinical use. In Chapter 3, a non-invasive automatic accurate localization method for the visualization of STN on standard clinical MRI is introduced. The approach exploits learned spatial relationships between the STN and its predictors based on highly detailed information from the 7T MR training data. Such predictors - RN and a combined region of SN and STN - are highly correlated with the STN and can be easily delineated on the individual patient clinical data. Given the segmentation of the predictors, the learned spatial dependency between them is used to predict the full shape of the STN. Furthermore, a robust framework is proposed to improve the prediction, estimating the prediction influence of different subsets from similar atlases. Given each training subset for the query patient, an error score as a measure for the contribution is estimated and weighted to produce the final accurate prediction. Clinical feasibility of the developed framework was validated with prediction results of the STN on clinical 1.5T MRIs from PD patients.

Finally, this dissertation provides clinicians with new automatic tools for direct patient-specific targeting of brain sub-cortical structures which cannot be normally identifiable on standard clinical data, by extracting and learning high quality information from ultrahigh-field MR atlases, ultimately, to reduce the need for intra-operative electro-physiological procedures during the DBS surgery.

Appendix A

The carefully designed acquisition protocols for each modality from 7T and 1.5T MRIs used in this study were described as below (Duchin et al., 2012; Lenglet et al., 2012). The 7T MRIs were acquired with the following acquisition protocols:

• T_1W image was acquired with the Siemens 3D MPRAGE sequence using the following parameters: field of view (FOV): 256×256×176 mm^3 with 1×1×1 mm resolution, repetition time/echo time (TR/TE) = 3000/4.03ms, nominal flip angle = 5°, bandwidth=10Hz/pixel, with an acceleration factor 2 (generalized auto-calibrating partially parallel acquisition (GRAPPA)) along the phase-encoding direction. The total acquisition time was 3.5min.

• T_2W image was acquired with a 2D turbo spin echo sequence using the following parameters: FOV = 205×205×36 mm^3 with 0.4×0.4×2.0 mm^3 resolution, TR/TE = 5000/57ms, flip angle = 120°, bandwidth = 220 Hz/pixel, with an acceleration factor of 2 (GRAPPA) along the phase-encoding direction. The total acquisition time was approximately 7 min for one average. This protocol was repeated twice, to obtain both axial and coronal images of the midbrain.

• SWI was acquired with a 3D flow-compensated gradient echo sequence using the following parameters: FOV= 180×180×60 mm^3 with 0.4×0.4×1.0 mm^3 resolution, TR/TE = 28/20msec, flip angle = 15°, bandwidth = 120 Hz/pixel, with an acceleration factor of 2 (GRAPPA) along the phase-encoding direction. One average was used, for a total

acquisition time of approximately 7 min. This protocol was also repeated twice, to obtain both axial and coronal images of the midbrain.

The 1.5T MRIs were acquired with the following standard clinical protocols:

• T_1W image was acquired using commercial Siemens T_1W AX T_1 MPR clinical protocol with the following image parameters: FOV=192×256×176 mm^3 with 0.98×0.98×1 mm^3 resolution, TR = 1650 ms; TE = 3.02 ms, nominal flip angle of 15°, bandwidth of 179 Hz/pixel.

• T_2W image was acquired using a commercial Siemens T_2W AX T_2 3D SPC (Spin Echo) clinical protocol with the following image parameters: FOV: 172×230×192 mm^3 with 0.72×0.72×2.0 mm^3 resolution, TR/TE 2500/249 msec, Flip Angle 120deg, bandwidth of 539 Hz/pixel and 2 averages.

Bibliography

Abdi, H., 2010. Partial least squares regression and projection on latent structure regression (PLS Regression). Wiley Interdiscip. Rev. Comput. Stat. 2 (1), 97-106 Jan.

Abosch, A., Yacoub, E., Ugurbil, K., Harel, N., 2010. An assessment of current brain targets for deep brain stimulation surgery with susceptibility weighted imaging at 7 tesla. Neurosurgery 67 (6), 1745-1756 Dec.

Aljabar, P., Heckemann, R., Hammers, A., Hajnal, J., Rueckert, D., 2009. Multi-atlas based segmentation of brain images: Atlas selection and its effect on accuracy. Neuroimage 46 (3), 726–738.

Artan, Y., Haider, M. A., Langer, D. L., Yetik, I. S., 2010. Semi-supervised prostate cancer segmentation with multispectral MRI. IEEE Int. Symposium on Biomedical Imaging: From Nano to Macro, pp. 648-651

Avants, B. B., Gee, J. C., 2004. Geodesic estimation for large deformation anatomical shape averaging and interpolation. Neuroimage 23 (Suppl. 1), 139–150.

Avants, B. B., Tustison, N. J., Song, G., Cook, P. A., Klein, A., Gee, J. C., 2011a. A reproducible evaluation of ANTs similarity metric performance in brain image registration. NeuroImage 54 (3), 2033-2044 Feb.

Avants, B. B., Tustison, N., Song, G., 2011b. Advanced Normalization Tools (ANTS) Release 1.5. Penn Image Computing and Science Laboratory.

Baka, N., Metz, C., Schaap, M., Lelieveldt, B., Niessen, W., De Bruijne, M., 2011. Comparison of shape regression methods under landmark position uncertainty. Med. Image Comput. Comput. Assit. Interv., pp. 434-441.

Blanc, R., Syrkina, E., Székely, G., 2009. Estimating the confidence of statistical model based shape prediction. Inf. Proc. Med. Imaging, pp. 602-613.

Blanc, R., Székely, G., 2012. Confidence regions for statistical model based shape prediction from sparse observation. IEEE Trans. Med. Imaging 31 (6), 1300–1310 Jun.

Blanc, R., Seiler, C., Székely, G., Nolte, L-P., Reyes, M., 2012. Statistical model based shape prediction from a combination of direct observations and various surrogates: Application to orthopaedic research. Med. Image Anal. 16 (6), 1156-1166 Aug.

Bossa, M., Zacur, E., Olmos, S., Alzheimer's Disease Neuroimaging Initiative, 2011. Statistical analysis of relative pose information of subcortical nuclei: Application on ADNI data. NeuroImage 55 (3), 999-1008 Apr.

Breiman, L., 1996. Bagging predictors. Machine Learning 24(2), 123-140.

Breiman, L., 2001. Random forest. Machine Learning 45(1), 5-32.

Caselles, V., Kimmel, R., Sapiro, G., 1997a. Geodesic active contours, Int. J. Computer Vision 20, 61-79

Caselles, V., Kimmel, R., Sapiro, G., Sbert, C., 1997b. Minimal surfaces based object segmentation, IEEE Trans. Pattern Analysis and Machine Intelligence 19, 394 –398 Apr.

Cerrolaza, J. J., Villanueva, A., Cabeza, R., 2012. Hierarchical statistical shape models of multiobject anatomical structures: Application to brain MRI. IEEE Trans. Med. Imaging 31 (3), 713-724 Mar.

Cerrolaza, J. J., Reyes, M., Summers, R. M., Gonzalez-Ballester, M. A., Linguraru, M. G., 2015. Automatic multi-resolution shape modeling of multi-organ structures. Med. Image Anal. 25(1), 11-21 Oct.

Chan, T. F., Vese, L. A., 2001. Active contours without edges. IEEE Trans. Image Processing 10, 266-277 Feb.

Cho, Z., Min, H., Oh, S., Han, J., Park, C., Chi, J., Kim, Y., Paek, S., Lozano, A. M., Lee, K. H., 2010. Direct visualization of deep brain stimulation targets in Parkinson disease with the use of 7-Tesla magnetic resonance imaging. Neurosurgery 113 (3), 639-647 Sep.

Cootes, T. F., Taylor, C. J., Cooper, D. H., Graham, J., 1992. Training models of shape from sets of examples. British Machine Vision Conf., pp. 266–275.

Cootes, T. F., Taylor, C. J., Cooper, D. H., Graham, J., 1995. Active shape models—Their training and application. Comput. Vis. Image Understand. 61 (1), 38–59 Jan.

Criminisi, A., Robertson, D., Konukoglu, E., Shotton, J., Pathak, S., White, S., Siddiqui, K., 2013. Regression forests for efficient anatomy detection and localization in computed tomography scans. Med. Image Anal. 17(8), 1293-1303.

D'Albis T., Haegelen, C., Essert, C., Fernandez-Vidal., S., Lays, F., Jannin, P., 2014. PyDBS: An automated image-processing workflow for planning and postoperative assessment of deep brain stimulation. Int. J. Comput. Assist. Radiol. Surg. 10(2), 117-128 May.

Daniluk, S., Davies, K. G., Ellias, S. A., Novak, P., Nazzaro, J. M., 2010. Asssessment of the variability in the anatomical position and size of the subthalamic nucleus among patients with advanced Parkinson's disease using magnetic resonance imaging. Acta Neurochirurgica 152 (2), 201-210 Feb.

den Dunnen, W. F., Staal, M. J., 2005. Anatomical alteration of the subthalamic nucleus in relation to age: a postmortem study, Mov. Disord. 20 (7), 893-898.

Dormont, D., Seidenwurm, D., Galanaud, D., Cornu, P., Yelnik, J., Bardinet, E., 2010. Neuroimaging and deep brain stimulation. Am. J. Neuroradiol. 31, 15-23 Jan.

Duchin, Y., Abosch, A., Yacoub, E., Sapiro, G., Harel, N., 2012. Feasibility of using ultra-high field (7T) MRI for clinical surgical targeting. PLoS ONE 7 (5), e37328 May.

Fang, W., Chan, K. L., 2007. Incorporating shape prior into geodesic active contours for detecting partially occluded object, Pattern Recognition 40, 2163-2172.

Fischl, B., Salat, D. H., Busa, E., Albert, M., Dieterich, M., Haselgrove, C., van der Kouwe, A. J., Killiany, R., Kennedy, D., Klaveness, S., Montillo, A., Makris, N., Rosen, B., Dale, A. M., 2002. Whole brain segmentation: Automated labeling of neuroanatomical structures in the human brain, Neuron 33, 341-355 Jan.

Fischl, B., Salat, D. H., van der Kouwe, A. J., Makris, N., Segonne, F., Quinn, B. T., Dale, A. M., 2004. Sequence-independent segmentation of magnetic resonance images, NeuroImage Math. Brain Imag., 23 (1), S69-S84.

Frangi, A. F., Rueckert, D., Schnabel, J. A., Niessen, W. J., 2002. Automatic construction of multiple-object three-dimensional statistical shape models: Application to cardiac modeling. IEEE Trans. Med. Imaging 21 (9), 1151–1166 Sep.

Gower, J.C., 1975. Generalized procrustes analysis. Psychometrika 40(1), 33-51 Mar.

Greve, D. N., Fischl, B., 2009. Accurate and robust brain image alignment using boundary-based registration. NeuroImage 48 (1), 63-72 Oct.

Guo, Y., 2010. A weighted cluster kernel PCA prediction model for multi-subject brain image data. Statistics and Its Interface 3 (1), 103-112 Jan.

Hamid, N. A., Mitchell, R. D., Mocroft, P., Westby, G. W. M., Milner, J., Pall, J. H., 2005. Targeting the subthalamic nucleus for deep brain stimulation: technical approach and fusion of pre- and postoperative MR images to define accuracy of lead placement. J. Neurol. Neurosurg. Psychiatry 76 (3), 409-414

Heimann, T., Wolf, I., Williams, T., Meinzer, H-P., 2005. 3d active shape models using gradient descent optimization of description length. Inf. Proc. Med. Imaging, pp. 566-577.

Heimann, T., Oguz, I., Wolf, I., Styner, M., Meinzer, H-P., 2006. Implementing the automatic generation of 3D statistical shape models with ITK Release 1.5. Insight J.

Heimann, T., Meinzer, H. P., 2009. Statistical shape models for 3D medical image segmentation: A reiview. Med. Image Anal. 13 (4), 543-563 Aug.

Insight Segmentation and Registration Toolkit Kitware, [Online]. Available: http://www.itk.org/

Jakab, A., Blanc, R., Berényi, E. L., Székely, G., 2012. Generation of individualized thalamus target maps by using statistical shape models and thalamocortical tractography. Am. J. Neuroradiol. 33 (11), 2110-2116 Dec.

Jenkinson, M., Smith, S. M., 2001. A global optimisation method for robust affine registration of brain images. Med. Image Anal. 5(2), 143-156 Jun.

Jenkinson, M., Bannister, P. R., Brady, J. M., Smith, S. M., 2002. Improved optimization for the robust and accurate linear registration and motion correction of brain images. NeuroImage 17 (2), 825-841 Oct.

Kacem, L. M., Poupon, C., Mangin, J. F., Poupon, F., 2010. Multi-contrast deep nuclei segmentation using a probabilistic atlas. IEEE Int. Symp. on Biomedical Imaging: From Nano to Macro, pp. 61-64.

Kerl, H. U., Gerigk, L., Pechlivanis, I., Al-Zghloul, M., Groden, C., Nölte, I. S., 2012. The subthalamic nucleus at 7.0 Tesla: evaluation of sequence and orientation for deep-brain stimulation. Acta Neurochirurgica 154 (11), 2051-2062 Nov.

Kim, H. J., Jeon, B. S., Paek, S. H., Lee, J. Y., Kim, C. K., Kim, D. G., 2010. Bilateral subthalamic deep brain stimulation in Parkinson disease patients with severe tremor. Neurosurgery 67 (3), 626-632 Sep.

Kim, J., Lenglet, C., Duchin, Y., Sapiro, G., Harel, N., 2014. Semiautomatic segmentation of brain subcortical structures from high-field MRI. IEEE J. Biomed. Health Inform. 18 (5), 1678-1695 Sep.

Kim, J., Duchin, Y., Sapiro, G., Vitek, J., Harel, N., 2015a. Clinical subthalamic nucleus prediction from high-field brain MRI. IEEE Int. Symp. on Biomedical Imaging: From Nano to Macro, pp. 1264-1267.

Kim, J., Duchin, Y., Sapiro, G., Vitek, J., Harel, N., 2015b. Clinical deep brain stimulation region prediction using regression forest from high-field MRI. IEEE Conf. Image Processing.

Kim, J., Duchin, Y., Kim, H., Vitek, J., Harel, N., Sapiro, G., 2015c. Robust prediction of clinical deep brain stimulation target structures via the estimation of influential high-field MR atlases. Med. Image Comput. Comput. Assit. Interv., pp. 587-594.

Kim, J., Duchin, Y., Shamir, R. R., Vitek, J., Harel, N., Sapiro, G., 2015d. Direct patient-specific deep brain stimulation is here: Automatic localization of surgical target structures via robust shape relationship learning from ultrahigh-field MRI. NeuroImage (Preparing for submission).

Krack, P., Hariz, M. I., Baunez, C., Guridi, J., Obeso, J. A., 2010. Deep brain stimulation: from neurology to psychiatry? Trends in Neuroscience 33 (10), 474-484 Oct.

Krishnan, A., Williams, L. J., McIntosh, A. R., Abdi, H., 2011. Partial least squares (PLS) methods for neuroimaging: A tutorial and review. NeuroImage 56 (2), 455-475 May.

Kwok, J. T-Y., Tsang, I. W-H., 2004. The pre-image problem in kernel methods. IEEE Trans. Neural Networks 15 (6), 1517-1525 Nov.

Lenglet, C., Abosch, A., Yacoub, E., De Martino, F., Sapiro, G., Harel, N., 2012. Comprehensive in vivo mapping of the human basal ganglia and thalamic connectome in individuals using 7T MRI. PLoS ONE 7 (1), 1-14 Jan.

Leventon, M., Grimson, E., Faugeras, O., 2000. Statistical shape influence in geodesic active contours. IEEE Conf. CVPR 1, 316–323.

Limousin, P., Krack, P., Pollack, P., Benazzouz, A., Ardouin, C., Hoffmann, D., Benabid, A. L., 1998. Electrical stimulation of the subthalamic nucleus in advanced Parkinson's disease. N. Engl. J. Med. 339 (16), 1105-1111 Oct.

Lorigo, L. M., Faugeras, O., Grimson, W. E. L., Keriven, R., Kikinis, R., Nabavi, A., Westin, C.-F., 2000. Codimension-two geodesic active contours for the segmentation of tubular structures. IEEE Conf. CVPR 1, 444–451.

Lucas, B. C., Kazhdan, M., Taylor, R. H., 2012. Multi-object geodesic active contours (MOGAC). Med. Image Comput. Comput. Assit. Interv., 404-412.

Ma, X., Zabaras, N., 2011. Kernel principal component analysis for stochastic input model generation. J. Comput. Phys. 230 (19), 7311-7331 Jul.

Madden, M. J., 2007. Segmentation of Images with Low-contrast Edges, M.S. thesis, Dept. Electron. Eng., West Virginia University, USA.

Mallet, L., Schüpbach, M., N'Diaye, K., Remy, P., Bardinet, E., Czernecki, V., Welter, M. L., Pelissolo, A., Ruberg, M., Agid, Y., Yelnik, J., 2007. Stimulation of subterritories of the subthalamic nucleus reveals its role in the integration of the emotional and motor aspects of behavior. Proc. of the National Academy of Sciences, pp. 10661-10666.

McKeown, M., Uthama, A., Abugharbieh, R., Palmer, S., Lewis, M., Huang, X., 2008. Shape (but not volume) changes in the thalami in Parkinson disease, BMC Neurology 8 (8).

Mika, S., Schölkopf, B., Smola, A., Müller, K-R, Scholz, M., Rätsch, G., 1999 Kernel PCA and de-noising in feature spaces. Advances in Neural Information Processing Systems 11, 536-542.

Mishina, E., 2010. Predictive properties of statistical shape models. Ph.D. thesis, Dept. Info. Tech.and Elec. Eng., ETH.

Osher, S., Sethian, J. A., 1988. Fronts propagating with curvature dependent speed: Algorithms based on Hamilton-Jacobi formulations, J. Computational Physics 79, 12-49.

Patel, N. K., Khan, S., Gill, S. S., 2008. Comparison of atlas and magnetic resonance imaging based stereotactic targeting of the subthalamic nucleus in the surgical treatment of Parkinson's disease. Stereotactic and Functional Neurosurgery 86 (3), 153-161.

Paragios, N., Deriche, R., 2000a. Coupled geodesic active regions for image segmentation: A level-set approach, European Conf. on Computer Vision, 224-240.

Paragios, N., Deriche, R., 2000b. Geodesic active contours and level-sets for the detection and tracking of moving object, IEEE Trans. Pattern Analysis and Machine Intelligence 22, 266 –280 Mar.

Patenaude, B., Smith, S. M., Kennedy, D. N., Jenkinson, M., 2011. A Bayesian model of shape and appearance for subcortical brain segmentation, NeuroImage 56 (3), 907-922.

Pieper, S., Kikinis, R., Miller, J., Halle, M., Lorensen, B., Schroeder, W. 3D Slicer [Online]. Available: http://www.slicer.org/

Rao, A., Babalola, K., Ruechert, D., 2006. Canonical correlation analysis of sub-cortical brain structures using non-rigid registration. Biomed. Image Reg., pp. 66-74.

Rao, A., Aljabar, P., Rueckert, D., 2008. Hierarchical statistical shape analysis and prediction of sub-cortical brain structures. Med. Image Anal. 12 (1), 55-68 Feb.

Rasmussen, P. M., Abrahamsen, T. J., Madsen, K. H., Hansen, L. K., 2012. Nonlinear denoising and analysis of neuroimages with kernel principal component analysis and pre-image estimation. NeuroImage 60 (3), 1807-1818 Apr.

Rathi, Y., Dambreville, S., Tannenbaum, A., 2006. Statistical shape analysis using kernel PCA. Proc. of SPIE-IS&T Electronic Imaging, pp. 60641B.

Rogers, M., Graham, J., Malik, R. A., 2000. Exploiting weak shape constraints to segment capillary images in microangiopathy. Med. Image Comput. Comput. Assit. Interv., pp. 717-726.

Sandberg, B.,Chan, T. F., 2005. A logic framework for active contours on multi-channel images, Journal of vision communication and image representation 16, 333-358.

Sapiro, G., 1996. Vector-valued active contours, IEEE Conf. CVPR, 680–685.

Schölkopf, B., Smola, A., Müller, K-R., 1998. Nonlinear component analysis as a kernel eigenvalue problem. Neural Comput. 10 (5), 1299-1319 Jul.

Schölkopf, B., Smola, A., Müller, K-R., 1999. Kernel principal component analysis. Advances in Kernel Methods – Support Vector Learning. MIT Press. pp. 327-352.

Shen, K-K., Fripp, J., Mériaudeau, F., Chételat, G., Salvado, O., Bourgeat, P., The Alzheimer's Disease Neuroimaging Initiative, 2012. Detecting global and local hippocampal shape changes in Alzheimer's disease using statistical shape models. NeuroImage 59 (3), 2155-2166 Feb.

Siverman, B. W., 1986. Density Estimation for Statistics and Data Analysis. Chapman Hall/CRC, London, U.K.

Slabaugh, G. G., 1999. Computing Euler angles from a rotation matrix. Tech. Rep.

Starr, P. A., Christine, C. W., Theodosopoulos, P. V., Lindsey, N., Byrd, D., Mosley, A., Marks, Jr., W. J., 2002. Implantation of deep brain stimulators into subthalamic nucleus: technical approach and magnetic imaging—verified electrode locations. J. Neurosurg. 97 (2), 370-387 Aug.

Sung, J. W., Kanade, T., Kim, D. J., 2007. A Unified gradient-based approach for combining ASM into AAM. Int. J. of Computer Vision. 75 (2), 297-309.

Smith, S. M., 2002. Fast robust automated brain extraction. Hum. Brain Mapp. 17, 143-155.

Styner, M. A., Rajamani, K. T., Nolte, L-P., Zsemlye, G., Székely, G., Taylor, C. J., Davies, Rhodri H., 2003. Evaluation of 3d correspondence methods for model building. Inf. Proc. Med. Imaging, pp. 63-75.

Terzopoulos, D., Witkin, A., Kass, M., 1988. Constraints on deformable models: Recovering 3D shape and nonrigid motions, Artificial Intelligence 36, 91-123.

The Deep-Brain Stimulation for Parkinson's Disease Study Group, 2001. Deep-brain stimulation of the subthalamic nucleus or the pars interna of the globus pallidus in Parkinson's disease. N. Engl. J. Med 345 (13), 956-963 Sep.

The Visualization Toolkit Kitware, [Online]. Available: http://www.vtk.org/

Uzunbas, M. G., Soldea, O., Unay, D., Cetin, M., Unal, G., Ercil, A., Ekin, A., 2010. Coupled nonparametric shape and moment-based intershape pose priors for multiple basal ganglia structure segmentation, IEEE Trans. Medical Imaging 29, 1959-1978 Dec.

Visage Imaging, Amira, [Online]. Available: http://www.amira.com/

Volkmann, J., 2007. Update on surgery for Parkinson's disease. Curr. Opin. Neurology 20 (4), 465-469 Aug.

Wold, H., 1982. Soft modeling: the basic design and some extensions. In: Wold, H., Jöreskog, K. G. (Eds.), Systems under indirect observation: Causality-Structure-Prediction. Part II. North-Holland Publishing Company, Amsterdam, pp. 1-54.

Wold, S., Sjöström, M., Eriksson, L., 2001. PLS-regression: a basic tool of chemometrics. Chemom. Intell. Lab. Syst. 58 (2), 109-130 Oct.

Woolrich, M. W., Jbabdi, S., Patenaudea, B., Chappell, M., Makni, S., Behrens, T., Beckmann, Jenkinson, C., M., Smith, S. M., 2009. Bayesian analysis of neuroimaging data in FSL, NeuroImage 45 (1), 173-186.

Xiao, Y., Jannin, P., D'Albis, T., Guizard, N., Haegelen, C., Lalys, F., Verin, M., Collins, D. L., 2014a. Investigation of Morphometric Variability of Subthalamic Nucleus, Red Nucleus, and Substantia Nigra in Advanced Parkinson's Disease Patients Using Automatic Segmentation and PCA-Based Analysis. Hum. Brain Mapp. 35 (9), 4330-4344.

Xiao, Y., Fonov, V. S., Beriault, S., Gerard, I., Sadikot, A. F., Pike, G. B., Collins, D. L., 2014b. Patch-based label fusion segmentation of brainstem structures with dual-contrast MRI for Parkinson's disease. Int. J. Comput. Assist. Radiol. Surg. 10 (7), 1029-1041 Jul.

Zimmer, C., Olivo-Marin, J.-C., 2005. Coupled parametric active contours, IEEE Trans. Pattern Analysis and Machine Intelligence 27, 1838 -1842 Nov.

Zitella, L. M., Xiao, Y., Teplitzky, B. A., Kastl, D. J., Duchin, Y., Baker, K. B., Vitek, J. L., Adriany, G., Yacoub, E., Harel, N., Johnson, M. D., 2015. In Vivo 7T MRI of the Non-Human Primate Brainstem. PLoS ONE 10 (5), e0127049 May.

Zonenshayn, M., Rezai, A. R., Mogilner, A. Y., Beric, A., Sterio, D., Kelly, P. J., 2000. Comparison of anatomic and neurophysiological methods for subthalamic nucleus targeting. Neurosurgery 47 (2), 282-292 Aug.

Zou, K. H., Warfield, S. K., Bharatha, A., Tempany, C. M. C., Kaus, M. R., Haker, S. J., Wells III, W. M., Jolesz, F. A., Kikinis, R., 2004. Statistical validation of image segmentation quality based on a spatial overlap index. Acad. Radiol. 11 (2), 178-189 Feb.

Biography

Jinyoung Kim was born in Republic of Korea in 1978. He received the B.Sc. and M.Sc. degrees in Electrical and Computer Engineering from Hanyang University, Republic of Korea, in 2004 and 2008, respectively, and the M.Sc. degree in Electrical and Computer Engineering from the University of Minnesota in 2012. From 2008 to 2010, he was with the Visual Display Division, Samsung Electronics, Republic of Korea. He is a member of Phi Kappa Phi. He expects to receive the Ph.D. in Electrical and Computer Engineering from Duke University in December 2015.